Applied Computational Electromagnetics Society

Journal

September 2012 Vol. 27 No. 9

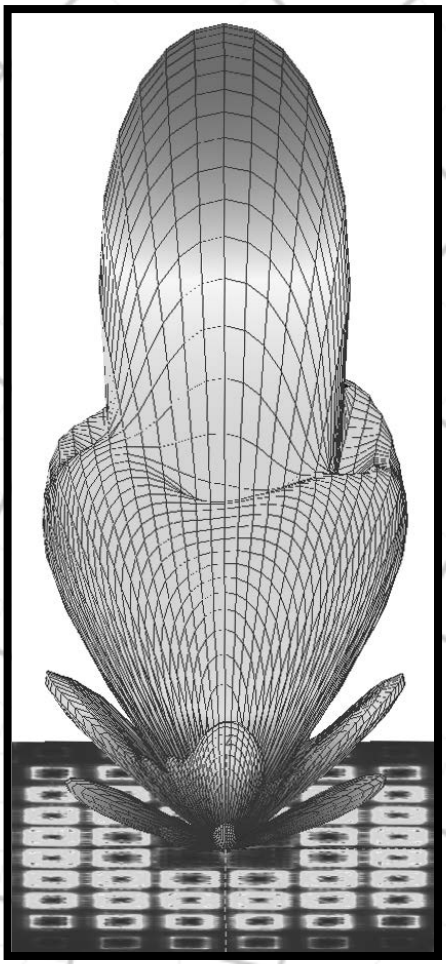

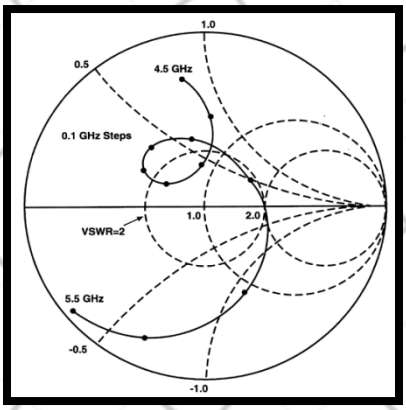

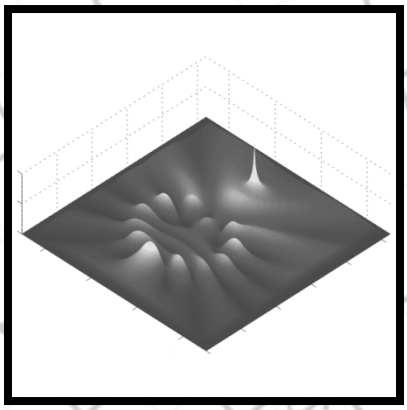

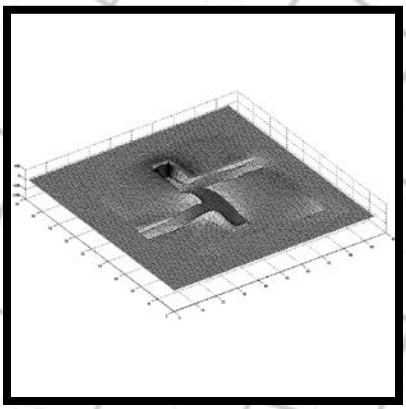

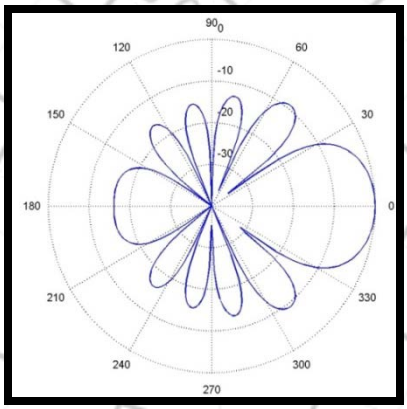

ISSN 1054-4887

GENERAL PURPOSE AND SCOPE: The Applied Computational Electromagnetics Society ***(ACES)*** Journal hereinafter known as the ***ACES Journal*** is devoted to the exchange of information in computational electromagnetics, to the advancement of the state-of-the art, and the promotion of related technical activities. The primary objective of the information exchange is to inform the scientific community on the developments of new computational electromagnetics tools and their use in electrical engineering, physics, or related areas. The technical activities promoted by this publication include code validation, performance analysis, and input/output standardization; code or technique optimization and error minimization; innovations in solution technique or in data input/output; identification of new applications for electromagnetics modeling codes and techniques; integration of computational electromagnetics techniques with new computer architectures; and correlation of computational parameters with physical mechanisms.

SUBMISSIONS: The ***ACES Journal*** welcomes original, previously unpublished papers, relating to applied computational electromagnetics. Typical papers will represent the computational electromagnetics aspects of research in electrical engineering, physics, or related disciplines. However, papers which represent research in applied computational electromagnetics itself are equally acceptable.

Manuscripts are to be submitted through the upload system of ***ACES*** web site http://aces.ee.olemiss.edu See "Information for Authors" on inside of back cover and at ***ACES*** web site. For additional information contact the Editor-in-Chief:

Dr. Atef Elsherbeni
Department of Electrical Engineering
The University of Mississippi
University, MS 386377 USA
Phone: 662-915-5382
Email: atef@olemiss.edu

SUBSCRIPTIONS: All members of the Applied Computational Electromagnetics Society are entitled to access and download the ***ACES Journal*** any published journal article available at http://aces.ee.olemiss.edu. Printed issues of the ***ACES Journal*** are delivered to institutional members. Each author of published papers receives a printed issue of the ***ACES Journal*** in which the paper is published.

Back issues, when available, are $50 each. Subscription to ***ACES*** is through the web site. Orders for back issues of the ***ACES Journal*** and change of address requests should be sent directly to ***ACES*** office at:

Department of Electrical Engineering
The University of Mississippi
University, MS 386377 USA
Phone: 662-915-7231
Email: aglisson@olemiss.edu

Allow four weeks advance notice for change of address. Claims for missing issues will not be honored because of insufficient notice, or address change, or loss in the mail unless the ***ACES*** office is notified within 60 days for USA and Canadian subscribers, or 90 days for subscribers in other countries, from the last day of the month of publication. For information regarding reprints of individual papers or other materials, see "Information for Authors".

LIABILITY. Neither ***ACES***, nor the ***ACES Journal*** editors, are responsible for any consequence of misinformation or claims, express or implied, in any published material in an ***ACES Journal*** issue. This also applies to advertising, for which only camera-ready copies are accepted. Authors are responsible for information contained in their papers. If any material submitted for publication includes material which has already been published elsewhere, it is the author's responsibility to obtain written permission to reproduce such material.

APPLIED COMPUTATIONAL ELECTROMAGNETICS SOCIETY JOURNAL

September 2012
Vol. 27 No. 9
ISSN 1054-4887

The ACES Journal is abstracted in INSPEC, in Engineering Index, DTIC, Science Citation Index Expanded, the Research Alert, and to Current Contents/Engineering, Computing & Technology.

The illustrations on the front cover have been obtained from the research groups at the Department of Electrical Engineering, The University of Mississippi.

SEPTEMBER 2012 REVIEWERS

Ahmed Abdelrahman
Robert Adams
Ayman Al-Zayed
Mohamed Bakr
M. do Rosário Calado
Dajun Cheng
Jorge Costa
Nihad Dib
Khaled ElMahgoub
Jun Hu
He Huang
Arkom Kaewrawang
Dimitra Kaklamani
Yasushi Kanai
Xiuping Li
Mehdi Salehi
Abbas Shiri
Apirat Siritaratiwat
Sanjay Velamparambil
Rui Wang
Joshua Wilson
Shaoqiu Xiao
Ozan Yurduseven

THE APPLIED COMPUTATIONAL ELECTROMAGNETICS SOCIETY

JOURNAL

Vol. 27 No. 9 September 2012

TABLE OF CONTENTS

Matlab-Based Virtual Wedge Scattering Tool for the Comparison of High Frequency Asymptotics and FDTD Method

Mehmet Alper Uslu, Levent Sevgi

Department of Electronics and Communication Engineering
Dogus University, Istanbul, Acibadem 34722, Turkey
alpuslu@gmail.com, lsevgi@dogus.edu.tr

Abstract ─ A novel Matlab-based diffraction tool for the investigation of scattered fields around a two-dimensional Perfectly Electric Conductor (PEC) wedge is introduced. Analytical (Exact by Integral, as well as some High Frequency Asymptotic (HFA) techniques) and numerical (Finite-Difference Time-Domain (FDTD)) models are included. The FDTD staircase modeling problems are removed by the application of Dey-Mittra Conformal approach.

Index Terms - conformal FDTD, Dey-Mittra, FDTD, hard boundary condition, high frequency asymptotics, scattering, soft boundary condition, staircase modeling, wedge diffraction.

I. INTRODUCTION

The two-dimensional (2D) wedge diffraction is a canonical problem and plays a fundamental role in the construction of High Frequency Asymptotic (HFA) techniques [1-8]. It has been revisited several times for the last couple of decades. One of these revisits is presented in [9] where several HFA techniques, such as Geometric Optics (GO), Physical optics (PO), Physical Theory of Diffraction (PTD), Uniform Theory of Diffraction (UTD), and Parabolic Equation (PE), are compared with each other and advantages/disadvantages are listed. A Matlab-based HFA numerical tool has also been introduced [10]. Numerical difficulties in and alternative computational approaches for complex diffraction integrals and series summation models are discussed in [11]. Finally, a novel, Finite-Difference Time-Domain (FDTD) - based multi-step numerical diffraction coefficient calculation method based on the has been introduced in [12].

A novel Matlab based WedgeFDTD package is introduced in this study. The package uses the multi-step FDTD approach presented in [12] and results are compared against available exact and HFA models. Deficiencies of staircase discretization are removed by the application of Dey-Mittra Conformal Technique [14].

The 2D wedge scattering scenario is pictured in Fig. 1. The polar coordinates r,φ,z are used throughout the paper. The z-axis is aligned along the edge of the wedge. The angle φ is measured from the top face of the wedge. The exterior angle of the wedge equals α. The wedge is illuminated by a Line Source (LS). Source and observer points are (r_0,φ_0) and (r,φ), respectively.

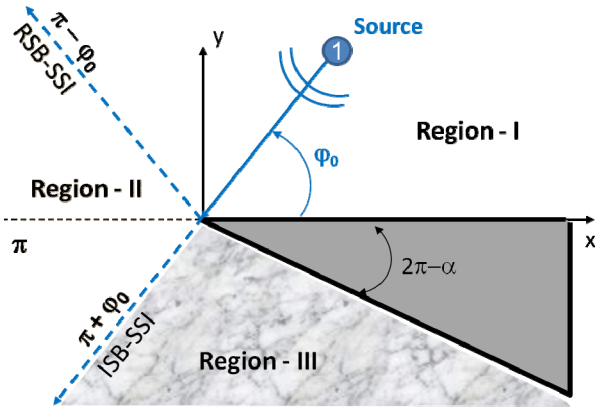

Fig. 1. The 2D PEC wedge problem, line Source (LS) illumination and three characteristic regions separated by RSB and ISB.

Submitted On: Feb. 10, 2012
Accepted On: Aug. 5, 2012

The scenario in Fig. 1 ($0<\varphi_0<\pi$) belongs to the Single Side Illumination (SSI) where *the top face is always illuminated*. The three regions are separated by two critical boundaries; *Incident Shadow Boundary* – ISB ($\varphi=\pi+\varphi_0$), *Reflection Shadow Boundary* – RSB ($\varphi=\pi-\varphi_0$). All field components – incident, reflected and diffracted fields – exist in Region–I. In Region–II, only incident and diffracted fields exist. Only diffracted fields exist in Region–III.

If the source is in ($\alpha-\pi<\varphi_0<\pi$), *both faces are always illuminated* and this is called Double Side Illumination (DSI). In this case, all three field components exist in regions $(0\le\varphi<\pi-\varphi_0)$ and $(2\alpha-\pi-\varphi_0\le\varphi<\alpha)$. There is no reflected field in $(\pi-\varphi_0\le\varphi<2\alpha-\pi-\varphi_0)$.

The field (for $\exp(-i\omega t)$) outside the wedge satisfies

$$\left(\frac{\partial^2}{\partial r^2}+\frac{1}{r}\frac{\partial}{\partial r}+\frac{1}{r^2}\frac{\partial^2}{\partial\varphi^2}+k^2\right)u = \frac{I_0}{r}\delta(r-r_0)\delta(\varphi-\varphi_0). \tag{1}$$

the Boundary Conditions (BC)

$$u_s=0 \text{ or } \partial u_k/\partial n=0 \text{ on } \varphi=0,\alpha. \tag{2-a}$$

and the Sommerfeld's Radiation Condition (SRC) at infinity:

$$\lim_{r\to\infty}\sqrt{kr}\left(\frac{du}{dr}-iku\right)=0. \tag{2-b}$$

Function u_s represents the z-component of electric field intensity E_z (TM), while function u_h is the z-component of magnetic field intensity H_z (TE), which, in acoustics, refer to acoustically soft (SBC) and hard (HBC) wedges, respectively.

II. ANALYTICAL MODELS

The problem has analytical exact as well as HFA solutions. Only analytical exact solution by integral and UTD model are given; the rest can be found in [9-12].

A. Exact solution by integral

The diffracted field solutions with SBC and HBC for both SSI and DSI are presented by Bowman and Senior in handbook [16] as:

$$u_s^{d,BS}=\{V_d(-\pi-\varphi+\varphi_0)-V_d(\pi-\varphi+\varphi_0)\}-\{V_d(-\pi-\varphi-\varphi_0)-V_d(\pi-\varphi-\varphi_0)\}, \tag{3-a}$$

$$u_s^{d,BS}=\{V_d(-\pi-\varphi+\varphi_0)-V_d(\pi-\varphi+\varphi_0)\}+\{V_d(-\pi-\varphi-\varphi_0)-V_d(\pi-\varphi-\varphi_0)\}, \tag{3-b}$$

where

$$V_d(\beta)=\frac{1}{2\pi n}\int_0^\infty H_0^{(1)}[kR(it)]\frac{\sin(\beta/n)}{\cosh(t/n)-\cos(\beta/n)}dt \tag{3-c}$$

$$n=\alpha/\pi,\ R(\eta)=\sqrt{r^2+r_0^2+2rr_0\cos(\eta)}.$$

Total fields $u_{s,h}^{t,BS}$ can be obtained by adding GO fields

$$u_{s,h}^{t,BM}/u_0=\left(u_{s,h}^{d,BM}+u_{s,h}^{GO}\right)/u_0, \tag{4}$$

where GO field that under LS excitation is given as follows:

$$u_{s,h}^{GO}=\begin{cases}H_0^{(1)}(kR_1)\pm H_0^{(1)}(kR_2), & 0\le\varphi<\pi-\varphi_0\\ H_0^{(1)}(kR_1), & \pi-\varphi_0\le\varphi<\pi+\varphi_0.\\ 0, & \pi+\varphi_0\le\varphi\le\alpha\end{cases} \tag{5-a}$$

for SSI and

$$u_{s,h}^{GO}=\begin{cases}H_0^{(1)}(kR_1)\pm H_0^{(1)}(kR_2), & 0\le\varphi<\pi-\varphi_0\\ H_0^{(1)}(kR_1), & \pi-\varphi_0\le\varphi<2\alpha-\pi-\varphi_0.\\ H_0^{(1)}(kR_1)\pm H_0^{(1)}(kR_3), & 2\alpha-\pi-\varphi_0\le\varphi\le\alpha\end{cases} \tag{5-b}$$

for DSI.

B. The UTD Model

The UTD diffracted fields are in the form of

$$u_{s,h}^{d,UTD}=u_0 d_{s,h}^{UTD}\frac{e^{-jkr}}{\sqrt{r}}. \tag{6}$$

where $u_0=H_0^{(2)}(kr_0)$ and the time dependence is $e^{j\omega t}$ [6]. According to the UTD, the diffraction coefficients for SBC and HBCs with line source as follows:

$$d_s^{UTD}(r,\varphi,\varphi_0,k)=$$

$$\frac{-e^{-j\pi/4}}{2n\sqrt{2\pi k}}\left[\begin{array}{l}\cot\left(\frac{\pi-\xi^-}{2n}\right)F\left(kLg^+(\xi^-)\right)\\+\cot\left(\frac{\pi+\xi^-}{2n}\right)F(kLg^-(\xi^-))\\-\cot\left(\frac{\pi-\xi^+}{2n}\right)F\left(kLg^+(\xi^+)\right)\\-\cot\left(\frac{\pi+\xi^+}{2n}\right)F\left(kLg^-(\xi^+)\right)\end{array}\right], \quad (7\text{-a})$$

$$d_h^{UTD}(r,\varphi,\varphi_0,k)=$$

$$\frac{-e^{-j\pi/4}}{2n\sqrt{2\pi k}}\left[\begin{array}{l}\cot\left(\frac{\pi-\xi^-}{2n}\right)F\left(kLg^+(\xi^-)\right)\\+\cot\left(\frac{\pi+\xi^-}{2n}\right)F\left(kLg^-(\xi^-)\right)\\+\cot\left(\frac{\pi-\xi^+}{2n}\right)F\left(kLg^+(\xi^+)\right)\\+c\cot\left(\frac{\pi+\xi^+}{2n}\right)F\left(kLg^-(\xi^+)\right)\end{array}\right], \quad (7\text{-b})$$

where $\xi^+=\varphi+\varphi_0$, $\xi^-=\varphi-\varphi_0$ and the Fresnel function is

$$F(X)=2j\sqrt{X}e^{jX}\int_{\sqrt{X}}^{\infty}e^{-j\tau^2}d\tau. \quad (8)$$

L, $g^{\pm}$ are determined as given in [13] by:

$$L=\frac{rr_0}{(r+r_0)}, g^{\pm}(\xi)=2\cos^2\left(\frac{2n\pi N^{\pm}-\xi}{2}\right). \quad (9)$$

Here, $N^{\pm}=\left(\pm\pi+\xi\right)/\left(2n\pi\right)$ are the integers which most nearly satisfy the last equation given in (9). Note that, the cotangent functions in (7) become singular at ISB/RSB and are replaced with [6]:

$$\cot\left(\frac{\pi\pm\beta}{2n}\right)F\left(kLg^{\pm}(\xi)\right)\simeq$$
$$n\left[\sqrt{2\pi kL}\,\mathrm{sgn}(\varepsilon)-2kL\varepsilon e^{-j\frac{\pi}{4}}\right]e^{-j\frac{\pi}{4}} \quad (10)$$

for small ε. The UTD based total fields are then obtained by adding the GO fields appropriately:

$$u_{s,h}^{t,UTD}/u_0=u_{s,h}^{d,UTD}/u_0+u_{s,h}^{GO}, \quad (11)$$

with the GO solutions given as for SSI ($0<\varphi_0<\alpha-\pi$)

$$u_{s,h}^{GO}=\begin{cases}e^{jkr\cos(\varphi-\varphi_0)}\pm e^{jkr\cos(\varphi+\varphi_0)}, & 0\le\varphi<\pi-\varphi_0\\ e^{jkr\cos(\varphi-\varphi_0)}, & \pi-\varphi_0\le\varphi<\pi+\varphi_0\\ 0, & \pi+\varphi_0\le\varphi\le\alpha\end{cases} \quad (12\text{-a})$$

and for DSI ($\alpha-\pi<\varphi_0<\pi$)

$$u_{s,h}^{GO}=\begin{cases}e^{jkr\cos(\varphi-\varphi_0)}\pm e^{jkr\cos(\varphi+\varphi_0)}, & 0\le\varphi<\pi-\varphi_0\\ e^{-jkr\cos(\varphi-\varphi_0)}, & \pi-\varphi_0\le\varphi<2\alpha-\pi-\varphi_0\\ e^{jkr\cos(\varphi-\varphi_0)}\pm e^{jkr\cos(2\alpha-\varphi-\varphi_0)}, & 2\alpha-\pi-\varphi_0\le\varphi\le\alpha\end{cases} \quad (12\text{-b})$$

Two examples are given in Figs. 2 and 3, where analytical exact solution is compared against the UTD model. Both total and diffracted field variations around the wedge are plotted. Figures 2 and 3 belong to DSI/HBC and SSI/SBC, respectively. Angles of incidences in these plots are 110º and 90º, respectively. As observed, results agree very well [10].

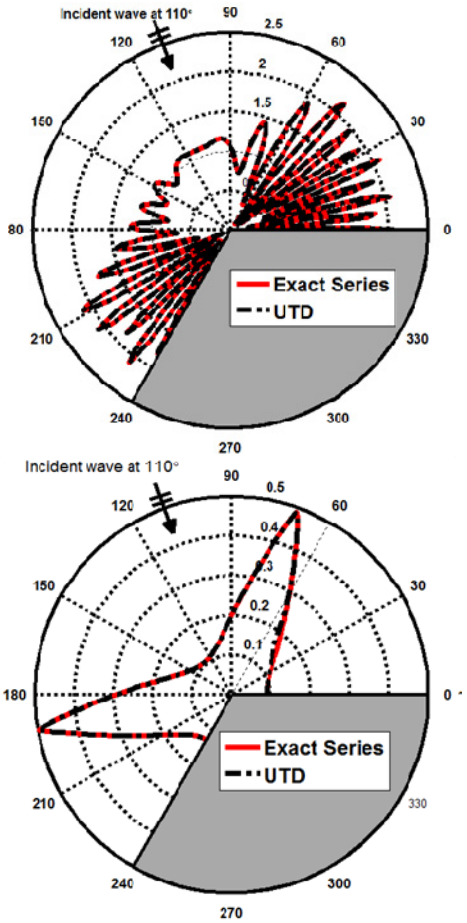

Fig. 2. (Top) Total, (Bottom) Diffracted fields around the PEC wedge; Exact by series vs. UTD

solution (HBC, $\alpha = 240^\circ$, f=30MHz, r=50m, kr=31.4).

III. FDTD MODEL

The Finite-Difference Time-Domain (FDTD) method is a pure numerical technique where Maxwell equations are directly discretized in the time-domain. Since its first introduction [13], it has been widely used in variety of EM problems. A general, multi-step FDTD-based diffraction model under the line source illumination is introduced in [12] where diffracted fields under any *source/observer locations* can be extracted. Results are calibrated via comparisons against analytical exact solutions as well as the UTD and PE models.

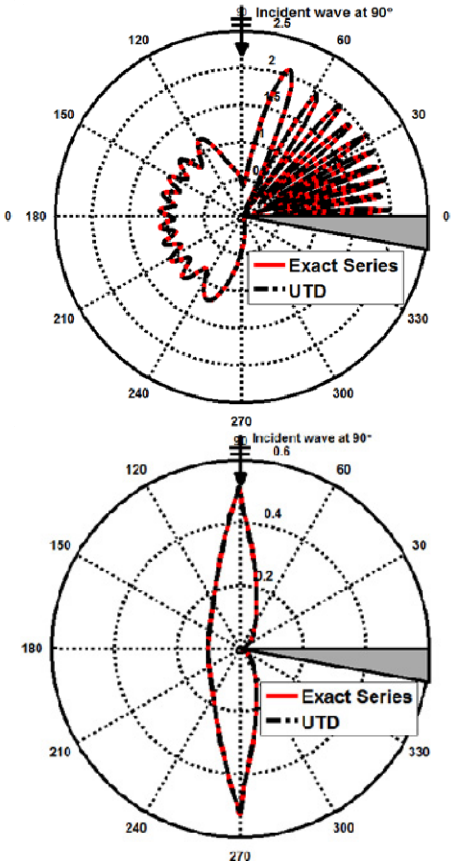

Fig. 3. (Top) Total, (Bottom) Diffracted fields around the PEC wedge; Exact by series vs. UTD solution (SBC, $\alpha = 350^\circ$, f=30MHz, r=50m, kr=31.4).

The FDTD-based wedge scattering model uses one of the two cases presented in Fig. 4. Here, a line source is injected to the E_z (H_z) component in the TM_z (TE_z) model.

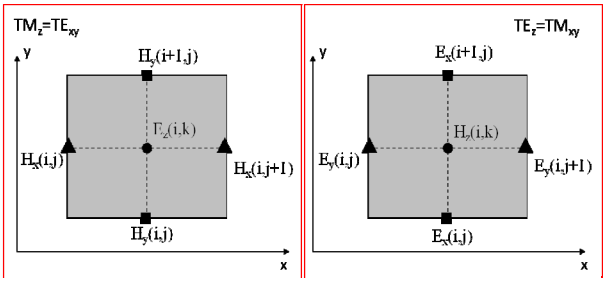

Fig. 4. The 2D FDTD cells on the xy-plane and locations of the field components.

The 2D–FDTD (TM_z type, i.e., soft BC) equations (with H_x, H_y, and E_z components) on the discrete xy–domain are:

$$H_x^{\tilde{n}}(i,j) = \frac{2\mu - \sigma_m \Delta t}{2\mu + \sigma_m \Delta t} H_x^{\tilde{n}-1}(i,j) + \frac{1}{2\mu + \sigma_m \Delta t} \frac{2\Delta t}{\Delta y} \left[E_z^n(i,j+1) - E_z^n(i,j) \right]. \quad (13)$$

$$H_y^{\tilde{n}}(i,j) = \frac{2\mu - \sigma_m \Delta t}{2\mu + \sigma_m \Delta t} H_y^{\tilde{n}-1}(i,j) + \frac{1}{2\mu + \sigma_m \Delta t} \frac{2\Delta t}{\Delta x} \left[E_z^n(i+1,j) - E_z^n(i,j) \right]. \quad (14)$$

$$E_z^n(i,j) = \frac{2\varepsilon - \sigma_e \Delta t}{2\varepsilon + \sigma_e \Delta t} E_z^{n-1}(i,j) + \frac{1}{2\varepsilon + \sigma_e \Delta t} \frac{2\Delta t}{\Delta x} \left[H_x^{\tilde{n}}(i,j) - H_x^{\tilde{n}}(i-1,j) \right] + \frac{1}{2\varepsilon + \sigma_e \Delta t} \frac{2\Delta t}{\Delta y} \left[H_y^{\tilde{n}}(i,j) - H_y^{\tilde{n}}(i,j-1) \right]. \quad (15)$$

The 2D–FDTD (TE_z type, i.e., hard BC) equations (with E_x, E_y, and H_z components) on the discrete xy–domain are

$$E_x^n(i,j) = \frac{2\varepsilon - \sigma_e \Delta t}{2\varepsilon + \sigma_e \Delta t} E_x^{n-1}(i,j) + \frac{1}{2\varepsilon + \sigma_e \Delta t} \frac{2\Delta t}{\Delta y} \left[H_z^{\tilde{n}}(i,j+1) - H_z^{\tilde{n}}(i,j) \right]. \quad (16)$$

$$E_y^n(i,j)=\frac{2\varepsilon-\sigma_e\Delta t}{2\varepsilon+\sigma_e\Delta t}E_y^{n-1}(i,j)+\frac{1}{2\varepsilon+\sigma_e\Delta t}\frac{2\Delta t}{\Delta x}\left[H_z^{\tilde{n}}(i+1,j)-H_z^{\tilde{n}}(i,j)\right]. \quad (17)$$

$$H_z^{\tilde{n}}(i,j)=\frac{2\mu-\sigma_m\Delta t}{2\mu+\sigma_m\Delta t}H_z^{\tilde{n}-1}(i,j)+\frac{1}{(2\mu+\sigma_m\Delta t)}\frac{2\Delta t}{\Delta x}\left[E_x^n(i,j)-E_x^n(i-1,j)\right]+\frac{1}{(2\mu+\sigma_m\Delta t)}\frac{2\Delta t}{\Delta y}\left[E_y^n(i,j)-E_y^n(i,j-1)\right]. \quad (18)$$

Here, i and j are labels of the discrete mesh points, Δx and Δy are the mesh sizes along x and y axes, respectively, and Δt is the time step. Medium parameters are permittivity (ε), permeability (μ), and conductivity (σ). Note, $\tilde{n}=n+1/2$ refer to $\Delta t/2$ time delay between electric and magnetic field computation time instants [13].

According to the method presented in [12] the diffracted fields are extracted for SSI as follows:

- First, FDTD is run for the PEC wedge and scattered fields are stored at n-receivers located on a circular path around the tip. This yields total fields; incident, reflected, and diffracted field components in Region II; and only the diffracted fields in Region III.
- Then, the wedge is removed, FDTD is run for free-space and scattered fields are stored with the same receivers. This yields incident fields all around.
- Finally, bottom face of the wedge is removed and top face is stretched to take up the entire transversal section of simulation space. Then, FDTD is run for the third time. The stored fields yield reflected fields on the upper half-plane.

The three pulses - the incident $u_h^{inc,FDTD}$, reflected $u_h^{\mathrm{Re}fl,FDTD}$, and diffracted $u_h^{d,FDTD}$ - are obtained using the three-step stored data. The related diffracted fields in the frequency domain are then extracted by the application of Fast Fourier Transform (FFT) as $u^d(f)=FFT\{u^{d,FDTD}(t)\}$. For DSI, a replica of third step is requires for the bottom face of the wedge. The numerical diffraction coefficient is then obtained via

$$d_h^{FDTD}=\frac{FFT\left\{u_h^{d,FDTD}\right\}}{FFT\left\{u_h^{inc,FDTD}\right\}}\frac{\sqrt{r}}{e^{ikr}} \quad (19)$$

IV. DISCRETIZATION AND DEY-MITTRA APPROCH

The FDTD procedure summarized above is calibrated against analytical exact as well as HFA models. It is shown that the method works very well under arbitrary source/ observer locations with the standard Yee model using the staircase discretization, except for angles near the bottom face of the wedge. In staircase approximation, when the center of cubic cell is embedded inside the PEC object, all surrounding electric fields of this cell are set to zero. The TM mode fits perfectly with the staircase approximation because tangential electric fields coincide with the third dimension. On the other hand, the TE mode is problematic as illustrated in Fig. 5. As observed, the staircase approximation leads to spurious diffracted fields which can erroneously alter results significantly.

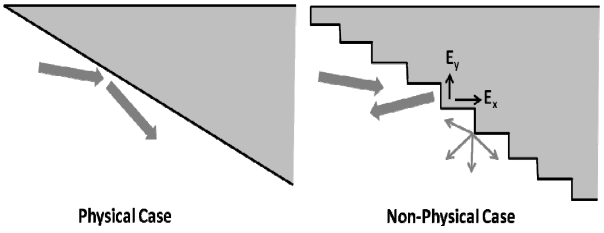

Fig. 5. Physical and non-physical case for the TE_z problem (thick arrows show incident and reflected waves, thin arrows show tip-diffracted waves).

In general, one can neglect staircase approximation error by selecting sampling resolution greater than $\lambda/60$. However, this increases computational burden proportionally and it is not suitable method for dealing with large problems and problems where phase information is crucial (as many as $\lambda/100$ may not be adequate).

Several methods are proposed to overcome staircase problems. Non-uniform gridding based on using smaller cells around the object is one approach, but the pay-off is the increase in total

number of FDTD cells and memory. Another approach is to use conformal FDTD models based on integration contour deformation around curved object being modeled and applying Faraday's law. Then, cell shape is changed to fit boundaries of modeled object. Among existing conformal models, Dey-Mittra technique described in [14] is found to be the most effective one here for the wedge problem. Fundamental steps of the Dey-Mittra technique are summarized below through cases shown in Fig. 6.

In Fig. 6a, slanted object cross slightly into top right cell. If the parameter $s/(\Delta x\Delta y)$ (s is the small area in the figure) is less than R_1 (which is the key parameter specifying numerical stability) one can neglect this penetration and set all four surrounding electric fields to zero for the top right cell. On the other hand, if Faraday's law is applied and integrated along the contour of area A_1 for top left cell one can obtain:

$$H_z^{n+1/2}(-\Delta/2,\Delta y/2)=H_z^{n-1/2}(-\Delta/2,\Delta y/2) + \frac{\Delta t}{\mu_0 A1}\begin{pmatrix} E_y^n(-\Delta x,\Delta y/2)\Delta y + \\ E_x^n(-\Delta x/2,\Delta y)f - E_x^n(-\Delta x/2,0)g \end{pmatrix} \quad (20)$$

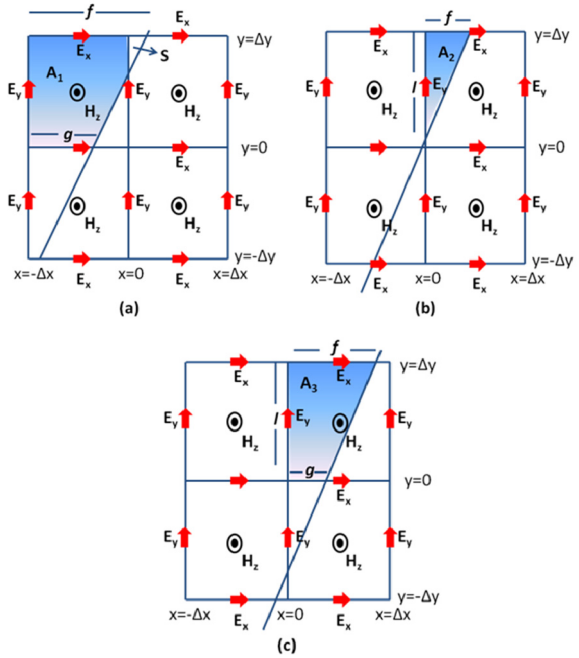

Fig. 6. Dey-Mittra conformal FDTD scenarios.

In Fig. 6b, the ratio of $A_2/(\Delta x\Delta y)$ is larger than R1. In this case, applying Faraday's Law to the top right cell and integrating over the contour of area A_2 gives the update equation for H_z on the top right cell despite the fact that it is in PEC. Noting that two electric field components reside in PEC and set to zero we have:

$$H_z^{n+1/2}(\Delta/2,\Delta y/2)=H_z^{n-1/2}(\Delta/2,\Delta y/2) + \frac{\Delta t}{\mu_0 A2}\left(E_y^n(0,\Delta y/2)l + E_x^n(\Delta x/2,\Delta y)f\right) \quad (21)$$

In Fig. 6c, applying Faraday's law and integrating along over the contour of area A_3 gives:

$$H_z^{n+1/2}(\Delta/2,\Delta y/2)=H_z^{n-1/2}(\Delta/2,\Delta y/2) + \frac{\Delta t}{\mu_0 A3}\begin{pmatrix} E_y^n(0,\Delta y/2)\Delta y \\ +E_x^n(\Delta x/2,\Delta y)f - E_x^n(\Delta x/2,0)g \end{pmatrix} \quad (22)$$

Despite its accuracy of modeling curved or slanted objects, Dey-Mittra conformal technique can cause instabilities. For this reason, time step should be reduced depending on the required accuracy. Stability analyses of several conformal methods are investigated in [15]. Here, selection of the key parameter R_1=0.0025 requires %30 reduction of time step below the normal limit of stability. Another handicap of using Dey-Mittra conformal technique is that it requires complex mesh generation for calculating intersection points of unit cells and boundaries of the object modeled.

Figure 7 compares Dey-Mittra and staircase discretization models. Here, a 60° wedge is illuminated with a line source at 160°. As observed in Fig. 6a, simulation results with Dey-Mittra conformal FDTD model agrees very well with analytical exact solution everywhere. On the other hand, staircase approximation significantly fails to yield correct behavior near the bottom face of the wedge. Things will get worse when both faces of wedge illuminated (DSI). Dey-Mittra conformal FDTD method fits exact results well.

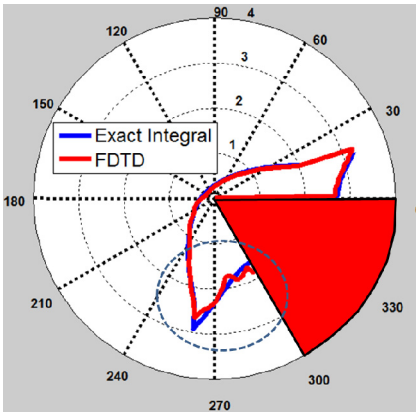

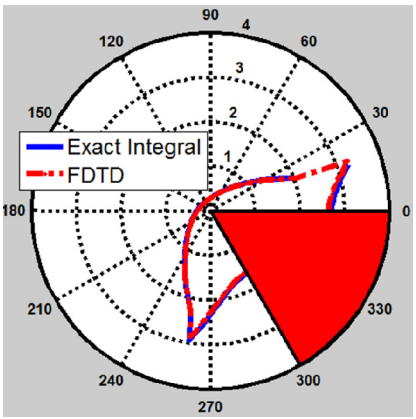

Fig. 7. Exact Solution vs. FDTD for (Top) Staircase approximation (Bottom) Dey-Mittra model.

V. THE WedgeFDTD PACKAGE AND EXAMPLES

A novel Matlab-based WedgeFDTD package with the front panel given in Fig. 8 (showing a time instant just before cylindrical waves emanating from a line source hits the top of the wedge) is developed to simulate scattered fields for a 2D PEC wedge. Results are compared against analytical exact integral method as well as the UTD model. The wedge is discretized with the Dey-Mittra approach. The program is designed with using both Matlab and Java swing library components. The interface of the program is divided into two panels as left and right. The user can enter the FDTD and simulation parameters from the left panel. At the bottom of this panel, user may select simulation results and visualization of different wave pieces. Figure 9 shows a late time instant, showing all – incident, reflected and diffracted – field components. The right panel is reserved for the FDTD visualization and simulation results. Three tabs are placed at top for this purpose.

The tabs are activated after the corresponding simulation type is clicked from the left panel. Also user can select the color map used for FDTD visualization from the popup menu which is placed at top right of this panel. Video recording property is embedded in program via external Mencoder application to reduce video size. For this purpose, one can use the record button which placed at left top of this panel. Bottom panel is dedicated for progress information of the simulation and dynamically appears while the simulation is running. The slider which separates the left and right panel enables enlarging/compressing panel sizes via horizontal scrolling. User can also export simulation results by using the standard MatLab figure toolbar.

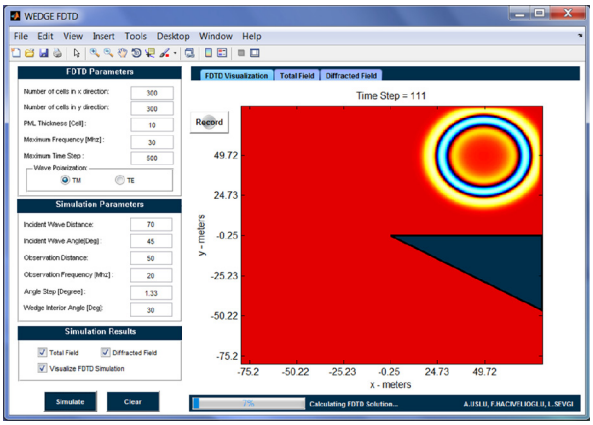

Fig. 8. The front-panel of WedgeFDTD Package.

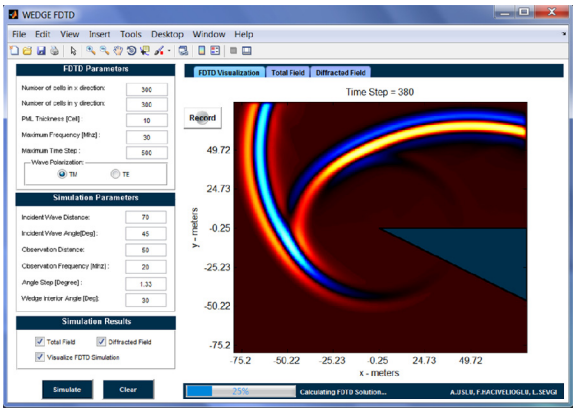

Fig. 9. The front-panel of WedgeFDTD Package showing reflected and tip-diffracted waves.

A few examples are included here. The first example is a TM_z EM or soft BC acoustic problem and belongs to a scenario with a $60°$ wedge apex angle, illuminated by a 20 MHz line source located 70 meters from the tip with the incidence angle $120°$. Total and diffracted fields are shown in Figs. 10 and 11, respectively.

The second example is a TE_z EM or Hard BC acoustic problem which belongs to a wedge with $30°$ interior angle, illuminated with a 30 MHz line source whose distance from the wedge is 80 meters and incidence angle is $45°$ W. The total and diffracted fields are observed at a distance of 50m. Results are given in Figs. 12 and 13, respectively.

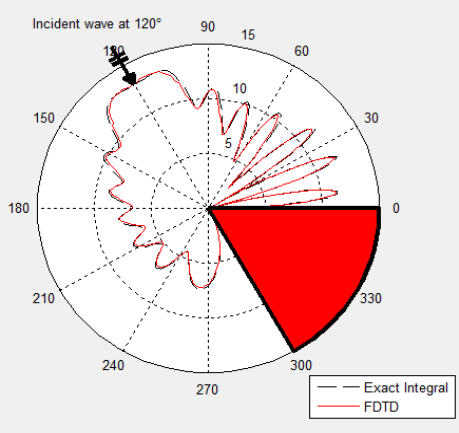

Fig. 10. Total Fields vs. angle computed with both FDTD and exact integral models ($\alpha = 300^{\circ}$, f=20MHz, r=70m, $\varphi_0 = 120^{\circ}$).

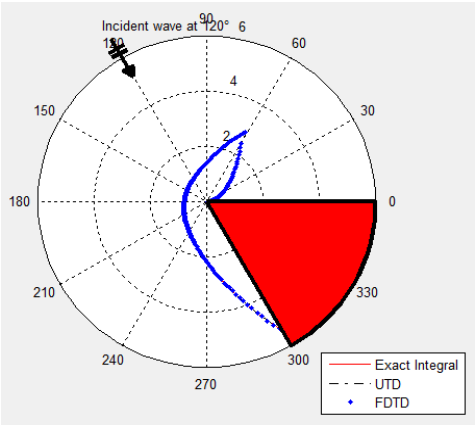

Fig. 11. Diffracted fields vs. angle solution computed with the FDTD, UTD and exact integral models ($\alpha = 300^{\circ}$, f=20MHz, r=70m, $\varphi_0 = 120^{\circ}$).

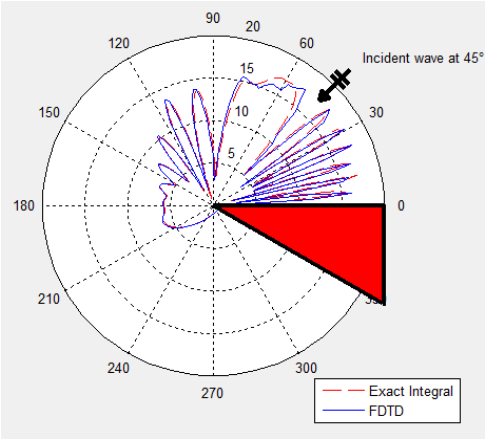

Fig. 12. Total Fields vs. angle solution computed with FDTD, UTD, and Exact integral models ($\alpha = 330^{\circ}$, f=30MHz, r=80m, $\varphi_0 = 45^{\circ}$).

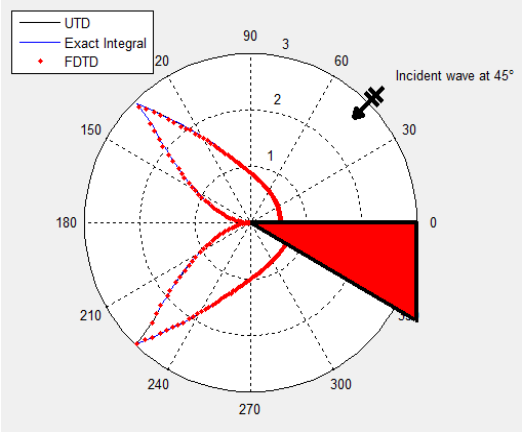

Fig. 13. Diffracted fields vs. angle solution computed with, FDTD, UTD, and Exact integral models ($\alpha = 330^{\circ}$, f=30MHz, r=80m, $\varphi_0 = 45^{\circ}$).

VI. CONCLUSION

A novel Matlab based tool is developed to investigate wedge scattering with the Finite-Difference Time-Domain (FDTD) method. Diffracted fields are extracted and are compared with the results of High Frequency Asymptotic (HFA) models. Dey-Mittra conformal FDTD method is used to eliminate staircase modeling deficiencies and results are presented. Excellent agreement among the models for both cases shows the success of the VV&C procedure [17].

REFERENCES

[1] A. Sommerfeld, "Mathematische Theorie der Diffraction," *Mathematische Annalen,* vol. 16**,** pp. 317-374, 1896.

[2] H. M. Macdonald, *Electric Waves,* The University Press, Cambridge, England, pp. 186-198, 1902

[3] G. D. Malyuzhinets, "Development of Ideas about Diffraction Phenomena," *Soviet Physics-Uspekhi*, vol. 69**,** 2, pp. 5, 1959.

[4] J. B. Keller, "The Geometric Optics Theory of Diffraction," presented at the 1953 McGill Symp. Microwave Optics, *A. F. Cambridge Res. Cen. Rep. TR-59-118* (II), pp. 207-210, 1959.

[5] V. A. Fock, *Electromagnetic Diffraction and Propagation Problems,* Pergamon Press, London, 1965.

[6] R. G. Kouyoumjian and P. H. Pathak, "A Uniform Geometrical Theory of Diffraction for an Edge in a Perfectly Conducting Surface," *Proc. IEEE*, vol. 62, pp. 1448-1461, Nov. 1974.

[7] P. Ya. Ufimtsev, *Theory of Edge Diffraction in Electromagnetics: Origination & Validation of PTD*, SciTech Publishing, Inc., 2009.

[8] P. Ya. Ufimtsev, *Fundamentals of the Physical Theory of Diffraction,* Wiley & Sons, Inc., Hoboken, New Jersey, 2007.

[9] F. Hacıvelioğlu, L. Sevgi, P. Ya. Ufimtsev, "Electromagnetic Wave Scattering from a Wedge with Perfectly Reflecting Boundaries: Analysis of Asymptotic Techniques," *IEEE Antennas and Propagation Magazine*, vol. 53, no. 3, pp. 232-253, Jun 2011.

[10] F. Hacıvelioğlu, M. A. Uslu, L. Sevgi, "A Matlab-based Simulator for the Electromagnetic Wave Scattering from a Wedge with Perfectly Reflecting Boundaries," *IEEE Antennas and Propagation Magazine*, vol. 53, no. 4, pp. 234-243, Dec. 2011.

[11] F. Hacivelioglu, L. Sevgi, "On the Numerical Evaluations of Diffraction Formulas for the Canonical Wedge Scattering Problems," *Applied Computational Electromagnetics Society (ACES) Journal*, 2012. (submitted)

[12] G. Çakır, L. Sevgi, P. Ya. Ufimtsev, "FDTD Modeling of Electromagnetic Wave Scattering from a Wedge with Perfectly Reflecting Boundaries: Comparisons against Analytical Models and Calibration," *IEEE Trans. on Antennas and Propagat.*, 2012. (to appear)

[13] K. S. Yee, "Numerical Solution of Initial Boundary Value Problems Involving Maxwell's Equations in Isotropic Media", *IEEE Trans. Antennas and Propagat*., **14**, pp. 302-307, 1966.

[14] S. Dey, R. Mittra, "A Locally Conformal FDTD Algorithm for Modeling Three-Dimensional Perfectly Conducting Objects," *IEEE Microwave and Guided Wave Letters*, 7 (9), pp. 273-275, Sep. 1997.

[15] C. J. Railton, J. B. Scheider, "An Analytical and Numerical Analysis of Several Locally Conformal FDTD Schemes," *IEEE Trans on MTT*, 47 (1), pp. 56-66, Jan. 1999.

[16] J.J. Bowman, T.B.A. Senior, P.L.E. Uslenghi, *Eds., Electromagnetic and Acoustic Scattering by Simple Shapes*, Hemisphere Publishing Corporation, 1987.

[17] G. Apaydin, L. Sevgi, "Validation, Verification and Calibration in Applied Computational Electromagnetics," *Applied Computational Electromagnetics Society (ACES) Journal*, vol. 25, no. 12, pp. 1026-1035, December 2010.

Mehmet Alper USLU was born in Turkey, in 1986. He received B.S. and M.S. in Electronics and Communication Engineering from Dogus University, Turkey in 2010 and 2012, respectively. Currently, he is pursuing his PhD studies in Institute of Science and Technology of the same university. He is one of the two recipients of Doğuş University-Felsen Fund Excellence in Electromagnetics 2011 award His research interests are diffraction theory, computational electrodynamics, RF Microwave circuits and systems, EMC and Digital signal processing algorithms.

Levent Sevgi (M'99-SM'02-F'09) has been with Dogus University since 2002. He has involved in complex electromagnetic problems for more than two decades. His research study has focused on radar systems, surface wave HF radars, propagation in complex environments, analytical and numerical methods in electromagnetic, EMC/EMI modeling and measurement, FDTD, FEM, TLM, SSPE and MoM techniques and their applications, RCS modeling, bio-electromagnetics. He is also interested in novel approaches in engineering education, teaching electromagnetics via virtual tools, and Science, Technology and Society issues.

He is a member of Turkish Chamber of Electrical Engineers (EMO), an assoc. Editor, of the IEEE Antennas and Propagation Magazine, "Testing ourselves" Column and member of the IEEE Antennas and Propagation Society Education Committee

Numerical Solution of Electromagnetic Integral Equations by the Meshfree Collocation Method

B. Honarbakhsh[1], A. Tavakoli[1, 2]

[1]Department of Electrical Engineering
[2]Institute of Communications Technology and Applied Electromagnetics
Amirkabir University of Technology (Tehran Polytechnic), Tehran, IRAN
b_honarbakhsh@aut.ac.ir, tavakoli@aut.ac.ir

Abstract ─ This paper presents guidelines for mesh free numerical solution of electromagnetic integral equations. Both static and dynamic problems are considered, including the EFIE and the MPIE for dynamic case. Different choices of the kind of meshfree method, shape functions and their parameters are studied and proper choices are suggested by logical deduction, experience or previous reports. The final configuration is applied to classical problems in one and two dimensions such as electric charge (density) and electric current (density) distributions over a line and flat plates, respectively. The method is validated by convergence analysis and is compared with MoM. In addition, suggestions are made for bypassing numerical integrations that make the construction of the coefficient matrix integration free.

Index Terms ─ collocation, EFIE, integral equation, meshfree, MPIE.

I. INTRODUCTION

Although there exist an extensive work on numerical solution of partial differential equations (PDEs) by meshfree methods (MFMs) [1]-[19], at present, volume of studies regarding integral equations (IEs) is negligible [20]-[23].

Meshless methods have four important advantages with respect to their mesh-based counterparts. First, they remove the need to a mesh generator, which requires a considerable CPU time especially for volumetric formulations. Second, the refinement process is extremely simpler. Third, the extreme capabilities of meshless shape functions in data fitting, leads to smaller matrices. Finally, since meshless shape functions usually have high order of continuity, differentiation and post processing are not of a concern.

IE solvers are of high importance in computational electromagnetics (CEM) and possess valuable properties. By the IE-based formulation, the discretization reduces only to the body under study. In contrast, when dealing with PDE solvers, the space surrounding the object should also be discretized; leading to additional memory and computational cost. IEs, also, remove the need for absorbing boundary condition (ABC) which is a bottleneck in numerical methods. Moreover, when dealing with practical problems ABCs are never precise.

EM IE solvers shortcut the above difficulties utilizing Green's function that is known for several practical situations; e.g., free space, half space and multilayer media [24]. Many realistic problems can be formulated by the aforementioned Green's functions including electromagnetic scattering, radar cross section (RCS), ground penetrating radars (GPR), microstrip antennas, planar microwave components, and lightning. The traditional numerical method for solving EM IEs is the method of moments (MoM) [25]-[27]. This method is mesh-based and uses simple expansion functions for approximating the unknown field variable and, in contrast to PDE solvers, leads to small but dense matrices.

The primary motivation of this work was extending the application domain of MFMs to IEs appearing in electrical engineering. Furthermore, since many practical problems are well formulated by hybridizing PDEs with IEs [28], [29] and noting that MFMs are powerful tools for solving

Submitted On: March 7, 2012
Accepted On: May 22, 2012

PDEs, the need for such researches becomes more comprehensible. In fact, the core ideas of this work are previously applied to such problems [30].

As a brief review on currently published works on meshfree solution of IEs, in [20] a 1D MPIE is solved over a thin straight wire by the Galerkin method and *moving least square* (MLS) shape functions as expansion functions. The work does not offer a justification for using the Galerkin type and MLS functions. Furthermore, the numerical integration strategy is not reported. Generalization of the method to more than 1D seems to be extremely time consuming and thus impractical. The major contribution of [21] is the error analysis of meshless collocation solution of the second kind Fredholm and Volterra IEs based on MLS shape functions. The given examples are abstract and of mathematical interest. Additionally, a justification for MLS method is not provided.

In [22], the CFIE is solved by meshless collocation method for bodies with cylindrical symmetry, at normal incidence. In such cases, the differential part of the IE is omitted, which considerably simplified the numerical solution. Moreover, the improved MLS (IMLS) method is used for shape function generation which is justified only in comparison with the MLS method. Finally, Hallen's IE that corresponds to a straight linear antenna is solved in [23] by the meshless collocation method utilizing *radial bases functions* (RBFs). The use of RBFs is justified based on their powerful fitting capability. This property is also present in the MLS shape functions. Therefore, the rationalization does not exclude other shape functions.

In this paper, both static and dynamic EM IEs are considered, including the EFIE and the MPIE in the case of dynamic cases. In addition, different choices of the kind of meshfree method, shape functions and their parameters are studied and proper choices are suggested by logical deduction, experience or previous reports. Noting the intrinsic complexity of meshfree shape functions that makes their evaluation time-consuming, suggestions are made to bypass numerical integrations for a specific arrangement of equidistant node arrangement. Theoretically, the idea of bypassing numerical integrations could be extended to arbitrary node distributions and is currently under investigation. Even though, the approach is general, only regular node arrangements are considered here.

II. MATHEMATICAL STATEMENT OF THE PROBLEM

In this paper, we have restricted the formulation to classical EM problems governing PECs in one and two dimensions. The guidelines throughout the paper are general.

The IEs considered in this work are Fredholm integral/integro-differential equations of the first kind, which all could be *equivalently* expressed by the following mathematical statement:

$$\begin{cases} e = O_D(y), \text{ over } \Omega \\ y = O_I(f) \\ O_I(f) = G * f \\ O_B(f) = 0, \text{ over } \partial\Omega \end{cases} . \tag{1}$$

where:

$$\begin{cases} e: \text{ excitation} \\ f: \text{ field variable} \\ G: \text{ Green's function} \\ O_D: \text{ differential operator} \\ O_I: \text{ integral operator} \\ O_B: \text{ Dirichlet boundary condition operator} \\ \Omega: \text{ problem domian} \\ \partial\Omega: \text{ problem boundary} \\ *: \text{ linear convolution} \end{cases} . \tag{2}$$

It is worth mentioning that (1) is, in general, a set of vector valued equations. In addition, the presence of O_B is problem dependent and O_D may be simplified to a multiplicative scalar.

III. A BRIEF INTRODUCTION TO MESHLESS SHAPE FUNCTIONS

In meshfree community, the expansion functions are called *shape functions*, and fall into two main categories; *approximants* and *interpolants*. We briefly introduce these types and some of their important advantages and disadvantages. Suppose the problem domain, Ω is described by M nodes. Our purpose is to fit a function u by a linear combination of M shape functions γ_i, $i = 1, \ldots, M$, at any point of Ω such that:

$$u^h(\mathbf{r}) = \overset{=T}{\Gamma}(\mathbf{r})\bar{c} = \sum_{i=1}^{M} \gamma_i(\mathbf{r}) c_i, \mathbf{r} \in \Omega. \tag{3}$$

where u^h, $\overline{\overline{\Gamma}}$ and $\bar{c}$ are fitted value of u, shape function matrix and coefficient vector, respectively [31].

A. Approximants

When shape functions are approximants, $c_i \neq u^h(\mathbf{r}_i) \equiv u_i$. There are a number of methods for generating them, e.g., *Smoothed Particle Hydrodynamics* (SPH), *Reproducing Kernel Particle Method* (RKPM), and *Moving Least Square Methods* [31]. The most powerful and known method is MLS. There are two kinds of MLS methods; *conventional* and *matrix-free* [32]. While the generated shape functions from the conventional type are very accurate, the evaluation process involves numerous small size matrix computations. Moreover, vector implementation is not possible. Thus, for evaluating each shape function at n points, the routine should be executed n times, that makes it computationally inefficient. Furthermore, the computational complexity grows dramatically by increasing the order of partial derivatives. These complexities have motivated researchers to design matrix-free MLS methods. The simplest and historically the first of this kind is the *Shepard function* [33] which is fast and vectorizable. MLS shape functions have a valuable property that make them superior to interpolants in some applications; they are *localized* and nonzero only in a small portion of the problem domain.

B. Interpolants

For interpolants, $c_i = u^h(\mathbf{r}_i) \equiv u_i$. The methods for generating such functions are called *point interpolation methods* and have two main kinds; the older employs polynomials as bases functions and the newer one uses RBFs. The RBF based methods are superior because their moment matrix is guaranteed to be non-singular [31]. While, in general, approximants are more accurate, interpolants have three valuable features that make them preferable to approximants in some cases. First, they and their partial derivatives are easy to generate. Second, imposition of Dirichlet boundary condition is extremely simple, and third, vector implementation is possible. On the other hand, they suffer from a disadvantage; their evaluation involves working with large size matrices. In other words, they work well when they are *spread* over the entire problem domain [34].

IV. SELECTION OF MESHLESS SHAPE FUNCTIONS

This section is the most important part of the present paper. Improper selection of shape functions, especially in the case of IEs, can severely degrade the quality and efficiency of the numerical solution. Consider the first equation of (1) which we call the *differential part* with y as unknown. Based on the previous section, we expanded y over RBFs to expedite the analysis. Next, consider the second equation of (1), which we name the *integral part* with f as unknown. In this case, expanding over RBFs is not reasonable. Although this selection leads to a fast computation of shape functions, their distribution over the entire domain of the problem requires either a huge number of quadrature points or a background mesh for numerical integration. Another choice is the conventional MLS shape functions. This choice is also improper. While such functions are localized over a small portion of the problem domain, for numerical integration, many evaluations are needed and this considerably slows down the numerical solution. The best option seems to be the matrix-free MLS shape functions since they are localized and fast.

V. MESHLESS DISCRETIZATION

From a theoretical point of view, meshfree solution of (1) can be based on any of the Galerkin, Petrov-Galerkin and collocation methods. However, due to the complex nature of meshless shape functions, their evaluation is considerably time consuming. Consequently, Implementation of the first two choices may not be straightforward, since numerical integration involves numerous evaluations. Thus, only the collocation method is applied in this study. Here, discretization of (1) is performed by assuming scalar functions and operators. Generalization to vector case is straightforward.

Numerical solution of (1) by meshfree collocation method can be carried out by the following three steps. First, scatter M nodes over the problem domain and on its boundary. Second, expand the unknown functions over the proper meshfree shape functions, and third, equate both sides of the equation at the nodes and solve the corresponding linear system of equations after imposition of boundary conditions.

Following the aforementioned steps, let the problem domain Ω and the boundary $\partial\Omega$ be described by M nodes. Assume $\{\varphi_i\}_{i=1}^{M}$ and $\{\psi_i\}_{i=1}^{M}$ be sets of shape functions for the nodes, where φ_i and ψ_i represents the interpolant and approximant corresponding to the ith node, respectively. Following the previous section by expanding y over interpolants and f over approximants, i.e.:

$$\begin{cases} y^h(\mathbf{r}) = \boldsymbol{\Phi}^T(\mathbf{r})\cdot\hat{\mathbf{y}} = \sum_{i=1}^{M}\varphi_i(\mathbf{r})\widehat{y_i} \\ f^h(\mathbf{r}) = \boldsymbol{\Psi}^T(\mathbf{r})\cdot\hat{\mathbf{f}} = \sum_{i=1}^{M}\psi_i(\mathbf{r})\widehat{f_i} \end{cases}. \tag{4}$$

where y^h and f^h are interpolated and approximated value of y and f, respectively. Replacing the first Eq. of (4) into the first Eq. of (1) and collocating at the nodes leads to

$$\hat{\mathbf{e}} = \mathbf{K}_D\cdot\hat{\mathbf{y}}. \tag{5}$$

with

$$\begin{cases} \left[\hat{\mathbf{e}}\right]_p = e(\mathbf{r}_p) \\ \left[\mathbf{K}_D\right]_{pq} = O_D\left[\varphi_q(\mathbf{r}_p)\right] \end{cases}. \tag{6}$$

Similarly, by replacing the second Eq. of (4) into the second Eq. of (1),

$$\boldsymbol{\Phi}^T\cdot\hat{\mathbf{y}} = \mathbf{K}_I\cdot\hat{\mathbf{f}}. \tag{7}$$

where

$$\left[\mathbf{K}_I\right]_{pq} = O_I\left[\psi_q(\mathbf{r}_p)\right]. \tag{8}$$

What remains is imposition of the Dirichlet boundary condition that is the last equation of (1). Because this equation acts on f, we should first eliminate $\hat{\mathbf{y}}$ and relate the excitation vector $\hat{\mathbf{e}}$ to $\hat{\mathbf{f}}$, directly. Consequently:

$$\begin{cases} \hat{\mathbf{e}} = \mathbf{K}\cdot\hat{\mathbf{f}} \\ \mathbf{K} = \mathbf{K}_D\cdot\boldsymbol{\Phi}^{-T}\cdot\mathbf{K}_I \end{cases}. \tag{9}$$

The unknown coefficient vector $\hat{\mathbf{f}}$ can now be found by solving (9) after imposition of the boundary condition, which is now straightforward.

VI. GENERAL GUIDELINES FOR COMPUTING THE ENTRIES OF $\mathbf{K}_I$

The calculation of $\mathbf{K}_I$ is the most critical and time-consuming part of the final coefficient matrix, $\mathbf{K}$. This section provides guidelines for its accurate and efficient computation.

Numerical integration is a vital step in weighted residual methods. It can severely affect the accuracy and speed of the solution. In IE based methods, presence of the Green's function increases the complexity of this step, particularly for high order of singularities. Additionally, meshless shape functions are more complicated and their evaluation is considerably slower than elementary mathematical functions such as polynomials and complex exponentials. This becomes extremely visible, when numerical integration is involved in the analysis.

The key point of this section is noting that approximant shape functions are *bell-shaped* and consequently, can be well approximated by a single bell-shaped function such as Gaussian and Butterworth. As a 1D example:

$$\psi(x) \cong \begin{cases} a_G\exp\left(-\xi_G x^2\right), & \text{Gaussian} \\ a_B\left[1+\left(x/x_B\right)^{2n_B}\right]^{-1}, & \text{Butterworth} \end{cases}. \tag{10}$$

where the parameters a_G, ξ_G, a_B, x_B, and n_B can be easily estimated by curve fitting methods. A sample approximation of a 1D Shepard approximant is represented in Fig. 1.

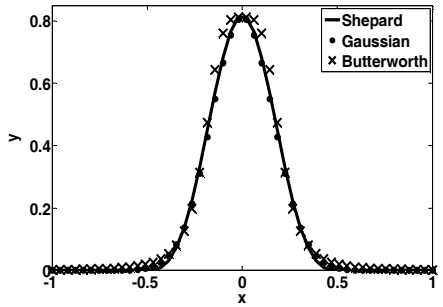

Fig. 1. Approximating a sample 1D Shepard approximant by Gaussian and Butterworth functions.

This simplifies handling of the problem and increases the computational efficiency. Moreover, since the Fourier transform of both Gaussian and Butterworth functions are available in all dimensions, such a substitution makes the understanding of the spectral behavior of the approximants possible. The importance of this point is made more comprehensible in the next section. The aforementioned matrix can be computed in both the space and the spectral domains. Thus, we split this section into two parts and discuss each case separately.

A. Space domain

In the space domain, some possible choices are *approximate Green's function*, *the Duffy transform* [35], *advanced quadratures* [36], *and fast convolution methods* [37]. Except for the last choice, all aforementioned methods are time consuming, but simple to implement. Although the method introduced in [37] is considerably more efficient than others, its implementation is not simple.

B. Spectral domain

Exploiting the spectral domain for computation of $\mathbf{K}_I$ is rooted in the convolutional nature of the EM IEs and can be performed in different ways. Considering (1) and (4), the mathematical form required for computing $\mathbf{K}_I$ is:

$$\begin{aligned} s &= \psi_i * G \\ &= \mathscr{F}^{-1}\left\{\mathscr{F}\left\{\psi_i\right\}\cdot\mathscr{F}\left\{G\right\}\right\}. \end{aligned} \tag{11}$$

where ψ_i is the approximant corresponding to the ith node and $\mathscr{F}$ stands for *continuous Fourier transform* (CFT). For this purpose, the most obvious choice is using the (inverse) fast Fourier transform, which can be efficiently computed by available FFT/IFFT algorithms. However, existence of singularity in the Green's function can potentially deteriorate the accuracy.

Here, we introduce our proposed method which is based on two assumptions. First, the problem domain and the boundary should be described by regular node arrangements. Under this assumption, all ψ_i approximants become shifted version of each other. The method can be potentially generalized to handle arbitrary configurations, which is currently under investigation. Second, it is necessary to approximate the approximants by a function having analytical Fourier transform. Under these assumptions, it is possible to compute (11) by a closed form expression. It is worth mentioning that this procedure is severely problem-dependent.

VII. NUMERICAL RESULTS

In this section, the guidelines are followed to solve five classic EM problems by the meshfree collocation method. Problem domains and boundaries are described by regular node arrangement for fast computation of the coefficient matrix. In all cases, d is the radial nodal distance. The approximant used is the Shepard function as defined by [33]:

$$\psi_i(\mathbf{r}) = w_i(\mathbf{r})\left(\sum_{j=1}^{M} w_j(\mathbf{r})\right)^{-1}. \tag{12}$$

with *quadric spline function* as its weighting defined by [38]:

$$w_i(\mathbf{r}) = w(d_i) = \begin{cases} 1-6d_i^2+8d_i^3-3d_i^4, & d_i \le r_0 \\ 0, & d_i > r_0 \end{cases}. \tag{13}$$

where M is the number of nodes, $d_i = |\mathbf{r}-\mathbf{r}_i|$ and r_0 is the *support size* of the Shepard function. For all 2D examples $r_0 = d/2^{1/2}$ is chosen. Approximants are approximated by a single Gaussian function for all cases. In addition, interpolants are constructed from *thin plate spline* (TPS) RBFs. Results are validated by convergence analysis [39]. Furthermore, convergence of the 1D dynamic case is compared with a pulse/rooftop MoM code and 2D dynamic cases are compared with RWG MoM codes developed by Makarov [40]. It should be pointed out that the number of nodes and unknowns are always denoted by M and N, respectively. Thus, for 1D and static examples N = M, whereas for 2D dynamic examples N = 2M. The error estimate is based on

$$r_e(u_m, u_{m+1}) = |u_{m+1}-u_m|/|u_m|. \tag{14}$$

with u_m being a functional of the field variable computed at the mth pass. Finally, the simulations are executed on a Intel(R) Core(TM)2 6700 CPU with 4 GB RAM.

A. Static charge over infinite PEC strip

As a 1D scalar static IE, consider the equation governing the static charge distribution over a 2 m width PEC infinite strip [27]:

$$\begin{cases} \int_{-1}^{1} G(x-x')\,q_s(x')\,dx' = 1, & |x| \le 1 \\ G(x) = -(2\pi\varepsilon_0)^{-1}\ln|x| \end{cases}. \tag{15}$$

It is assumed that the strip has the potential of 1 V and is placed on the x-y plane, along the y-axis and is centered at the origin. By comparing (15) with (1) one can recognize that:

$$\begin{cases} e = 1 \\ f = q_s(x) \\ O_D(u) = u \\ \Omega : -1 \le x \le 1 \end{cases}. \tag{16}$$

Thus, the problem has neither the differential part nor the boundary condition. For this problem $r_0 = 1.5d$ and adaptive Gauss-Kronrod quadrature is used for numerical integrations. The convergence curve in the sense of total charge and the normalized charge distribution across the strip are depicted in Fig. 2.

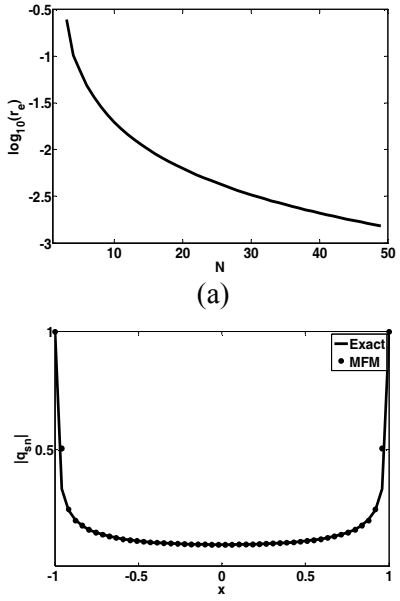

Fig. 2. Static charge per unit length on an infinite PEC strip: (a) convergence curve, (b) spatial distribution of normalized charge.

B. Static charge density over square PEC plate

As a 2D scalar static IE, consider the equation governing the static charge density distribution over a unit length square PEC plate [25]:

$$\begin{cases} \int_{Plate} G(\mathbf{r}-\mathbf{r}')\rho_s(\mathbf{r}')d\mathbf{r}' = 1, |x| \wedge |y| \le 1 \\ G(\mathbf{r}) = (4\pi\varepsilon_0 r)^{-1} \end{cases} . \quad (17)$$

It is assumed that the plate has the potential of 1 V and is placed on the *x*-*y* plane, centered at the origin. By comparing (17) with (1), a similar expressions to (16) can be written. Thus, problem has neither the differential part nor boundary condition. Following the proposed method, the computation of the $\mathbf{K}_1$ matrix can be carried out without numerical integration by noting that

$$\begin{cases} \mathcal{F}\{\exp(-\xi r^2)\} = (\pi/\xi)\exp(-k_r^2/4\xi) \\ \mathcal{F}\{G\} = k_r^{-1} \end{cases} . \quad (18)$$

where $r = (x^2 + y^2)^{1/2}$. Therefore [41]:

$$\begin{aligned} s(r) &= (\pi/\xi)\int_0^\infty \exp(-k_r^2/4\xi)k_r^{-1}J_0(k_r r)k_r dk_r \\ &= (\pi/4\xi)^{1/2}\exp(-\xi r^2/2)I_0(\xi r^2/2). \end{aligned} \quad (19)$$

The convergence curve in the sense of capacity per unit length and the normalized charge density distribution over the plate are depicted in Figs. 3(a) and 3(b), respectively. In addition, Fig. 3(c) compares the computational cost of $\mathbf{K}_1$ by direct numerical integration in the space domain and the proposed spectral domain method based on (19).

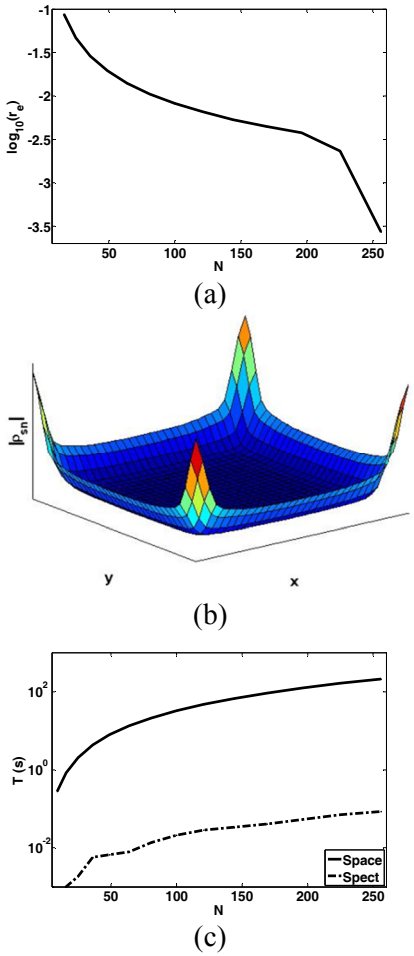

Fig. 3. Static charge density over square PEC plate: (a) convergence curve, (b) spatial distribution of normalized charge density, (c) computation cost of $\mathbf{K}_1$.

C. Scattering by a thin PEC wire

As a 1D scalar dynamic IE, consider the equation governing the current distribution over a 6λ thin PEC wire. The problem can be formulated by two mathematically equivalent IEs, i.e., EFIE and MPIE [25], [42]:

$$\begin{cases} EFIE: j\omega\left(1+k_0^{-2}\,\partial^2/\partial z^2\right)A=1 \\ MPIE: j\omega A+\nabla V=1 \end{cases}, |z|<3\lambda. \tag{20}$$

subject to:

$$I=0, |z|=3\lambda. \tag{21}$$

where

$$\begin{cases} A(z)=\mu_0\int\limits_{Wire} G(z-z')I(z')dz' \\ V(z)=-(j\omega\varepsilon_0)^{-1}\int\limits_{Wire} G(z-z')\dfrac{dI(z')}{dz'}dz' \end{cases}. \tag{22}$$

and

$$G(z)=\left(4\pi\sqrt{z^2+a^2}\right)^{-1}\exp\left(-jk\sqrt{z^2+a^2}\right). \tag{23}$$

The wire is placed on the z-axis, centered at the origin, with radius $a = 0.00628\lambda$. It is assumed that the wire is normally illuminated by an incident plane wave of unit amplitude and angular frequency of ω. By comparing (20)-(23) with (1),

$$\begin{cases} e=1 \\ f=I(z) \\ O_D(u)=j\omega\left(1+k_0^{-2}\,\partial^2/\partial z^2\right)u. \\ \Omega: -3\lambda<z<3\lambda \\ \partial\Omega: z=\pm 3\lambda \end{cases} \tag{24}$$

Thus, both formulations have differential part and boundary condition. In this case, $r_0 = 2.5d$ and adaptive Gauss-Kronrod quadrature is used for numerical integrations. The convergence curves in the sense of normalized monostatic RCS and the normalized current distribution for 35 nodes and reconstructed at 200 nodes are depicted in Figs. 4(a) and 4(b), respectively. Additionally, Fig. 4(c) compares the computational cost of $\mathbf{K}_I$ by direct numerical integration in the space with the proposed method exploiting FFT.

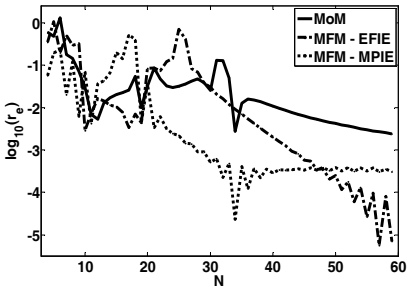

(a)

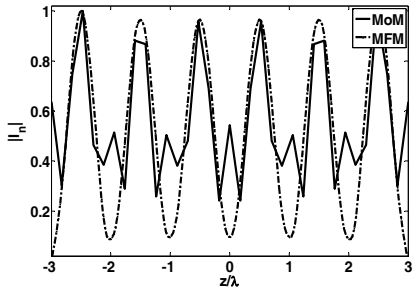

(b)

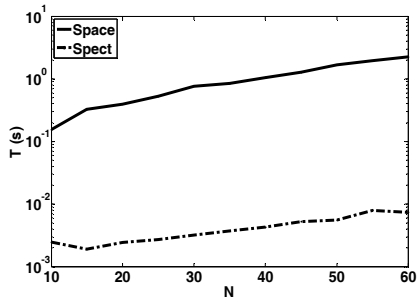

(c)

Fig. 4. Scattering by a 6λ thin PEC wire: (a) convergence curves, (b) spatial distribution of normalized current for 35 nodes and reconstructed at 200 nodes, (c) computation cost of $\mathbf{K}_I$.

D. Scattering by a PEC square plate

As a 2D vector dynamic IE, consider the equation governing the current density distribution over a 3λ PEC square plate. Similar to the previous case, the problem can be formulated by EFIE and MPIE:

$$\begin{cases} EFIE: j\omega\left(1+k_0^{-2}\nabla\nabla\cdot\right)\mathbf{A}=\hat{\mathbf{x}} \\ MPIE: j\omega\mathbf{A}+\nabla V=\hat{\mathbf{x}} \end{cases}, |x|\wedge|y|<3\lambda/2. \tag{25}$$

subject to:

$$\begin{cases} J_x=0, |x|=3\lambda/2 \\ J_y=0, |y|=3\lambda/2 \end{cases}. \tag{26}$$

where:

$$\begin{cases} \mathbf{A}(\mathbf{r})=\mu_0\int\limits_{Plate} G(\mathbf{r}-\mathbf{r}')\mathbf{J}(\mathbf{r}')d\mathbf{r}' \\ V(\mathbf{r})=-(j\omega\varepsilon_0)^{-1}\int\limits_{Plate} G(\mathbf{r}-\mathbf{r}')\nabla'\cdot\mathbf{J}(\mathbf{r}')d\mathbf{r}' \end{cases}. \tag{27}$$

and:

$$G(\mathbf{r})=(4\pi r)^{-1}\exp(-jkr). \tag{28}$$

The plate is placed on the x-y plane, centered at the origin and illuminated by an incident wave with an x-directed electric field of unit amplitude

and angular frequency of ω. Comparing (25)-(28) with (1) leads to

$$\begin{cases} e = \mathbf{x} \\ f = \mathbf{J}(\mathbf{r}) \\ O_D(u) = j\omega\left(1 + k_0^{-2}\nabla\nabla\cdot\right)u \\ \Omega : -3\lambda/2 < x,\, y < 3\lambda/2 \\ \partial\Omega : (x,\, y) = (\pm 3\lambda/2,\, \pm 3\lambda/2) \end{cases} . \tag{29}$$

As in the previous case, both formulations have differential part and boundary condition. By applying the proposed spectral method, it is straightforward to show that the mathematical forms of the integrals for computing $\mathbf{K}_I$ are

$$\begin{cases} g_1(r) = \int_0^\infty (jk_z)^{-1}\, \widetilde{\psi}(r) J_0(k_r r) k_r dk_r \\ g_2(r) = \cos\theta \int_0^\infty (jk_z)^{-1}\, \widetilde{\psi}(r) J_1(k_r r) k_r^2 dk_r \\ g_3(r) = \sin\theta \int_0^\infty (jk_z)^{-1}\, \widetilde{\psi}(r) J_1(k_r r) k_r^2 dk_r \end{cases} . \tag{30}$$

where $\tan(\theta) = y/x$, and:

$$\begin{cases} \widetilde{\psi}(r) = \mathcal{F}\{\psi(r)\} = e^{-\frac{k_r^2}{4\xi}} \\ \widetilde{G}(r) = \mathcal{F}\{G(r)\} = (jk_z)^{-1} = \left(k_r^2 - k_0^2\right)^{-1/2} \end{cases} . \tag{31}$$

For fast evaluation of (31), we follow the idea behind the *discrete complex image method* (DCIM) [43]. Suppose:

$$\widetilde{\psi}(r) = \sum_{m=1}^{M} a_m e^{-b_m k_z} . \tag{32}$$

which can be efficiently calculated by the *matrix-pencil-method* (MPM) [44]. Now, a closed-form of the aforementioned integrals can be readily obtained by making use of the *Sommerfeld identity* and its first derivative [45]. The convergence curves in the sense of normalized monostatic RCS and the normalized current density distribution for N = 2×19×19 and reconstructed at 22500 nodes are depicted in Figs. 5(a) and 5(b), respectively. Additionally, the computational cost of $\mathbf{K}_I$ is reported in Fig. 5(c).

E. Scattering by a PEC circular plate

As 2D vector dynamic IE over a non-rectangular domain, consider the equation governing the current density distribution over a PEC circular plate with $\lambda/4$ radius. Similar to the previous case, the problem can be formulated by EFIE and MPIE, subject to

$$J_x \cos\theta + J_y \sin\theta = 0,\; x^2 + y^2 = (\lambda/4)^2 . \tag{33}$$

The plate is placed on the *x*-*y* plane, centered at the origin. The excitation, discretization parameters and numerical integration strategy are the same as the previous problem. The convergence curves in the sense of normalized monostatic RCS, a nodal arrangement based on 98 nodes and the corresponding normalized current density distribution reconstructed at 17500 nodes, are depicted in Fig. 6.

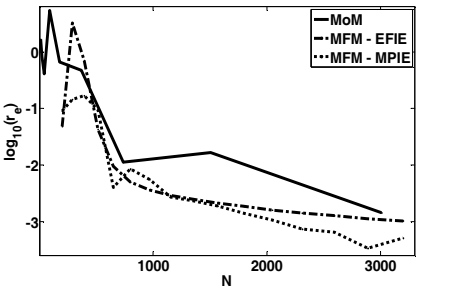

(a)

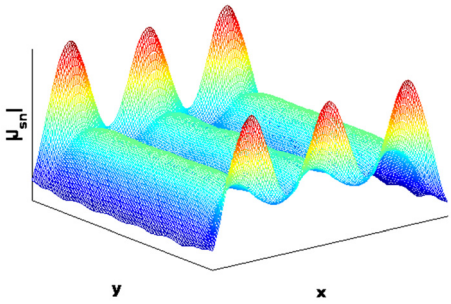

(b)

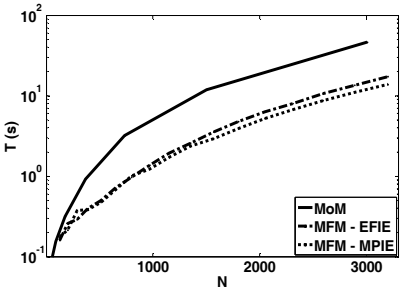

(c)

Fig. 5. Scattering by a 3λ PEC square plate: (a) convergence curves, (b) spatial distribution of normalized current density for N = 2×19×19, (c) computation cost of $\mathbf{K}_I$.

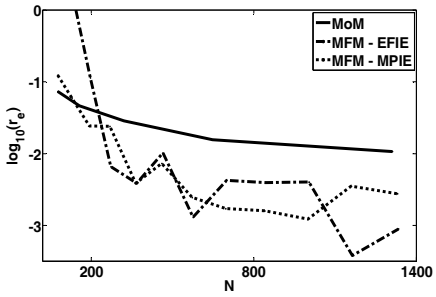

(a)

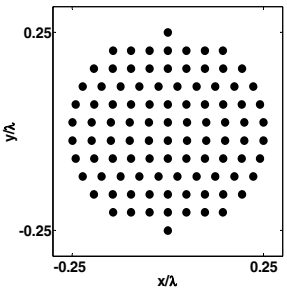

(b)

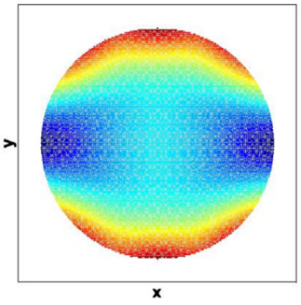

(c)

Fig. 6. Scattering by a PEC circular plate with $\lambda/4$ radius: (a) convergence curves, (b) nodal arrangement based on 98 nodes, (c) reconstructed solution at 17500 nodes.

VIII. CONCLUSION

The meshfree collocation method is formulated for numerical solution of electromagnetic integral equations including EFIE and MPIE. Both RBF interpolants and Shepard approximants are utilized for efficient analysis. Suggestions are also made for bypassing numerical integration.

ACKNOWLEDGMENT

The authors acknowledge Prof. M. Dehghan for inputs in meshfree methods, and Prof. R. F. Dana, for inputs in validation techniques.

REFERENCES

[1] Y. Marechal, "Some Meshless Methods for Electromagnetic Field Computations," *IEEE Trans. Magn*., vol. 34, no. 5, pp. 3351-3354, 1998.

[2] C. Herault and Y. Marechal, "Boundary and Interface Conditions in Meshless Methods," *IEEE Trans. Magn.*, vol. 35, no. 3, pp. 1450-1453, 1999.

[3] S. L. Ho, S. Yang, J. M. Machado, and H. C. Wong, "Application of a Meshless Method in Electromagnetics," *IEEE Trans. Magn.*, vol. 37, no. 5, pp. 3198-3201, 2001.

[4] L. Xuan, Z. Zeng, B. Shanker, and L. Udpa, "Meshless Method for Numerical Modeling of Pulsed Eddy Currents," *IEEE Trans. Magn*., vol. 40, no. 6, pp. 3457-3462, 2004.

[5] S. L. Ho, S. S. Yang, H. C. Wong, and G. Ni, "Meshless Collocation Method based on Radial Basis Functions and Wavelets," *IEEE Trans. Magn.*, vol. 40, no. 2, pp. 1021-1024, 2004.

[6] S. L. Ho, S. S. Yang, G. Ni , H. C. Wong, and Y. Wang, "Numerical Analysis of Thin Skin Depths of 3-D Eddy-Current Problems using a Combination of Finite Element and Meshless Methods," *IEEE Trans. Magn*., vol. 40, no. 2, pp. 1354-1357, 2004.

[7] S. L. Ho, S. S. Yang, H. C. Wong, E. W. C. Lo and G. Ni, "Refinement Computations of Electromagnetic Fields using FE and Meshless Methods," *IEEE Trans. Magn*., vol. 41, no. 5, pp. 1456-1459, 2005.

[8] Y. Zhang, K. R. Shao, D. X. Xie and J. D. Lavers, "Meshless Method based on Orthogonal Basis for Electromagnetics," *IEEE Trans. Magn*., vol. 41, no. 5, pp. 1432-1435, 2005.

[9] Q. Li and K. Lee, "Adaptive Meshless Method for Magnetic Field Computation," *IEEE Trans. Magn*., vol. 42, no. 8, pp. 1996-2003, 2006.

[10] R. K. Gordon, W. E. Hutchcraft, "The Use of Multiquadric Radial Basis Functions in Open Region Problems," *Applied Computational Electromagnetics Society (ACES) Journal*, vol. 21, no. 2, pp. 127-134, July 2006.

[11] Y. Zhang, K. R. Shao, J. Zhu, D. X. Xie and J. D. Lavers, "A Comparison of Point Interpolative Boundary Meshless Method based on PBF and RBF for Transient Eddy-Current Analysis," *IEEE Trans. Magn*., vol. 43, no. 4, pp. 1497-1500, 2007.

[12] F. G. Guimaraes, R. R. Saldanha, R. C. Mesquita, D. A. Lowther, and J. A. Ramirez, "A Meshless Method for Electromagnetic Field Computation based on the Multiquadratic Technique," *IEEE Trans. Magn.*, vol. 43, no. 4, pp. 1281-1284, 2007.

[13] S. Ikuno, K. Takakura, and A. Kamitani, "Influence of Method for Imposing Essential Boundary Condition on Meshless Galerkin/Petrov-Galerkin Approaches," *IEEE Trans. Magn*., vol. 43, no. 4, pp. 1501-1504, 2007.

[14] S. McFee, D. Ma, and M. Golshayan, "A Parallel Meshless Formulation for h-p Adaptive Finite

Element Analysis," *IEEE Trans. Magn*., vol. 44, no. 6, pp. 786-789, 2008.

[15] T. Kaufmann, C. Fumeaux, R. Vahldieck, "The Meshless Radial Point Interpolation Method for Time-Domain Electromagnetics", *IEEE MTT-S Int. Microwave Symp. Dig.*, Atlanta, pp. 61 - 64, 2008.

[16] Y. Yu and Z. Chen, "A 3-D Radial Point Interpolation Method for Meshless Time-Domain Modeling," *IEEE Trans. Microwave Theory Tech.*, vol. 57, no. 8, pp. 2015-202, 2009.

[17] Y. Yu and Z. Chen, "Towards the Development of an Unconditionally Stable Time-Domain Meshless Method," *IEEE Trans. Microwave Theory Tech.*, vol. 58, no. 3, pp. 578- 586, 2010.

[18] T. Kaufmann, C. Engström, C. Fumeaux, R. Vahldieck, "Eigenvalue Analysis and Longtime Stability of Resonant Structures for the Meshless Radial Point Interpolation Method in Time Domain", *IEEE Trans. Microwave Theory Tech.*, vol. 58, no. 12, pp. 3399 - 3408, 2010.

[19] R. D. Soares, R. C. Mesquita, F. J. S. Moreira, "Axisymmetric Electromagnetic Resonant Cavity Solution by a Meshless Local Petrov-Galerkin Method," *Applied Computational Electromagnetics Society (ACES) Journal*, vol. 26, no. 10, pp. 792-799, October 2011.

[20] M. Zhang, L. Lingxia, P. Zhou, and X. Zhang, "A Novel Mesh-Free Method for Electromagnetic Scattering from a Wire Structure," *PIERS Online*, vol. 3, no. 6, pp. 774-776, 2007.

[21] D. Mirzaei and M. Dehghan, "A Meshless based Method for Solution of Integral Equations," *Appl. Numer. Math.*, vol. 60, no. 3, pp. 245-262, 2010.

[22] W. L. Nicomedes, R. C. Mesquita, and F. J. S. Moreira, "An Integral Meshless-based Approach in Electromagnetic Scattering," *COMPEL Int. J. Comput. Math. Elec. Elec. Eng.*, vol. 29, no. 6, pp. 1464-1473, 2010.

[23] S. J. Lai, B. Z. Wang , and Y. Duan, "Meshless Radial Basis Functions Method for Solving Hallen's Integral Equation," *Applied Computational Electromagnetic Society (ACES) Journal*, vol. 27, no. 1, pp. 9-13, 2012.

[24] W. C. Chew, *Waves and Fields in Inhomogeneous Media*. IEEE Press, 1995.

[25] R. F. Harrington, *Field Computation by Moment Methods*. New York: Macmillan, 1968.

[26] J. R. Mosig, "Arbitrary Shaped Microstrip Structures and their Analysis with a Mixed Potential Integral Equation," *IEEE Trans. Microwave Theory Tech.*, vol. 36, no. 2, pp. 314-323, 1988.

[27] R. Bancroft, *Understanding Electromagnetic Scattering Using the Moment Method*. Artech House, 1996.

[28] J. Jin and J. L. Volakis, "A Finite Element-Boundary Integral Formulation for Scattering by Three-Dimensional Cavity-Backed Apertures," *IEEE Trans. Antennas Propagat.*, vol. 39, no. 1, pp. 97-104, 1991.

[29] Z. Huang, K. R. Demarest, and R. G. Plumb, "An FDTD/MoM Hybrid Technique for Modeling Complex Antennas in the Presence of Heterogeneous Grounds," *IEEE Trans. Geosci. Remote*, vol. 37, no. 6, pp. 2692-2698, 1999.

[30] B. Honarbakhsh and A. Tavakoli, "Scattering by a 2D Crack: The Meshfree Collocation Approach," *Applied Computational Electromagnetic Society (ACES) Journal*, vol. 27, no. 3, pp. 278-284, 2012.

[31] G. R. Liu, *Mesh Free Methods*. CRC Press, 2003.

[32] G. E. Fasshauer, *Approximation Theory X: Wavelets, Splines and Applications*. Vanderbilt University Press, 2002.

[33] D. Shepard, "A Two Dimensional Interpolation Function for Irregularly Spaced Data," in *Proc. 23rd Nat. Conf. ACM*, pp. 517–523, 1968.

[34] R. Schaback, "Limit Problems for Interpolation by Analytic Radial Base Functions," *Comp. Appl. Math.*, vol. 212, no. 2, pp. 127-149, 2008.

[35] M. G. Duffy, "Quadrature over a Pyramid or Cube of Integrands with a Singularity at a Vertex," *SIAM J. Numer. Anal.*, vol. 19, pp. 1260-1262, 1982.

[36] L. F. Shampine, "Vectorized Adaptive Quadrature in MATLAB," *J. Comput. Appl. Math.*, vol. 211, pp. 131-140, 2008.

[37] G. Beylkin, C. Kurcz and L. Monzon, "Fast Convolution with the Free Space Helmholtz Green's Function," *J. Comput. Phys.*, vol. 228, pp. 2770-2791, 2009.

[38] G. R. Liu and Y. T. Gu, *An Introduction to MeshFree Methods and Their Programming*. Springer, 2005.

[39] J. C. Rautio, "The Microwava Point of View on Software Validation," *IEEE Antennas Propagat. Mag*., vol. 38, no. 2, pp. 68-71, 1996.

[40] S. N. Makarov, *Antenna and EM Modeling with MATLAB*, Wiley-InterScience, 2002.

[41] I. S. Gradshteyn, I. M. Ryzhik, A. Jeffrey, and D. Zwillinger, *Table of Integrals, Series, and Products*, 6th Edition, Academic Press, 2000.

[42] W. C. Gibson, *The Method of Moments in Electromagnetics*. Chapman & Hall/CRC, Taylor & Francis Group, 2008.

[43] Y. L. Chow, J. J. Yang, D.G. Fang, G. E. Howard, "A Closed-Form Green's Function for the Thick Microstrip Substrate," *IEEE Trans. Microwave Theory Tech.*, vol. 39, no. 3, pp. 588-592, 1991.

[44] T. K. Sarkar, O. Pereira, "Using the Matrix Pencil Method to Estimate the Parameters of a Sum of Complex Exponentials," *IEEE Antennas Propagat. Mag*., vol. 37, no. 3, pp. 48-55, 1995.

[45] M. Yuan, T. K. Sarkar, M. Salazar-Palma, "A Direct Discrete Complex Image Method from the Closed-Form Green's Functions in Multilayered Media" *IEEE Trans. Microwave Theory Tech*., vol. 54, no. 3, pp. 1025-32, 2006.

Babak Honarbakhsh was born in Tehran, Iran. He received his B.S. and M.S. degrees in electrical engineering from Amirkabir University of Technology where he is currently working toward his Ph.D. degree. His current research interest is numerical solution of electromagnetic problems by meshfree methods.

Ahad Tavakoli was born in Tehran, Iran, on March 8, 1959. He received B.S. and M.S. degrees from the University of Kansas, Lawrence, and the Ph.D. degree from the University of Michigan, Ann Arbor, all in electrical engineering, in 1982, 1984, and 1991, respectively.

He is currently a Professor in the Department of Electrical Engineering at Amirkabir University of Technology. His research interests include EMC, scattering of electromagnetic waves and microstrip antennas.

Micromagnetic Modeling on Magnetisation Dynamics with Lossy Magnetic Material in Thin Film Heads by FDTD Calculations

Gustavo Recio and César Estébanez

Department of Computer Science
Universidad Carlos III de Madrid, Spain
grecio@inf.uc3m.es, cesteban@inf.uc3m.es

***Abstract* —** An extension to the standard FDTD formulation aimed at modelling the micromagnetics of materials together with the solution of Maxwell's equations is presented in this paper. Numerical computations using actual thin film head geometries were carried out with the purpose of validating the method. The analysis of results revealed the importance of the method for modelling electromagnetic interaction with lossy magnetic material in the presence of current and magnetic sources.

***Index Terms* —** FDTD Computations, Equation of Motion, Eddy Currents, Magnetic Losses, Micromagnetic Model, Recording Heads, Magnetic Recording, Thin Film Heads.

I. INTRODUCTION

Advances in recording speeds have reached a point where the micromagnetics of the heads have become a physical limit. Consequently, to continue with the rise in areal storage densities and to push towards higher recording speeds, research has been focused on understanding and improving flux propagation and reversal times in thin-films inductive recording heads [1], [2]. The flux reversal time is the time required in order to obtain a response from the magnetic flux (inside the head circuit) to changes in the write current waveform. Minimising this time in the head yoke reduces the rise time of the writing fields in the pole tip region and allows shorter and well defined magnetic transitions to be written onto the storage medium [3].

High-speed experimental studies using the time-resolved magneto-optical Kerr microscope on magnetic thin-films [1] and on thin-film recording heads [2] have contributed to furthering the understanding of the switching mechanisms in these magnetic structures. With the reduction of the size of the active regions in thin-film recording heads [4], the ability to observe the flux distribution during switching in the pole tip region of heads is becoming beyond the optical resolution of this technique. As a result, modelling and simulation are becoming increasingly important as alternative tools to understand the flux reversal process in these small head features and to enable the optimisation of write head designs. This motivated the study of the contribution and effect of eddy currents when working at high frequencies, e.g. developing non-destructive evaluations of conductive materials by means of eddy current imaging [5].

Static models of characterising magnetic heads include equivalent circuit models, transmission line models and finite elements models [6], [7], [8], [9], [10], [11]. These are either time independent or limited in the frequency domain to the fundamental response, and ignore the magnetic detail of the head material. Dynamic models, on the other hand, utilise full micromagnetic description of the magnetic material [12], but the absence of electromagnetic formulation in these models neglects the eddy current effect coming from time varying fields in the finite resistivity thin-film materials. Therefore the need arises for a dynamic model that combines the solution to Maxwell's equations for the electromagnetic fields with micromagnetic models of the material to accurately simulate the reversal process in magnetic heads.

Modern computational methods such as the Finite Difference Time Domain (FDTD) algorithm will play a key role in modelling magnetic heads in the future [13]. The FDTD method solves the electromagnetic phenomena for a given geometry inside a computational space and, as a result, the magnitude and direction of the electromagnetic fields are given for the whole computational space. This research extends

Submitted On: March 1, 2012
Accepted On: July 22, 2012

the standard FDTD algorithm to model the micromagnetics of materials together with the solution of Maxwell's equations having in this manner a better description of the reversal process. Studying and characterising the fast switching process (dynamics) in thin-film heads is the main aim of this work which will be achieved through FDTD computations of actual thin-film head geometries. The advantage provided by this study is that magnetisation motion can be simulated considering electromagnetic interaction in lossy magnetic material by making use of the FDTD method and the LLG equation (having a better description of the reversal process).

This paper is organised as follows, Section II formalises the general electromagnetic theory and the micromagnetic model formulation for non-linear magnetic materials which form the basis behind the numerical work in this research. Section III presents the discretisation of the equation of motion. Space and time synchronism, boundary conditions and stability of the extended method are dealt with in Sections IV, V and VI respectively. In Section VII the numerical experiments carried out are presented followed by an analysis of results. The paper concludes with a discussion of the main findings in Section VIII.

II. Non-linear Magnetic Materials

When linear magnetic materials are considered, the magnetic flux density **B** is proportional to the external magnetic field $\mathbf{H_{app}}$ by a constant called the permeability of the material μ. However, when considering non-linear magnetic materials, the following equation applies

$$\mathbf{B} = \mu_o(\mathbf{H_{app}} + \mathbf{M}) \tag{1}$$

where the magnetisation vector **M** is taken into account to calculate the magnetic flux density.

Extending the FDTD method to non-linear magnetic materials requires to start by considering Maxwell's curl equations for a general medium.

$$\frac{\partial \mathbf{B}}{\partial t} = -\nabla \times \mathbf{E} \tag{2}$$

$$\frac{\partial \mathbf{D}}{\partial t} = \nabla \times \mathbf{H_{eff}} \tag{3}$$

where **B** is as in (1) and

$$\mathbf{D} = \epsilon \mathbf{E} \tag{4}$$

substituting **B** and **D** into (2) and (3) yields

$$\frac{\partial \mathbf{H_{app}}}{\partial t} = -\frac{1}{\mu_o}\nabla \times \mathbf{E} - \frac{\partial \mathbf{M}}{\partial t} \tag{5}$$

$$\frac{\partial \mathbf{E}}{\partial t} = \frac{1}{\epsilon}\nabla \times \mathbf{H_{eff}} \tag{6}$$

where the nonlinearity introduced by the term $\partial\mathbf{M}/\partial t$ is described by Landau-Lifshitz-Gilbert's (LLG) equation [14].

$$\frac{\partial \mathbf{M}}{\partial t} = -\gamma(\mathbf{M} \times \mathbf{H_{eff}}) + \frac{\alpha}{M_s}\left(\mathbf{M} \times \frac{\partial \mathbf{M}}{\partial t}\right) \tag{7}$$

III. Discretisation of LLG Equation

To discretise all of above equations, central finite difference expressions, which provide second order accuracy, for the space and time derivatives are used. Equation (6) follows the same expression as in the normal FDTD method therefore no changes are needed for the E_z component in the 2D TM_z mode.

$$\begin{aligned} E_z|^{n+\frac{1}{2}}_{i+\frac{1}{2},j+\frac{1}{2}} &= C_a|_{i+\frac{1}{2},j+\frac{1}{2}} E_z|^{n-\frac{1}{2}}_{i+\frac{1}{2},j+\frac{1}{2}} \\ &+ C_b|_{i+\frac{1}{2},j+\frac{1}{2}} \Big(H_y|^n_{i+1,j+\frac{1}{2}} - H_y|^n_{i,j+\frac{1}{2}} \\ &+ H_x|^n_{i+\frac{1}{2},j} - H_x|^n_{i+\frac{1}{2},j+1} \Big) \end{aligned} \tag{8}$$

Equation (5) has a new term $\partial M/\partial t$, which is discretised using central differences in time, and it must be included in the final expressions for H_x and H_y.

$$\begin{aligned} H_x|^{n+1}_{i+\frac{1}{2},j+1} &= D_a|_{i+\frac{1}{2},j+1} H_x|^n_{i+\frac{1}{2},j+1} \\ &+ D_b|_{i+\frac{1}{2},j+1} \Big(E_z|^{n+\frac{1}{2}}_{i+\frac{1}{2},j+\frac{1}{2}} - E_z|^{n+\frac{1}{2}}_{i+\frac{1}{2},j+\frac{3}{2}} \Big) \\ &- M_x|^{n+1}_{i+\frac{1}{2},j+1} + M_x|^n_{i+\frac{1}{2},j+1} \end{aligned} \tag{9}$$

$$\begin{aligned} H_y|^{n+1}_{i+1,j+\frac{1}{2}} &= D_a|_{i+1,j+\frac{1}{2}} H_y|^n_{i+1,j+\frac{1}{2}} \\ &+ D_b|_{i+1,j+\frac{1}{2}} \Big(E_z|^{n+\frac{1}{2}}_{i+\frac{3}{2},j+\frac{1}{2}} - E_z|^{n+\frac{1}{2}}_{i+\frac{1}{2},j+\frac{1}{2}} \Big) \\ &- M_y|^{n+1}_{i+\frac{1}{2},j+1} + M_y|^n_{i+\frac{1}{2},j+1} \end{aligned} \tag{10}$$

where the coefficients C and D are described as

$$C_a|_{i,j} = \left(1 - \frac{\sigma_{i,j}\Delta t}{2\varepsilon_{i,j}}\right) \Big/ \left(1 + \frac{\sigma_{i,j}\Delta t}{2\varepsilon_{i,j}}\right) \tag{11}$$

$$C_b|_{i,j} = \left(\frac{\Delta t}{\varepsilon_{i,j}}\Delta\right) \Big/ \left(1 + \frac{\sigma_{i,j}\Delta t}{2\varepsilon_{i,j}}\right) \tag{12}$$

$$D_a|_{i,j} = \left(1 - \frac{\sigma^*_{i,j}\Delta t}{2\mu_{i,j}}\right) \Big/ \left(1 + \frac{\sigma^*_{i,j}\Delta t}{2\mu_{i,j}}\right) \tag{13}$$

$$D_b|_{i,j} = \left(\frac{\Delta t}{\mu_{i,j}\Delta}\right) \Big/ \left(1 + \frac{\sigma^*_{i,j}\Delta t}{2\mu_{i,j}}\right) \tag{14}$$

for which $\Delta x = \Delta y = \Delta$ is assumed.

An expression for the magnetisation vector components can be obtained by expanding the vector product in LLG equation (7) and solving for $\partial M_x/\partial t$, $\partial M_y/\partial t$ and $\partial M_z/\partial t$; this yields

$$\begin{aligned}\frac{\partial M_x}{\partial t} = {} & \frac{\gamma}{M_s(1+\alpha^2)}[M_s(H_z M_y - H_y M_z) \\ & +\alpha M_x(H_y M_y + H_z M_z) - \alpha H_x(M_s^2 - M_x^2)]\end{aligned} \tag{15}$$

$$\begin{aligned}\frac{\partial M_y}{\partial t} = {} & \frac{\gamma}{M_s(1+\alpha^2)}[M_s(H_x M_z - H_z M_x) \\ & +\alpha M_y(H_x M_x + H_z M_z) - \alpha H_y(M_s^2 - M_y^2)]\end{aligned} \tag{16}$$

$$\begin{aligned}\frac{\partial M_z}{\partial t} = {} & \frac{\gamma}{M_s(1+\alpha^2)}[M_s(H_y M_x - H_x M_y) \\ & +\alpha M_z(H_x M_x + H_y M_y) - \alpha H_z(M_s^2 - M_z^2)]\end{aligned} \tag{17}$$

Applying central time differences to (15) and evaluating M_x at time step $n + 1/2$ yields

$$\frac{M_x|^{n+1} - M_x|^n}{\Delta t} = f(H_x, H_y, H_z, M_x, M_y, M_z)|^{n+\frac{1}{2}} \tag{18}$$

rearranging terms gives the time marching scheme for M_x

$$M_x|^{n+1} = M_x|^n + f(H_x, H_y, H_z, M_x, M_y, M_z)|^{n+\frac{1}{2}}\Delta t \tag{19}$$

where $f(H_x, H_y, H_z, M_x, M_y, M_z)$ is a function of the magnetic field and the magnetisation vector components coming from (15) and has the form

$$\begin{aligned}f(H, M) = {} & \frac{\gamma}{M_s(1+\alpha^2)}\Bigg[M_s(H_z M_y - H_y M_z) \\ & +\alpha M_x(H_y M_y + H_z M_z) - \alpha H_x \frac{M_s^2 - M_x^2}{M_y^2 + M_z^2}\Bigg]\end{aligned} \tag{20}$$

The magnetisation components are evaluated at the same spatial location as the magnetic field components in the Yee's cell. Time marching expressions for M_y and M_z are derived in the same manner. From equation (19) it is noticed that M_y, M_z, H_y and H_z are used to compute the new value of M_x, however, these are placed at different locations than M_x within the Yee's cell, therefore spacial interpolation is needed. It is also noticed that equation (19) uses M_x, M_y, M_z, H_x, H_y and H_z evaluated at time step $n + 1/2$ while their values are only known at time step n, with n being an integer, thus time extrapolation is required. The proper space and time discretisation of LLG equation to maintain second order accuracy are addressed in detail next.

IV. Space and Time Synchronism

Here two different problems are addressed to maintain second order accuracy of the central difference scheme. First, H_x, H_y, H_z, M_x, M_y and M_z are not known at time step $n+1/2$ in (19) or any other M (the same applies for the time marching expressions for M_y and M_z). A simple approach to solve this problem is to use an extrapolation scheme [15] in which the current value of a variable depends on the previous values using the backward differencing approximation

$$u|^{n+\frac{1}{2}} \simeq u|^{n-\frac{1}{2}} + \left.\frac{\partial u}{\partial t}\right|^{n-\frac{1}{2}} \Delta t \tag{21}$$

The unknown value of $u|^{n-\frac{1}{2}}$ on the right side of the equation can be expressed as the average of $u|^{n-1}$ and $u|^n$ and the derivative can be estimated using standard central differences. These operations lead to the second order accurate time marching formalism for correct integration into the FDTD scheme.

$$\begin{aligned}u|^{n+\frac{1}{2}} & \simeq \tfrac{u|^{n-1}+u|^n}{2} + u|^n - u|^{n-1} \\ & = \tfrac{1}{2}(3u|^n - u|^{n-1})\end{aligned} \tag{22}$$

To illustrate the time synchronism, M_x will be computed for time step $n + 1$. From (19), H_x, H_y, H_z, M_x, M_y and M_z must be known at time step $n + 1/2$ in order to evaluate $M_x|^{n+1}$. This is done by applying the time synchronism equation (22) to all vector components of $\mathbf{H}$ and $\mathbf{M}$ using previous values at time steps n and $n - 1$.

$$H_{x,y,z}|^{n+\frac{1}{2}} = \frac{1}{2}(3H_{x,y,z}|^n - H_{x,y,z}|^{n-1}) \tag{23}$$

$$M_{x,y,z}|^{n+\frac{1}{2}} = \frac{1}{2}(3M_{x,y,z}|^n - M_{x,y,z}|^{n-1}) \tag{24}$$

Now, all components on the right side of equations (23) and (24) are known, however, it is not yet possible to compute the magnetisation vector at time step $n + 1$ in the time marching scheme because space synchronism has not been applied.

In the Yee's cell, the $\mathbf{M}$ components are evaluated at the same spatial location as the $\mathbf{H}$ components. Therefore when any component of the magnetisation vector say M_x is being computed at a given point, say $(i + \frac{1}{2}, j)$, the y and z components of $\mathbf{H}$ and $\mathbf{M}$ used to compute $\mathbf{M_x}$ are located at different space locations as shown in Figure 1.

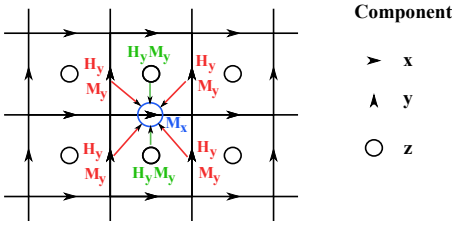

Fig. 1. Reallocation of components in a 2D Yee's cell for space synchronisation.

Thus, all the components in equations (23) and (24) must be reallocated to M_x position. This is done by interpolation of all components surrounding M_x in the Yee's cell [15]. This can be easy understood by a graphical example. Figure 1 represents the space synchronism operations needed to compute M_x (blue circle) where M_y at spatial point $(i+\frac{1}{2}, j)$ will be the average of the four M_y components surrounding Mx in Figure 1. This is the operation represented by the red arrows denoted below as $M_y\_M_x$.

$$M_y\_M_x|_{i+\frac{1}{2},j}^{n+\frac{1}{2}} = \frac{1}{4}\left(M_y|_{i,j-\frac{1}{2}}^{n+\frac{1}{2}} + M_y|_{i,j+\frac{1}{2}}^{n+\frac{1}{2}} + M_y|_{i+1,j-\frac{1}{2}}^{n+\frac{1}{2}} + M_y|_{i+1,j+\frac{1}{2}}^{n+\frac{1}{2}}\right) \quad (25)$$

The same must be done with $H_y\_M_x$ (red arrows operation)

$$H_y\_M_x|_{i+\frac{1}{2},j}^{n+\frac{1}{2}} = \frac{1}{4}\left(H_y|_{i,j-\frac{1}{2}}^{n+\frac{1}{2}} + H_y|_{i,j+\frac{1}{2}}^{n+\frac{1}{2}} + H_y|_{i+1,j-\frac{1}{2}}^{n+\frac{1}{2}} + H_y|_{i+1,j+\frac{1}{2}}^{n+\frac{1}{2}}\right) \quad (26)$$

In a similar way $M_z\_M_x$ (M_z to compute M_x) is described by the operation represented by green arrows.

$$M_z\_M_x|_{i+\frac{1}{2},j}^{n+\frac{1}{2}} = \frac{M_z|_{i+\frac{1}{2},j-\frac{1}{2}}^{n+\frac{1}{2}} + M_z|_{i+\frac{1}{2},j-\frac{1}{2}}^{n+\frac{1}{2}}}{2} \quad (27)$$

The same must be done with $H_z\_M_x$ if any (green arrows operation).

$$H_z\_M_x|_{i+\frac{1}{2},j}^{n+\frac{1}{2}} = \frac{H_z|_{i+\frac{1}{2},j-\frac{1}{2}}^{n+\frac{1}{2}} + H_z|_{i+\frac{1}{2},j-\frac{1}{2}}^{n+\frac{1}{2}}}{2} \quad (28)$$

H_x and M_x to compute M_x will remain the same as they are already in the same spatial position as M_x.

$$M_x\_M_x|_{i+\frac{1}{2},j}^{n+\frac{1}{2}} = M_x|_{i+\frac{1}{2},j}^{n+\frac{1}{2}} \quad (29)$$

$$H_x\_M_x|_{i+\frac{1}{2},j}^{n+\frac{1}{2}} = H_x|_{i+\frac{1}{2},j}^{n+\frac{1}{2}} \quad (30)$$

Then the values obtained from (25) to (30) are used in (20) to calculate $f(H_x, H_y, H_z, M_x, M_y, M_z)$ at time step $n+1/2$. To finish the computation of $M_x|^{n+1}$ the previous result and the known value of M_x at time n are introduced in (19).

The purpose of all these operations referred here as space and time synchronism is to maintain the second order accuracy in the differentiating scheme.

V. Boundary Conditions

From the minimisation of the total energy in a magnetic material, the following boundary condition is derived [16], [17]:

$$\frac{\partial \mathbf{M}}{\partial \mathbf{n}} = 0 \quad (31)$$

where **n** is the direction normal to the material surface. For example, solving (31) at the left boundary of the material ($n = -x$) involves the following operations

$$M_x|_{i+\frac{1}{2}} = M_x|_{i+\frac{3}{2}} \quad (32)$$

$$M_y|_i = M_y|_{i+1} \quad (33)$$

$$M_z|_{i+\frac{1}{2}} = M_z|_{i+\frac{3}{2}} \quad (34)$$

and similar equations would apply for other directions of **n**.

The perfectly matched layer (PML) around the computational space used in normal FDTD to absorb the outgoing waves can be used for the extended method as far as the magnetic material is surrounded by the computational space and not in contact with the PML areas. This is based on the fact that the magnetisation vector has zero value outside the material (it doesn't exist) therefore the extended equations without the magnetisation are the same as in the normal FDTD method.

VI. Stability of the Extended Method

Due to the rotation of the magnetisation in a magnetic material another upper limit in Δt must be considered to make a stable solution for LLG equation. The worst case happens when damping is neglected and a strong field is applied in one direction, therefore the magnetisation describes a circular movement perpendicular to the applied field with a precession angular frequency $\omega_0 = \gamma H$ which in this particular case will be equal to the maximum rotational angular frequency of the magnetisation. Then, the equation of

motion can be written as:

$$\left.\begin{aligned}\frac{dM_x}{dt} &= \omega_0 M_y \\ \frac{dM_y}{dt} &= -\omega_0 M_x \\ \frac{dM_z}{dt} &= 0\end{aligned}\right\} \tag{35}$$

In order to obtain an equation explicitly for, say M_x, expression (35) must be differentiated to give:

$$\frac{d^2 M_x}{dt^2} = \omega_0 \frac{dM_y}{dt} \tag{36}$$

Substituting dM_y/dt from (35) into (36) yields the ordinary differential equation for M_x:

$$\frac{d^2 M_x}{dt^2} = -\omega_0^2 M_x \tag{37}$$

Applying central finite differences to this equation:

$$\frac{M_x^{n+1} - 2M_x^n + M_x^{n-1}}{(\Delta t)^2} = -\omega_0^2 M_x^n \tag{38}$$

and solving for M_x^{n+1} yields the explicit time marching scheme for M_x

$$\begin{aligned} M_x^{n+1} &= 2M_x^n - M_x^{n-1} - \omega_0^2 \Delta t^2 M_x^n \\ &= M_x^n (2 - \omega_0^2 \Delta t^2) - M_x^{n-1} \end{aligned} \tag{39}$$

Using a complex exponential solution $M_x = M_s e^{j\omega_0 t}$ and substituting in (39) gives

$$e^{j\omega_0 (n+1)\Delta t} = e^{j\omega_0 n \Delta t}(2 - \omega_0^2 \Delta t^2) - e^{j\omega_0 (n-1)\Delta t} \tag{40}$$

Expanding the exponential terms and applying Euler's relation to the exponential terms gives

$$2\cos(\omega_0 \Delta t) = 2 - \omega_0^2 \Delta t^2 \tag{41}$$

Equation (41) relates the angular frequency of the system to the time increment. Furthermore

$$\omega_0 \Delta t = \cos^{-1}\left(1 - \frac{\omega_0^2 \Delta t^2}{2}\right) = \cos^{-1}\xi \tag{42}$$

As in the general case for non-magnetic materials, stability is found for the values of ξ that make $\omega_0 \Delta t$ in equation (42) to be real. For values of ξ outside the interval -1 and 1, the function $\cos^{-1}\xi$ will be complex valued and therefore the rotation of magnetisation will produce an unstable solution. At the limits of the above interval

$$\xi = 1 - \frac{\omega_0^2 \Delta t^2}{2} = 1 \quad \rightarrow \quad \Delta t = 0 \tag{43}$$

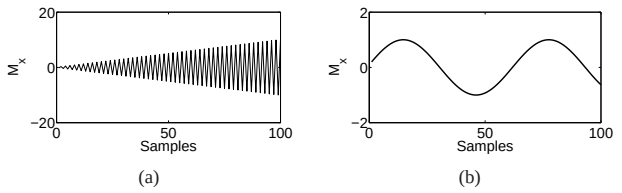

Fig. 2. Solution of (37) sampled with (a) $\Delta t = 2/\omega_0$ which makes the system unstable and (b) $\Delta t = 0.1/\omega_0$ which makes the system stable.

$$\xi = 1 - \frac{\omega_0^2 \Delta t^2}{2} = -1 \quad \rightarrow \quad \Delta t = \frac{2}{\omega_0} \tag{44}$$

Therefore defining the range of Δt for the stable solution of the oscillator equation (37)

$$0 < \Delta t < \frac{2}{\omega_0} = UpperBound \tag{45}$$

This is clearly understood by an example. Figure 2(a) represents a sampled solution of (37) with a sampling rate of $\Delta t = 2/\omega_0$ which is just over the limit in (45) therefore the system is unstable and the solution grows to infinity as time goes on. Figure 2(b) is an example of a stable solution where $\Delta t = 0.1/\omega_0$ implies a stable solution. Although equation (45) defines the stable range when the magnetisation is introduced, the general equation that rules the stability of the FDTD method still needs to be considered as

$$\Delta t > 1 \Big/ c\sqrt{\tfrac{1}{(\Delta x)^2} + \tfrac{1}{(\Delta y)^2}} \equiv \Delta t_{stable\ limit_{2D}} \tag{46}$$

Therefore the time increment of the system Δt must be bounded in such a way that satisfies both (45) and (46) to avoid instability.

To finalise with the stability section, the solution to LLG equation is convergent when the magnetisation is aligned with the applied field or expressed mathematically as

$$\frac{|\mathbf{M} \times \mathbf{H}|}{|\mathbf{M}| \cdot |\mathbf{H}|} \approx 1 \tag{47}$$

This then provides a test of convergence in the numerical implementation.

VII. Experiment Set Up and Results

Figure 3 represents the head diagram used for the simulations. Both geometry and dimensions were taken from an actual Seagate head manufactured in 1997 trhough electron microscope imaging. Two snapshots of the magnetic field strength during simulation

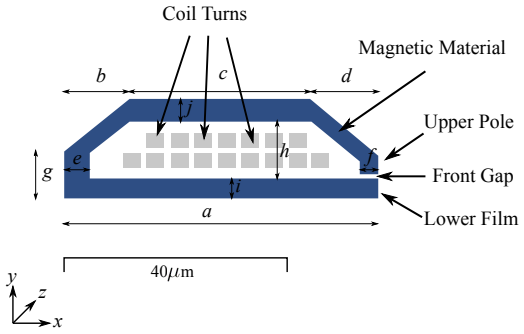

Fig. 3. Scaled diagram of the head geometry with dimensions: front gap height= 0.5μm, a= 56.7μm, b= 11.5μm, c= 33.3μm, d= 11.9μm, e= 4.6μm, f= 2.7μm, g= 10.2μm, h= 12.4μm, i= 4.6μm, j= 4.6μm. For simulation purposes the axis are taken as shown where the *z*-axis represents the anisotropy axis.

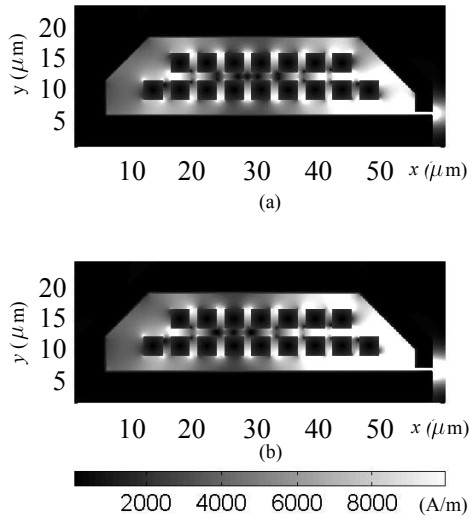

Fig. 4. Magnetic field magnitude for two time instants, (a) $t = 0.2$ns and (b) $t = 0.45$ns, computed using the standard FDTD algorithm (no magnetisation is considered) and a 15mA current step excitation with rise time constant 20ps.

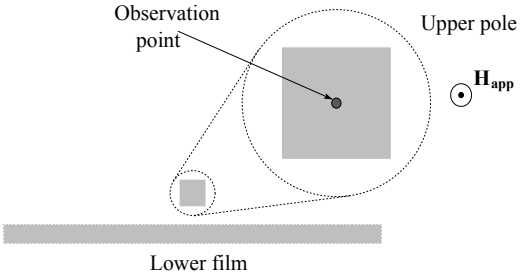

Fig. 5. Configuration of the upper pole simulation in the TE_z mode. Only the zoomed image of the upper pole is defined in the simulation. The excitation is applied uniformly as indicated by $\mathbf{H_{app}}$.

in the TMz mode are shown in Figure 4. Figure 5 represents the configuration used to carry out simulations of the upper pole of head A in TEz mode. These were aimed to study the effects of eddy currents on the switching time due to a field step applied perpendicular to the plane of the paper, with 20ps time constant and 12×10^3A/m amplitude. The simulation parameters were $\Delta x = 0.5\mu$m, $\Delta t = 0.83333$fs and total simulation time 1ns. With regards to material properties, three types of materials were considered: a perfect conductor for the coil turns, a magnetic material for the head core and an isolating material between them. The coil turns were defined by a conductivity $\sigma = 5.8 \times 10^7$ (1/Ωm) and a relative permittivity $\epsilon_r = 4.8$; The magnetic material was defined by a low electrical conductivity $\sigma = 5000$ (1/Ωm), saturation magnetisation $M_s = 800 \times 10^3$ (A/m) initially oriented in the y direction, damping coefficient $\alpha = 0.1$ (μm), uniaxial anisotropy with $H_k = 400$ (A/m) and anisotropy constant $K_u = 200$ (J/m^3), and exchange stiffness constant $A_x = 1.0 \times 10^{-11}$ (J/m); The isolating material was defined by $\epsilon_r = 1$, $\mu_r = 1$ and $\sigma = 0$. Demagnetising fields were included as another term in the direction of the applied field into the effective field expression. Considering the head pole as an infinite cylinder, the demagnetising energy can be expressed as

$$\mathcal{E}_{demag} = \frac{\mu_0}{2}(N_x M_x^2 + N_y M_y^2 + N_z M_z^2) \qquad (48)$$

where due to the cylindrical geometry and orientation in the *z* direction, $N_x = N_y = 1/2$ and $N_z = 0$. Then

$$\mathcal{E}_{demag} = \frac{\mu_0}{2}\left(\frac{M_x^2}{2} + \frac{M_y^2}{2}\right) \qquad (49)$$

The applied energy can be expressed as

$$\mathcal{E}_h = -\mu_0 \mathbf{M}\mathbf{H_{app}} \qquad (50)$$

where $\mathbf{H_{app}} = H_z\mathbf{k}$, then

$$\mathcal{E}_h = -\mu_0 M_z H_z \qquad (51)$$

Now, considering the total free energy as the applied and demagnetising field contributions

$$\mathcal{E}(\mathbf{M}) = \frac{\mu_0}{2}\left(\frac{M_x^2}{2} + \frac{M_y^2}{2}\right) - \mu_0 M_z H_z \qquad (52)$$

or by normalising by $\mu_0 M_s$

$$\hat{\mathcal{E}}(\mathbf{m}) = \frac{1}{4}(m_x^2 + m_y^2) - m_z h_z \qquad (53)$$

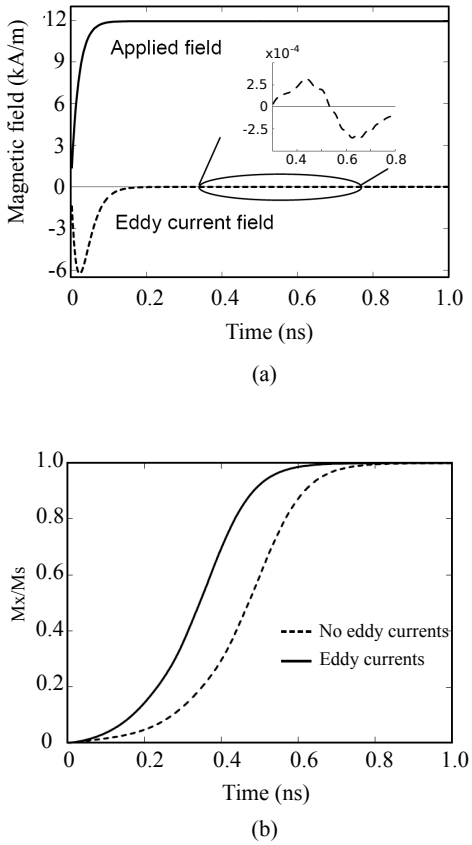

Fig. 6. Eddy current effect at the head pole. (a) Applied field and corresponding eddy current field. (b) Out of plane magnetisation versus time showing a 0.13ns delay in the precessional switching of the magnetisation.

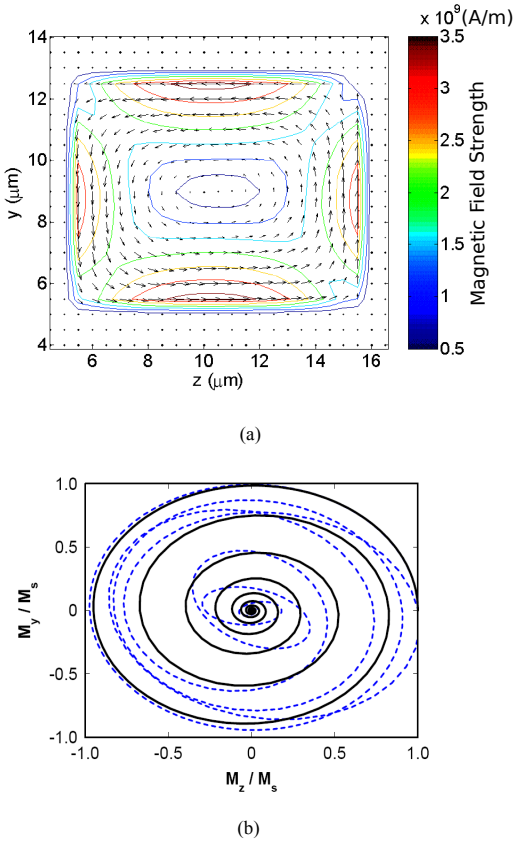

Fig. 7. Eddy current effect at the head pole. (a) Contour and arrow plot of the current density (A/m^2) at 0.02ns. (b) Magnetisation precession with (dashed plot) and without (solid plot) eddy current fields.

Since $m_x^2 + m_y^2 + m_z^2 = 1$, then

$$\hat{\mathcal{E}}(\mathbf{m}) = \frac{1}{4}(1 - m_z^2) - m_z h_z \tag{54}$$

which concludes with effective field expression as

$$\mathbf{h_{eff}} = -\frac{\partial \hat{\mathcal{E}}}{\partial \mathbf{m}} = \left(\frac{m_z}{2} + hz\right)\mathbf{k} \tag{55}$$

The magnetic fields and the magnetisation were evaluated at the center of the head pole. Figure 6(a) shows that eddy currents produce opposing fields to the applied field that turns out to trigger the precessional switching of the magnetisation. Analysing the plot in Figure 6(b), when eddy currents are not considered, a delay of 0.13ns is observed in the switching time of the magnetisation, which causes a slower head field response in agreement with the literature. The expanded plot in Figure 6(a) represents eddy current field due to $\partial M/\partial t$ which is negligible. Figure 7(a) shows the current density across the head pole, its distribution agrees with the theory of eddy currents that can be found in the literature. The eddy current fields trigger the switching of the magnetisation and also modify its precession as can be seen in Figure 7(b).

Figure 8 shows the magnetic field distribution near the gap region at time 0.45ns for both the standard and the extended FDTD algorithms. By comparison, it is observed that when using the extended method, the field strength is smaller and the effective field concentrates at the head corners. As explained above, these effects are due to the switching of the magnetisation and the demagnetising fields. The arrow plot of Figure 8(b) represents the orientation of the magnetisation. The direction of the magnetic flux density can be visualised by observing the orientation of the magnetisation arrows, it is obvious that there is a flux linking both thin films through the gap resulting in the external radiation of the write field.

Figure 9 is obtained by plotting the magnetic field

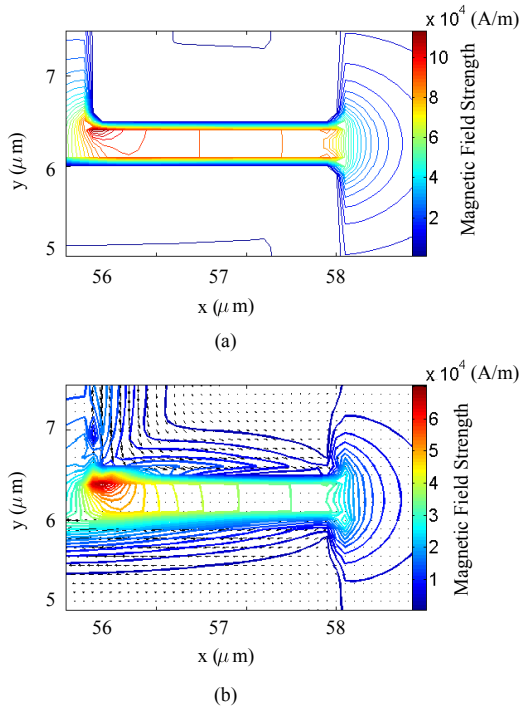

Fig. 8. Magnetic field distribution of the head geometry near the gap region at simulation time 0.45ns. (a) Contour plot of the field strength for linear material and (b) contour plot of the field strength and arrow plot of the magnetisation for non-linear material.

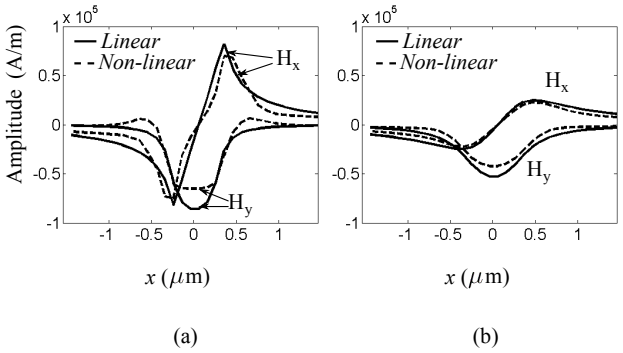

Fig. 9. Recording gap fields simulating a plane parallel to the disk surface in a recording system. (a) Fields at the pole surface and (b) at 100nm from the head surface.

components H_x and H_y at the head surface and at a distance of 100nm from the head surface in the gap region. Here, the x-axis represents distances from the central point of the gap region towards both poles (upper and lower), e.g. $x = 0$ is the value taken in the centre of the gap at a distance of 100nm away from the head, the direction of x is parallel to the disk surface. Having in mind that the disk surface in a recording system would be parallel to this plane, the field magnitude responsible for orientating the magnetisation of the disk in one direction or another will be proportional to the plot in Figure 9. In particular, H_y is the main field responsible for the recording process in longitudinal media. Higher field gradients are observed in the pole corner regions with the inclusion of the magnetic details of the core material. This has the implication that shorter transition lengths are recorded in practice than predicted by models that ignore the magnetic detail of the core material.

The obtained results are in agreement with previous works present in the literature. In [18], a similar delay of 0.25ns was observed when considering a damping coefficient $\alpha = 0.1$, which triggers the precession of the magnetisation. The same conclusions were drawn in [19] with respect to the precession of the magnetisation: eddy currents introduce an eddy current field that triggers the precession. In [20], a faster magnetisation switching was also observed, it was triggered by the eddy currents which turned out into a slower head field response. In [21], authors agree with the fact that the effect of eddy currents is completely different when considering micromagnetic level models and thus the effect of the magnetisation can not be represented by an equivalent permeability. Also, predicted gap field distributions showed a more accurate field description near the head poles when compared against simpler head models, e.g. Karlqvist [22].

Regarding the memory requirement, in order to store each sample, the extended FDTD simulation requires 153,558,419 bytes, figure which is, without surprise, above the amount of memory that uses the standard FDTD method to simulate the same head structure, 26,345,603 bytes. With respect to the calculation time, the time increment in between consecutive iterations of an FDTD execution is directly related to the spatial resolution of the grid in the FDTD algorithm, stability equations (45) and (46). The grid resolution is determined by the most restrictive of two factors: the smallest feature in the simulated structure or the shortest wavelength in the simulated space. In this particular case, where a magnetic head has been simulated, the very small front gap height for the head geometry in Figure 3 determined a very small time increment resulting in a large number of iterations. Thus, a small grid resolution results in a very small time increment and therefore large simulation time (CPU time) to obtain the results of a single simulation

(the TM_z Matlab simulation took fifty days overall on a 2GHz machine, with 2GB of RAM, running on Windows XP). Large waiting time requirements have made it impossible to carry out several simulations and other tests over very small head structures.

VIII. Conclusion

This investigation aimed at developing a numerical simulation approach that simultaneously incorporates the fundamental micromagnetic and electromagnetic details of magnetic materials to study the fast switching process in soft magnetic materials in general, and in thin-film inductive writers in particular.

This work successfully met all its original objectives by developing a numerical technique for simulating the dynamic behaviour of magnetic materials and devices. This technique naturally combines the fundamental equation of magnetisation motion with the solution of Maxwell's equations using the Finite- Difference Time-Domain method, with the unique feature that the micromagnetic (including exchange and anisotropy effects) and electromagnetic (electric and magnetic fields due to charges and currents) descriptions of simulated structures are produced simultaneously.

Using this technique will help to design and study complete magnetic devices without ignoring the interaction between the magnetic material and other dielectric and conductive layers in the structure, which is important at high frequencies. Moreover, this feature simplifies the magnetostatic computations which are inherently demanding in numerical micromagnetics, thus extending existing work in micromagnetics to more complex geometries and applications.

References

[1] R. J. Hicken, N. D. Hughes, J. R. Moore, D. S. Schmool, and J. W. R. Wilks, "Magneto-optical studies of magnetism on pico and femtosecond time scales," *Journal of Magnetism and Magnetic Materials*, vol. 242-245, no. 1, pp. 559–564, 2002.

[2] C. H. Back, J. Heidmann, and J. M. Cord, "Time resolvel kerr microscopy: Magnetisation dynamics in thin film write heads," *Magnetics, IEEE Transactions on*, vol. 35, pp. 637–642, 1999.

[3] B. K. Middleton, J. J. Miles, and M. M. Aziz, "Switching times and transition widths in digital recording theory," *Magnetics, IEEE Transactions on*, vol. 37, pp. 1327–1329, 2001.

[4] I. Tagawa, T. Koshikawa, and Y. Sasaki, "High performance write head for 10 krpm hdd with high data rate recording up to 45 mb/s," *Magnetics, IEEE Transactions on*, vol. 36, no. 1, pp. 177–182, 2000.

[5] G. Rubinacci, A. Tamburrino, and S. Ventre, "Eddy Current Imaging of Surface Breaking Defects by Using Monotonicity Based Methods," *Applied Computational Electromagnetics Society (ACES) Journal*, vol. 23, no. 1, pp. 46–52, 2008.

[6] H. Engstrom, "Equivalent circuit of a thin film recording head," *Magnetics, IEEE Transactions on*, vol. 20, no. 5, pp. 842–844, 1984.

[7] A. Paton, "Analysis of the efficiency of thin film magnetic recording heads," *J. Appl. Phys.*, vol. 42, no. 13, pp. 5868–5870, 1971.

[8] R. E. Jones, "Analysis of the efficiency and inductance of multiturn thin film magnetic recording heads," *Magnetics, IEEE Transactions on*, vol. 14, no. 5, pp. 509–511, 1978.

[9] T. Arnoldussen, "A modular transmission line/reluctance head model," *Magnetics, IEEE Transactions on*, vol. 24, no. 6, pp. 2482–2484, 1988.

[10] N. Yeh, "Analysis of thin film head with a generalized transmission line model," *Magnetics, IEEE Transactions on*, vol. 18, no. 1, pp. 233–237, 1982.

[11] F. Liu, S. Shi, J. Wang, Y. Chen, K. Stoev, L. Leal, R. Saha, H. Tong, S. Dey, and M. Nojaba, "Magnetic recording at a data rate of one gigabit per second," *Magnetics, IEEE Transactions on*, vol. 37, no. 2, pp. 613–618, 2001.

[12] K. Gao and H. N. Bertram, "Three dimensional micromagnetic analysis of write head dynamics and field patterns," *Magnetics, IEEE Transactions on*, vol. 37, no. 4, pp. 1373–1375, 2001.

[13] S. Hagness and A. Taflove, *Computational Electrodynamics, the Finite Difference Time Domain Method*. Artech House, 2000.

[14] T. L. Gilbert, "A lagrangian formulation of the gyromagnetic equation of the magnetic field," *Physical Review*, vol. 100, 1955.

[15] M. Okoniewski and E. Okoniewska, "FDTD analysis of magnetized ferrites: a more efficient algorithm," *Microwave and Guided Wave Letters, IEEE*, vol. 4, no. 6, pp. 169–171, 1994.

[16] W. F. Brown, *Micromagnetics*. Robert E. Krieger publishing company Huntington, New York, 1978.

[17] A. Aharoni, *Introduction to the Theory of Ferromagnetism*. Oxford Science Publications, 2nd ed., 2000.

[18] L. Torres, L. Lopez-Diaz, E. Martinez, and O. Alejos, "Micromagnetic dynamic computations including eddy currents," *Magnetics, IEEE Transactions on*, vol. 39, pp. 2498 – 2500, sept. 2003.

[19] G. Hrkac, T. Schrefl, O. Ertl, D. Suess, M. Kirschner, F. Dorfbauer, and J. Fidler, "Influence of eddy current on magnetization processes in submicrometer permalloy structures," *Magnetics, IEEE Transactions on*, vol. 41, pp. 3097 – 3099, oct. 2005.

[20] K. Takano, X. Zhang, E.-A. Salhi, L. Guan, M. Sakai, J. Smyth, and M. Dovek, "Micromagnetics and eddy current effects in magnetic recording heads," *Magnetics, IEEE Transactions on*, vol. 43, pp. 2184 –2186, june 2007.

[21] E. Della Torre and J. Eicke, "Eddy currents in micromagnetic calculations," *Magnetics, IEEE Transactions on*, vol. 33, pp. 1251 –1254, mar 1997.

[22] O. Karlqvist, "Calculation of the magnetic field in the ferromagnetic layer of a magnetic drum," *Trans. Roy. Inst. Techno., Stockholm*, no. 86, pp. 3 –27, 1954.

GPU implementation of the Modified Equivalent Current Approximation (MECA) method

Luis E. Tirado[1], José Á. Martínez-Lorenzo[1], Borja González-Valdés[1], Carey Rappaport[1], Oscar Rubiños-López[2], Hipólito Gómez-Sousa[2]

[1] Department of Electrical Engineering
Northeastern University, Boston, MA 02115, USA
{ltirado, jmartine, bgonzale, rappapor}@ece.neu.edu

[2] Department of Signal Theory and Communications
University of Vigo, ETSI de Telecomunicación, Campus Universitario, E-36310 Vigo, Spain
{oscar, hgomez}@com.uvigo.es

Abstract ─ This paper investigates two different methods of implementing the Modified Equivalent Current Approximation (MECA) method using CUDA parallel programing and computing platform [1]. The MECA method allows the analysis of dielectric and lossy geometries and reduces to the well-studied Physical Optics (PO) formulation in case of PEC caterers [2]. We discuss the implementation details and performance of using both an add-on toolbox for MATLAB™ to offload computations to the GPU, as well as porting MECA code to CUDA directly. We show through simulations that both methods are effective at significantly reducing the MECA algorithm computation time.

Index Terms ─ CUDA, GPGPU, MECA, parallel programming, Physical Optics.

I. INTRODUCTION

There are various methods to compute the effects of a wave scattered from arbitrary objects. Full-wave methods, like the Method of Moments (MoM) are very precise, but computationally intensive. Physical Optics methods, which approximate currents by a tangent plane method, are less accurate but faster. MECA is a good compromise, calculating equivalent currents based on oblique incidence of a plane wave on the interface together with a field decomposition into transverse electric (TE) and transverse magnetic (TM) components [3].

The current implementation of MECA using CPUs carries a heavy computational load when evaluated at multiple frequencies and observation points in different aspect angles and incident directions. However, with the recent rise in availability of Graphics Processing Unit (GPU) computing, the most processing intensive parts of the MECA code can be evaluated exactly without any approximations or interpolations at higher speeds. Parallelization using GPUs is desired for the MECA algorithm given that the algorithm is being implemented as a forward model in a personnel screening portal-based real-time whole body imaging system [4]. The Department of Homeland Security (DHS), through its mission of preventing terrorism and enhancing security, requires a high throughput, accurate, and quick detection of person-borne threats in highly secure areas. DHS calls for a security checkpoint throughput of 200-250 persons/hour. For this reason, it is essential to be able to model the scattered electric and magnetic fields from the person under test as fast as possible.

In order to reduce the total runtime of MECA, two distinct approaches have been developed. Our first approach consists of using AccelerEyes Jacket [5] GPU engine for MATLAB™ to create a vectorized version of the existing MECA code. Jacket automatically wraps MATLAB™ code into a GPU compatible form, allowing a programmer to extend existing code to parallel processing with minimal effort. The second approach is to port

Submitted On: Jan. 19, 2012
Accepted On: July 22, 2012

existing MECA code in C directly to CUDA. This paper will detail the implementation details and performance of both methods.

The paper is divided as follows. Section II gives an overview of the MECA method and briefly describes the platform used for computation. In Section III, the GPU architecture and two approaches to speed up the MECA code are discussed, while Section IV details the performance results obtained.

II. MECA OVERVIEW

The MECA method described in [2] and [3] calculates the currents from scattering objects that need not be perfect electric conductors (PEC). The objects may be dielectrics or even lossy, and MECA provides comparable results to full wave methods such as Method of Moments (MoM), except at grazing angles, where diffraction effects become more pronounced. The part of most concern in this paper is the calculation of the electric and magnetic fields given the inputs of magnetic and electric currents, observation directions, and the faceted object geometry representation, as this is the most time consuming part of the algorithm.

The MECA algorithm calculates the scattered electric field $\boldsymbol{E_k^s}$ at the observation point P_{obs} as the sum of the contributions of all the facets *i* of a given mesh geometry as [8]:

$$\boldsymbol{E_k^s} = \frac{j}{2\lambda}\sum_i \frac{e^{-jk_1 r_{ik}}}{r_{ik}}\left[\boldsymbol{E_{ik}^a} - \boldsymbol{\eta_1 H_{ik}^a} \times \hat{\boldsymbol{r}}_{ik}\right], \quad (1)$$

where λ is the wavelength used, j is the imaginary unit, k_1 is the wavenumber of the first medium, $\boldsymbol{E_{ik}^a}$ and $\boldsymbol{H_{ik}^a}$ are the electric and magnetic fields at the observation vector $\boldsymbol{r_k}$ as defined in [3], $\boldsymbol{\eta_1}$ is the intrinsic impedance of the first medium, and $\boldsymbol{r_{ik}} = r_{ik}\hat{\boldsymbol{r}}_{ik}$ is the position vector from the *i*-th facet centroid $\boldsymbol{r_i}$ to the observation vector $\boldsymbol{r_k}$. The magnetic field is calculated in a similar manner. Figure 1 denotes the notation of the position vectors used for an oblique wave incidence in a faceted geometry.

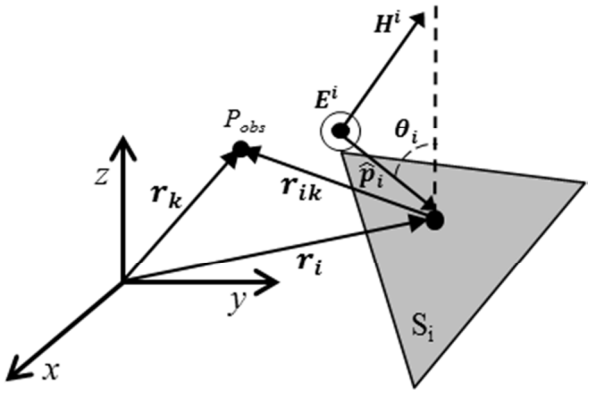

Fig. 1. Position vectors, observation point P_{obs}, propagation vector $\hat{\boldsymbol{p}}_{\boldsymbol{i}}$, angle of incidence θ_i, incident electric and magnetic fields, and facet S_i.

III. GPU IMPLEMENTATION DETAILS

A. Fermi CUDA architecture

The Fermi parallel architecture in the Tesla C2070 GPU consists of a Single Instruction Multiple Data (SIMD) processor with 14 Streaming Multiprocessors (SM). Each SM design contains 32 Streaming Processors (SPs), also called CUDA cores, 32,768 registers and 64 KB of RAM with a configurable partitioning of shared memory and L1 cache [7]. Each SM can run a variable number of threads, and the local resources are divided among them [1]. A thread on the GPU is a basic element of the data to be processed. Threads are grouped into blocks which can contain 64 to 1024 threads. Blocks are grouped together into a grid. A kernel is a code function that is executed by the CUDA device using the number of specified blocks and threads (see Fig. 2).

The CPU and GPU maintain their own DRAM and address spaces, respectively called host and device memory. Device memory can be of different types: global, shared, and constant. Table 1 lists the differences between these memory types.

Table 1: CUDA memory types

Memory	Scope	Lifetime	Access
global	grid	application	slow read/write
shared	block	kernel	fast read/write
constant	grid	application	cached read only

A challenge in developing MECA on NVIDIA CUDA enabled GPUs is making the most effective use of the platform's memory system and

resources. In addition, the productivity of GPUs under different programming paradigms can be significant depending on the application [8], which brings forth the two subsequent approaches.

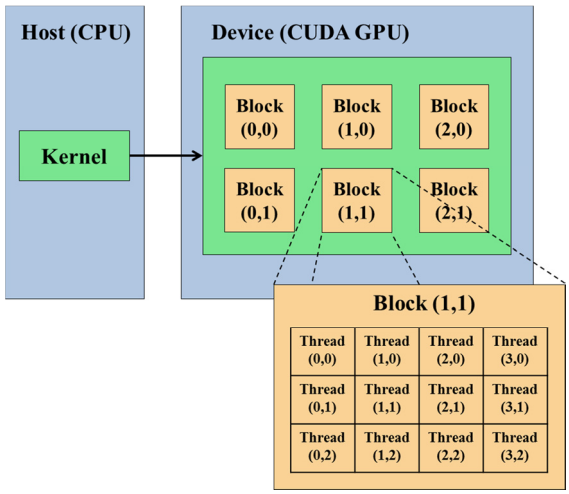

Fig. 2. CUDA Threading model.

B. JACKET GPU engine implementation

The first approach to parallelizing the existing MATLAB code is to vectorize the arithmetic operations. MATLAB and GPU computing both tend to perform best on vectorized code. The same is also true of Jacket, especially for element-wise operations which are performed just-in-time, *i.e.* they are batched together and performed in a single kernel.

Once the code is vectorized, input data is cast to Jacket's GPU data structure, allowing real-time compile-on-the-fly calculations and memory management on the GPU behind-the-scenes. Functions called on GPU data execute on the GPU automatically without any extra programming.

As an example, assume that there are 80,000 facets (`nT`), and 181 observation points (`nr`) in the polar angle $\boldsymbol{\theta}$ sweep for a single circumferential angle $\boldsymbol{\phi}$ in our simulation. The single-threaded MATLAB implementation relies on a loop that iterates over the observation points, calculating the electric and magnetic field x, y, and z components for each point. The Jacket GPU implementation, however, reshapes the intermediate data quantities into single matrices of size `(3, nT*nr)`, which eliminates looping, and many GPU threads work at the same time to compute the output fields in steps. The end result is that the GPU multiprocessor occupancy is increased up to 72% for the example case, and thus, the vectorized code runtime is reduced as compared to the single-threaded for-loop version of the code.

One disadvantage of this type of vectorization is that, for the example case, up to 2.5 GB of GPU memory is allocated to perform the calculations. In order to be able to process a larger data set, the algorithm needs to be broken down into chunks, and many intermediate calculations are repeated. The data chunks then have to be arranged to match the original output format. Thus, for each additional $\boldsymbol{\phi}$ cut in our example, the computational time is doubled due to memory constraints. Even though the MECA runtime is reduced with the Jacket code, there is still room for improvement in reducing memory usage and maximizing GPU resource occupancy.

C. CUDA C code implementation

It was advantageous to reuse the existing structure of an already existing and validated version of the MECA code ported to C [2]. In the OpenMP C version of MECA, the sum in Eq. (1) is calculated in series by use of an accumulating variable. Figure 3(a) shows the implementation of the scattered field computations for the OpenMP C version of the code.

In the CUDA version of MECA, changes must be made to account for the GPU architectural differences to avoid having many threads writing to the same memory address, resulting in a race condition. Without modifying the C code, atomic operations would be necessary to compute the sum in Eq. (1). Atomic operations read, modify, and write back a value to memory without interfering with other threads. However, the GPU cannot perform many atomic operations without considerable delays. In our example with 80,000 facets, the computations using atomic operations are one order of magnitude slower than the single threaded MATLAB implementation of MECA.

The CUDA implementation strategy is shown in Fig. 3(b). In order to avoid atomic operations, we structure the code to use one GPU thread to do intermediate calculations for each facet in the input geometry. For our example from the previous section, 256 threads per block are instantiated, so we end up using `ceil(nT/256) = 313` blocks. Given that the current NVIDIA Fermi architecture allows for up to 65,536 blocks of up to 1024 threads each, it is clear that a large number of facets can be

evaluated in parallel limited only by GPU memory constraints.

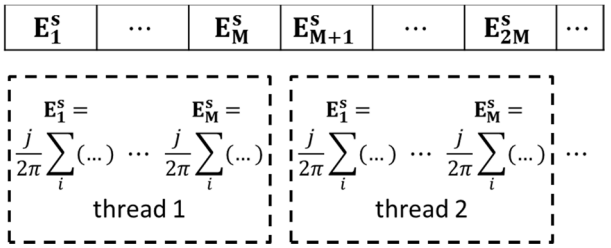

a) Each thread computes for a set of observation points (OpenMP C approach)

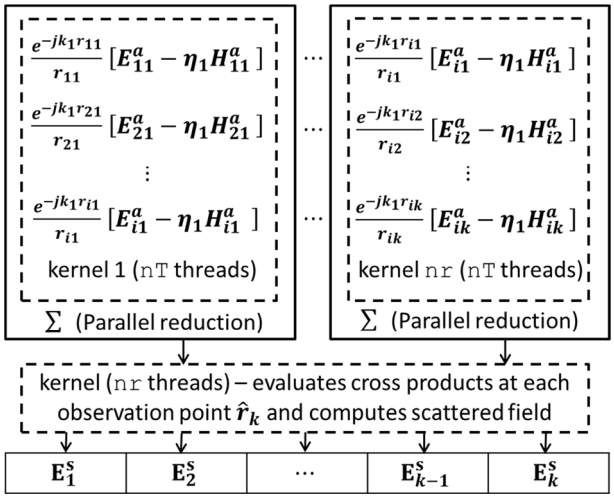

b) nT threads compute part of Eq. (1) in nr kernels, parallel reduction, last kernel (nr threads) computes field (CUDA C approach)

Fig. 3. OpenMP & CUDA MECA implementations

More explicitly, the CUDA code begins by copying the variables used by the algorithm into the GPU's global memory. Next, nr kernels are launched, in which each of the threads calculates part of the *i*-th term inside the sum in Eq. (1) independently and writes each result to a different index of an array initialized in GPU memory. Subsequently, a parallel reduction algorithm [9] is used to sum all the facet contributions for the *k*-th observation point. This algorithm takes advantage of the most efficient implementation of a parallel sum reduction automatically based on data input size, relying on use of fast shared memory [10]. Lastly, a kernel with nr threads loads the previously-saved reductions for each of the coordinate axes. Next, it evaluates the cross-products of Eq. (1) and the analogous magnetic field equation to compute the real and imaginary parts of the scattered electric and magnetic fields at each observation point $\boldsymbol{r_k}$.

Comparing to the Jacket version, in the example case, only 25 MB of GPU memory is required to perform the computations, and for each additional observation point, only 24 extra bytes of memory are required to be allocated on the GPU, which greatly falls below the memory requirements for the vectorized Jacket version of the code.

Based on the fact that the brute force computation of the scattered far fields is an O(nT*nr) operation, there is a massive amount of parallelism that is exploited by porting the MECA code to CUDA enabled GPUs.

IV. RESULTS

In addition to computing the total runtime results for the Jacket and CUDA implementations, we also compare these to MATLAB code (single threaded) [3] and OpenMP multi-threaded C code developed in [2]. The Jacket and CUDA implementations are also validated against the existing MATLAB and C codes for numerical accuracy. The MECA code has been widely validated with other electromagnetic codes in previous works, [2,3] which compare MECA with other electromagnetic methods. The discussion on accuracy is out of the scope of this paper, which focuses on the speed improvements.

The simulations conducted in this paper are performed using a single workstation 2.8 GHz Intel® Core™ i7 930 quad-core CPU with an NVIDIA Tesla™ C2070 Computing Processor with 6 GB of GDDR5 VRAM. The Tesla™ C2070 contains 448 stream processors running at 1.15 GHz, which has a double precision floating point peak performance of 515 GFLOPs. MATLAB version 7.11.0.584 (R2010b) is used along with Jacket version 1.8.1. The compiled CUDA code and Jacket 1.8.1 both are based on NVIDIA's CUDA version 4.0.

A square plate geometry is used for the performance tests, by varying the number of facets and keeping the number of observations fixed to 722 to compare the performance to the results presented in [2]. The number of facets is kept fixed at 80,000 while the number of observations is varied. The maximum number of facets used in the tests is 8×10^6, and the maximum number of

observations points is 360 θ cuts × 360 ϕ cuts. The plane incident wave frequency is 60 GHz.

Figures 4 and 5 show the runtime for computing Eq. (3) as a function of the number of facets for the CUDA version of the code versus the MATLAB and OpenMP C versions for near and far-fields, respectively. Jacket M code timing results are not included in these figures due to a product limitation in the implementation of the Kronecker tensor product in the Jacket version used to construct vectorized data matrices with more than 1.67×10^7 elements in one dimension.

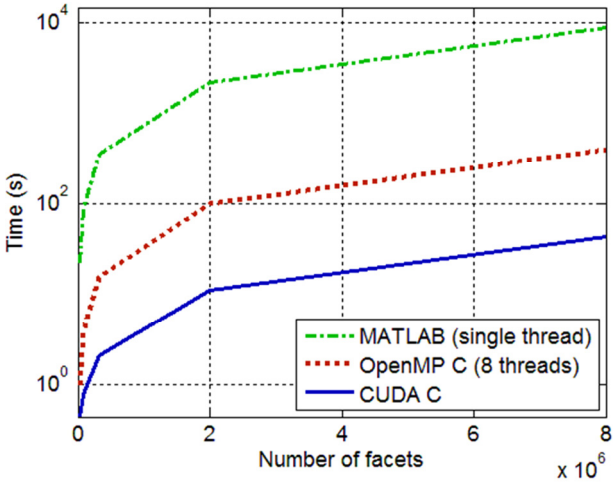

Fig. 4. Runtime vs. number of facets for near-field calculations (722 observations).

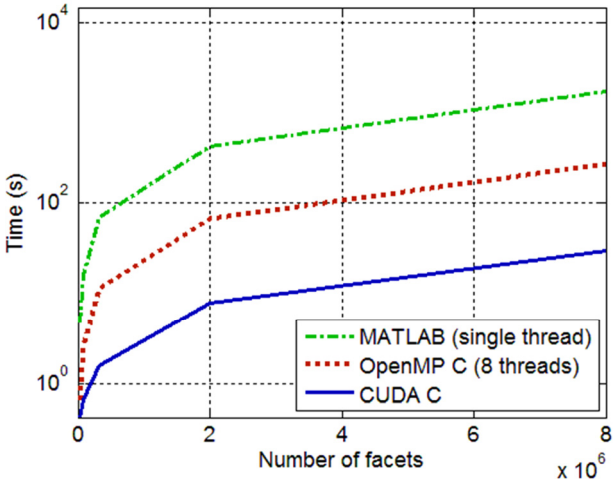

Fig. 5. Runtime vs. number of facets for far-field calculations (722 observations).

The CUDA C implementation is 1.5 to 9.3 times faster than the OpenMP C implementation with GPU multiprocessor occupancy varying from 70 to 100% as a function of the number of facets used in the computations. The algorithm reaches 100% GPU occupancy at 2.9×10^6 facets and 4.5×10^6 facets for the near and far-field versions, respectively.

Figures 6 and 7 show the runtime for computing Eq. (1) for 80,000 facets and a varying number of observations for the MATLAB (single-threaded), OpenMP (multi-threaded), Jacket M, and CUDA C codes for near and far-fields, respectively. From the timing results obtained, we can ascertain that CUDA C code scales linearly with the number of observations in the same way as the MATLAB and OpenMP C versions do.

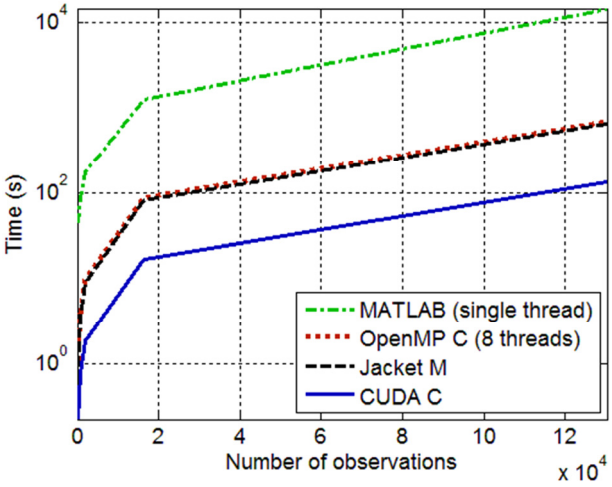

Fig. 6. Runtime vs. number of observations for near-field calculations (80,000 facets).

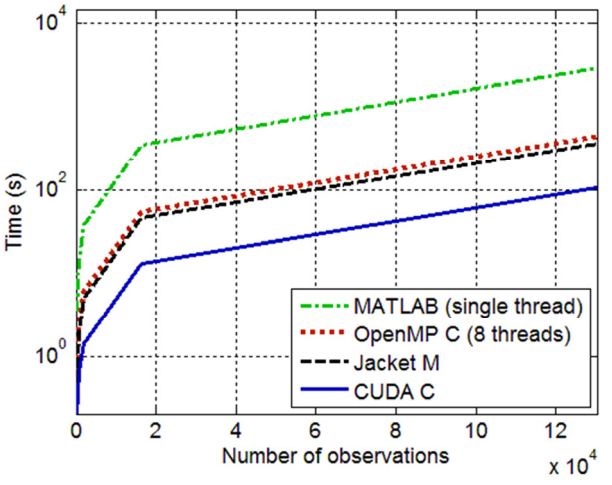

Fig. 7. Runtime vs. number of observations for far-field calculations (80,000 facets).

The Jacket M implementation for 80,000 facets is only 7% to 18% faster than the OpenMP C implementation. This is because the input data needs to be processed in chunks due to the high memory usage required by the vectorization. In addition, the Jacket code GPU multiprocessor occupancy is 72% or 68% for the near and far-field implementations, respectively. The CUDA version for the same number of facets, however, is 80% or 84% efficient for the near and far-fields. It computes all of the data in a single run, which makes it 3.8 to 5.3 times faster than the OpenMP code, a marked performance improvement.

To validate the numerical accuracy of the CUDA implementation, the maximum error between the OpenMP C and CUDA C results is computed for both the near and far-field cases with varying facet numbers from the earlier simulation. The results are shown in Table 2 and Table 3 for near and far-field observations, respectively.

Table 2: CUDA and OpenMP near-field maximum error

Number of facets	Total electric field maximum error (V/m)	Total magnetic field maximum error (A/m)
20000	8.39E-14	2.35E-16
80000	1.07E-13	2.80E-16
320000	1.94E-13	4.85E-16
2000000	6.30E-12	1.68E-14
8000000	8.85E-12	2.37E-14

Table 3: CUDA and OpenMP far-field maximum error

Number of facets	Total electric field maximum error (V/m)	Total magnetic field maximum error (A/m)
20000	2.61E-11	6.92E-14
80000	6.13E-11	1.63E-13
320000	1.23E-10	3.27E-13
2000000	8.43E-10	2.24E-12
8000000	3.82E-09	1.01E-11

The variation of the maximum error difference is due to the parallel sum reduction algorithm used to sum all the facet contributions for each observation point, whereas the OpenMP code adds up the contributions serially. Given that floating point operations are non-commutative, small differences between the CPU and GPU results are expected.

V. CONCLUSION

This paper presents a CUDA version of a modified PO method known as the modified equivalent current approximation (MECA), which is valid for both PEC and dielectric objects. Our results show that the computational performance of the CUDA version is increased up to 9.3 times with respect to the OpenMP C algorithm timings. This shows promise to implement an inverse reconstruction algorithm, taking advantage of the speedup and the excellent numerical accuracy that the CUDA platform provides.

ACKNOWLEDGMENT

This material is based upon work supported by the U.S. Department of Homeland Security under Award Number 2008-ST-061-ED0001. The views and conclusions contained in this document are those of the authors and should not be interpreted as necessarily representing the official policies, either expressed or implied of the U.S. Department of Homeland Security.

REFERENCES

[1] M. Ujaldon, "Using GPUs for Accelerating Electromagnetic Simulations," ACES Journal, vol. 25, no. 4, pp. 294-302, 2010.

[2] H. Gómez-Sousa, J. A. Martínez-Lorenzo, O. Rubiños-López, J. G. Meana, M. Graña-Varela, N. Gonzalez-Valdes, M. Arias-Acuña, "Strategies for Improving the Use of the Memory Hierarchy in an Implementation of the Modified Equivalent Current Approximation (MECA) Method," ACES Journal, vol. 25, no. 10, pp. 841-852, 2010.

[3] J. G. Meana, J. A. Martinez-Lorenzo, F. Las-Heras, and C. Rappaport, "Wave Scattering by Dielectric and Lossy Materials using the Modified Equivalent Current Approximation," IEEE Transactions on Antennas and Propagation, vol. 58, no. 11, pp. 3757-3761, 2010.

[4] J. L. Fernandes, C. Rappaport and D. M. Sheen, "Improved Reconstruction and Sensing Techniques for Personnel Screening in Three-Dimensional Cylindrical Millimeter-Wave Portal Scanning," Proc. SPIE 8022, 802205, 2011.

[5] AccelerEyes, Jacket, Version 1.8.1, http://www.accelereyes.com, Sep. 2011.

[6] C. A. Balanis, *Advanced Engineering Electromagnetics,* 1st ed. New York, USA: John Wiley and Sons, 1989.

[7] NVIDIA, "NVIDIA's Next Generation CUDA™ Compute Architecture: Fermi™," Version 1.1, http://www.nvidia.com/content/PDF/fermi_white_papers/NVIDIA_Fermi_Compute_Architecture_Whitepaper.pdf, 2009.
[8] M. Malik, T. Li, U. Sharif, R. Shahid, T. El-Ghazawi, G. Newby, "Productivity of GPUs under Different Programming Paradigms," Concurrency and Computation: Practice and Experience, vol. 24, no. 2, pp. 179-191, 2012.
[9] J. Hoberock, N. Bell, "Thrust: A Parallel Template Library," V1.3.0, http://www.meganewtons.com, 2010.
[10] NVIDIA, "Thrust Quick Start Guide," Version 01, http://developer.download.nvidia.com/compute/DevZone/docs/html/CUDALibraries/doc/Thrust_Quick_Start_Guide.pdf, Jan. 2011.

Luis Eladio Tirado was born in Mayagüez, Puerto Rico in 1983. He received the B.S. and M.S. degrees in Electrical Engineering from Northeastern University in 2006 and 2008, respectively. He is currently on leave of absence from Raytheon Integrated Defense Systems (IDS) to complete the Ph.D. in Electrical Engineering at Northeastern University, Boston, MA, where he is part of the Awareness and Localization of Explosives-Related Threats (ALERT) Department. His research interests include GPU implementations of forward and inverse millimeter wave models.

José Ángel Martínez-Lorenzo (S'03–M'05) was born in Madrid, Spain, in 1979. He received the M.S. and Ph.D. degrees in telecommunications engineering from the University of Vigo, Vigo, Spain, in 2002 and 2005, respectively.

He was a Teaching and Research Assistant with the University of Vigo from 2002 to 2004. He joined the faculty at the University of Oviedo, Gijón, Spain, in 2004, where he was an Assistant Professor in the area of signal theory and communications until 2006. During spring and summer 2006, he was a Visiting Researcher with the Bernard Gordon Center for Subsurface Sensing and Imaging Systems (Gordon-CenSSIS), Northeastern University, Boston, MA. He was appointed as a Research Assistant Professor with the Department of Electrical and Computer Engineering, Northeastern University. He is currently an active member of the Awareness and Localization of Explosives-Related Threats (ALERT), a Department of Homeland Security Center of Excellence, Northeastern University. He has authored over 80 technical journal and conference papers. His research is geared toward the understanding, modeling, and quantitative prediction of complex electromagnetic problems with special application to security sensing systems, communication systems, and biomedical systems.

Borja González-Valdés was born in Gijon, Spain. He received the Electrical Engineering degree and Ph.D. from the University of Vigo, Spain, in 2006 and 2010 respectively. From 2006 to 2010, he was a research grant holder and then postdoctoral researcher with the Antenna and Optical Communications group at the University of Vigo. During 2008 and 2009, he was a visiting researcher at the Gordon CenSSIS Center, Northeastern University, Boston, USA. In 2011, he joined the ALERT Center of Excellence, Northeastern University, Boston, USA as a Postdoctoral Research Associate. His research interests include antenna design, inverse scattering, advanced imaging techniques, and THz technology.

Carey M. Rappaport (S'80–M'87–SM'96–F'06) received the B.S. degree in mathematics, the B.S., M.S., and E.E. degrees in electrical engineering in 1982, and the Ph.D. degree in electrical engineering in June 1987 from the Massachusetts Institute of Technology (MIT), Cambridge.

He was a Teaching and Research Assistant with MIT from 1981 to 1987 and also with COMSAT Labs, Clarksburg, MD, and The Aerospace Corporation, El Segundo, CA, during summers. In 1987, he joined the faculty at Northeastern University, Boston, MA, where he has been a Professor of electrical and computer engineering since July 2000. During fall 1995, he was a Visiting Professor of electrical engineering with the Electromagnetics Institute, Technical University of Denmark, Lyngby, Denmark, as part of the W. Fulbright International Scholar Program. During the second half of 2005, he was a Visiting Research Scientist with the Commonwealth Scientific Industrial and Research Organization, Marsfield Australia. He has consulted for Geo-Centers, Inc., PPG, Inc., Alion Science and Technology, Inc., and several municipalities on wave propagation and modeling and also on microwave heating and safety. He was a Principal Investigator of an ARO-sponsored Multidisciplinary University Research Initiative on Humanitarian Demining and a Co-Principal Investigator of the NSF-sponsored Bernard Gordon

Center for Subsurface Sensing and Imaging Systems (Gordon-CenSSIS), Northeastern University, Boston, MA. He has authored over 300 technical journal and conference papers in the areas of microwave antenna design, electromagnetic wave propagation and scattering computation, and bioelectromagnetics. He is the holder of two reflector antenna patents, two biomedical device patents, and three subsurface sensing device patents.

Dr. Rappaport is a member of Sigma Xi and Eta Kappa Nu professional honorary societies. He received the IEEE Antenna and Propagation Society's H. A. Wheeler Award for best applications paper, as a student, in 1986.

Oscar Rubiños-López received the M.S. and Ph.D. degrees in telecommunication engineering from the Universidad de Vigo, Vigo, Spain, in 1991 and 1997, respectively. He joined the Universidad de Vigo in 1991 and is currently an associate professor with the Dept. of Signal Theory and Communications at the Universidad de Vigo. During different periods of 2004, 2005 and 2007, he was a Visiting Researcher at Chalmers University of Technology in Goteborg (Sweden). His research interests include: the analysis and design of broadband antennas, numerical simulation of applied electromagnetic problems, terahertz technology for electromagnetic sensing applications, satellite systems and wireless communications. He has coauthored over 80 technical journal and conference papers. From 2001 to 2006, he held the position of Vice-President of University Extension (2001-2002) and for University Extension and Students at the University of Vigo.

Hipólito Gómez-Sousa received the M.S. degree in telecommunications engineering from the University of Vigo, Vigo, Spain, in 2009. Since 2009, he has been with the Department of Signal Theory and Communications, University of Vigo. His current research interests are on computational electromagnetism, THz sensing systems, and quantum cryptography.

A Gaussian Modulated Sinusoidal Pulse for Circuit-Parameter Estimation of a Synchronous Generator Using a 2D-FE Field Model

C. Hernandez [1], M. Cisneros-González [2], and M. A. Arjona[1]

[1] División de Estudios de Posgrado e Investigación
Instituto Tecnológico de la Laguna. Torreón, Coah. 27000 México.
coni.hernandez@ieee.org, marjona@ieee.org

[2] Departamento de Ciencias Básicas
Instituto Tecnológico del Valle del Guadiana. Durango, Dgo. 34371 México.
meritcisneros@gmail.com

Abstract ─ This paper presents the parameter estimation of a synchronous generator model based on the Gaussian Modulated Sinusoidal Pulse (GMSP). A 2D Finite Element (FE) model is used to evaluate the proposed signal in the estimation of the equivalent-circuit parameters of the generator. The presented methodology is based on the application of a FE model to simulate a standstill test. The FE model is validated against GMSP experimental results whilst the generator is at standstill. Afterwards, the FE simulation results are used to estimate the equivalent circuit parameters using a genetic algorithm. Finally, the estimated parameters are validated by comparing the simulation results against experimental data of a sudden three-phase short-circuit fault. A synchronous generator of a 7 kVA, 220V, 60 Hz, 1800 rpm, four-pole was employed for validating the estimated model parameters.

Index Terms - Finite element method, genetic algorithm, parameter estimation, synchronous generator.

I. INTRODUCTION

Equivalent electric circuits of electrical machines are a lumped representation of the complex electromagnetic behavior of these devices [1-3]. They have been used since several decades ago for predicting the performance of synchronous generators, induction motors and transformers. The equivalent circuits have advantages such as simplicity, fast computation and good accuracy in predicting the dynamic behavior of electric machines. On the other hand, lumped parameter models can be represented by state-space equations. The parameters of these generator models have usually been obtained by standstill and online tests [4]. The standstill tests are attractive because a small perturbation signal can be applied to each magnetic axis and a possible damage to the generator is avoided. The step voltage, dc-flux decay, and frequency response are standstill tests that have been commonly applied in estimating the complete set of parameters. Recently, new signals have been explored using the Finite Element Method (FEM) in induction machines [5]. A Finite Element (FE) model can be employed for evaluating any excitation signal at the design stage of an electrical machine. This approach is attractive for manufacturers in characterizing their synchronous generators before they are built [6-8]. Moreover, the FE method has also been used to study other types of electrical machines, e.g. switched reluctance generators and helical motion induction motors [9-10]. However, there are excitation signals which may be of interest in the parameter estimation of electrical machines such as the

Submitted On: Jan. 13, 2012
Accepted On: July 22, 2012

Gaussian Modulated Sinusoidal Pulse (GMSP). The GMSP has been successfully applied in the analysis of transient electromagnetic wave propagation but it has not been used in electrical machines [11].

This paper presents the standstill GMSP test for estimating the parameters of the *d*-*q*-axis model of a synchronous generator. The proposed methodology uses a 2D FE model which is validated against standstill GMSP experimental tests. Afterwards, the obtained FE data is used to estimate the model parameters by applying a Genetic Algorithm (GA) and they are fine tuned by employing the quasi-Newton method. To validate the estimated parameters, a sudden three-phase short-circuit fault is simulated and it is compared against experimental results where a good agreement was found. A 7 kVA, 220V, 1800 rpm and 60 Hz salient-pole synchronous generator is used in the proposed approach.

II. FINITE ELEMENT MODEL

The FEM has been used in many areas of knowledge where it is used to solve partial differential equations. In electrical engineering, the FEM has been used to solve the Maxwell equations that describe the electromagnetic dynamics of electrical machines. The 2D time-domain electromagnetic behavior of a synchronous machine is governed by the diffusion equation (1).

$$\frac{\partial}{\partial x}\left(\nu\frac{\partial A}{\partial x}\right)+\frac{\partial}{\partial y}\left(\nu\frac{\partial A}{\partial y}\right)+\sigma E-\sigma\frac{\partial A}{\partial t}=0\,, \quad (1)$$

where σ is the electric conductivity, E is the electric field intensity, A is the magnetic vector potential and ν is the magnetic reluctivity.

The FEM can be used to solve the diffusion equation (1) and this may be achieved by applying the Galerkin method. This method is based on the minimization of the residual by using a weighting function. Due that most electrical devices are fed by a voltage source, equation (1) needs to be modified to allow this source type instead injected currents. In this paper, the model formulation takes into account the electromagnetic field and circuit equations. The model formulation considers the winding currents as additional degrees of freedom and the related circuit equations are solved simultaneously with (1). The resulting FE formulation can be expressed by (2) and (3) [8].

$$\mathbf{SA}+\mathbf{N}\frac{\mathrm{d}\mathbf{A}}{\mathrm{dt}}-\mathbf{PI}=\mathbf{0}\,, \quad (2)$$

$$\mathbf{Q}\frac{\mathrm{d}\mathbf{A}}{\mathrm{dt}}+\mathbf{RI}+\mathbf{L}\frac{\mathrm{d}\mathbf{I}}{\mathrm{dt}}=\mathbf{V}\,, \quad (3)$$

where **S** is the stiffness matrix, **N** represents eddy current regions, **P** represents machine windings, and **Q** stands for induced voltages. Matrix **R** represents dc resistances, matrix **L** stands for end-winding inductances, vector **V** represents the source voltages, **I** represents a vector of winding currents, and **A** is the magnetic vector potential.

The matrices **S**, **N**, **P** and **Q** are obtained by assembling its corresponding elemental matrices which are defined by (4)-(7).

$$S_{kj}=\int_{S_i}\nabla\alpha_k^t\nu\nabla\alpha_j\,ds, \quad (4)$$

$$N_{kj}=\int_{S_i}\sigma\alpha_k^t\alpha_j\,ds, \quad (5)$$

$$P_{kj}=\int_{S_i}\frac{n_{cj}}{S_{fj}}\alpha_k\,ds, \quad (6)$$

$$Q_{kj}=\int_{S_i}\frac{n_{ck}\ell}{S_{fk}}\alpha_j\,ds, \quad (7)$$

where S_i indicates surface of the mesh element i, α is the shape function of first order finite elements and ds represents a differential surface. n_c represents the winding turns and S_f is the total surface of the coil. The axial length of the winding f is denoted by ℓ.

By using the Euler scheme, the time-domain dicretization of (2) and (3) can be expressed as (8).

$$\begin{bmatrix}\mathbf{S}(t+\Delta t)+\frac{1}{\Delta t}\mathbf{N} & -\mathbf{P}\\ \frac{1}{\Delta t}\mathbf{Q} & \mathbf{R}+\frac{1}{\Delta t}\mathbf{L}\end{bmatrix}\begin{bmatrix}\mathbf{A}(t+\Delta t)\\ \mathbf{I}(t+\Delta t)\end{bmatrix}=\begin{bmatrix}\frac{1}{\Delta t}\mathbf{N} & 0\\ \frac{1}{\Delta t}\mathbf{Q} & \frac{1}{\Delta t}\mathbf{L}\end{bmatrix}\begin{bmatrix}\mathbf{A}(t)\\ \mathbf{I}(t)\end{bmatrix}+\begin{bmatrix}0\\ \mathbf{V}\end{bmatrix}, \quad (8)$$

where Δt stands for the time step.

The GMSP voltage is applied to the stator with the field winding in short-circuit while the alternator is at standstill. This type of excitation has been applied to transient electromagnetic wave propagation and it is given by (9) [11]:

$$v(t) = V_m \exp\left(-\frac{(t - t_{delay})^2}{\beta}\right)\sin\left(\omega(t - t_{delay})\right), \quad (9)$$

where V_m is the amplitude of the signal, $\omega=2\pi f$ is the operational angular frequency, and t is time. The parameters β and t_{delay} define the signal shape. The studied synchronous generator has solid poles where eddy currents are induced. A constant permeability of 200 and a first order FE mesh was used [12]. The magnetic flux distributions along the *d*-*q* axis positions are shown in Figs. 1 and 2. The effect of the induced eddy currents in the flux distribution is clearly seen in the pole faces.

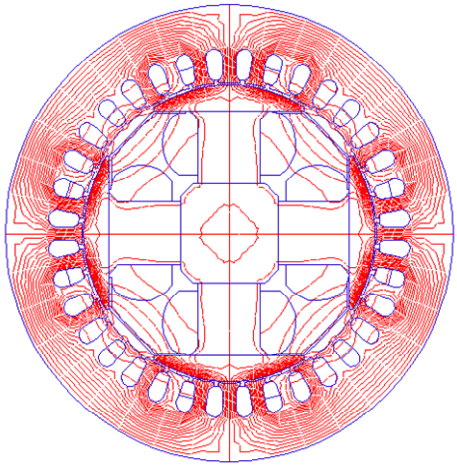

Fig. 1. D-axis field distribution with the GMSP standstill test.

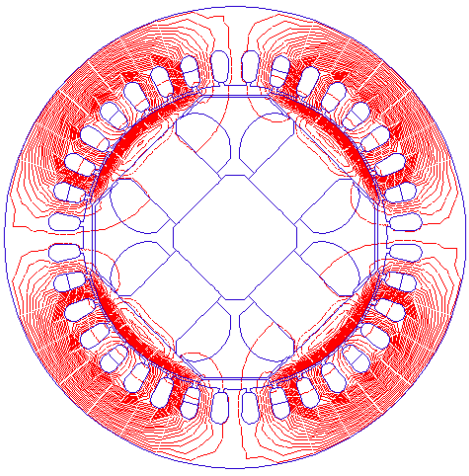

Fig. 2. Q-axis field distribution with the GMSP standstill test.

III. FE-GMSP MODEL VALIDATION

The second step in the proposed approach is the validation of the developed FE model. The GMSP was applied to the machine *d*-*q* magnetic axes, with the machine previously positioned in each magnetic axis at standstill. The GMSP test arrangement for the *d*-axis test is shown in Fig. 3. The signal generation and data acquisition were carried out by a computer and an acquisition card. A virtual instrument was developed in LabVIEW and allows the GMSP generation through a friendly user interface. A power amplifier was used to get the appropriate level of the testing current. The stator and field currents (i_a and i_f) were measured with resistive shunts. The GMSP voltage and the generator currents can be visualized in the computer during the test.

The GMSP voltage applied to the *d*-axis is shown in Fig. 4. A comparison of the FE predicted currents against experimental data for the *d*-axis, field and *q*-axis currents are shown in Figs. 5-7 where a good accuracy was achieved. The small values of field current causes a noisy signal as it is seen in Fig. 6.

The use of a FE model for parameter estimation offers the advantage of having noise free signals that allows estimating a better set of parameters. The employed GMSP signal uses a shape parameter (β) of 0.0311, a frequency of 60 Hz, and 0.5s for t_{delay}. The GMSP magnitude was adjusted to have approximately a stator current of 1 A in the *d*-*q* axis tests. A small difference is observed between the FE model and test results for the *q*-axis test (Fig. 7).

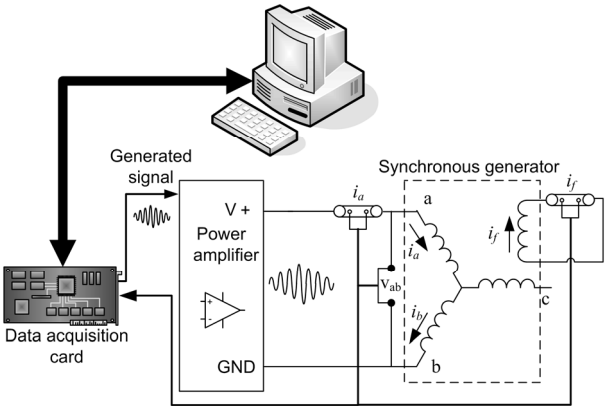

Fig. 3. Direct-axis standstill test with the GMSP excitation.

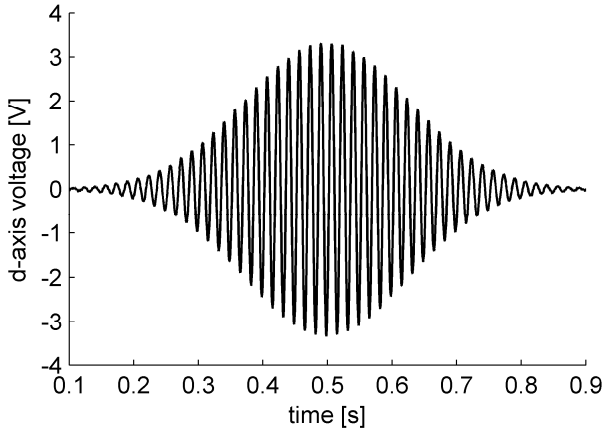

Fig. 4. GMSP voltage applied to the *d*-axis.

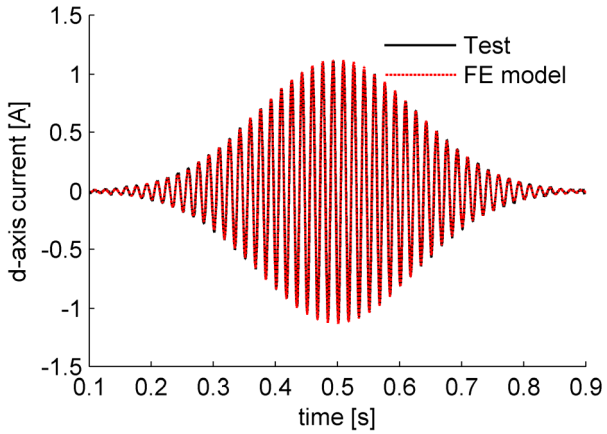

Fig. 5. FE model prediction and standstill test results for the *d*-axis current.

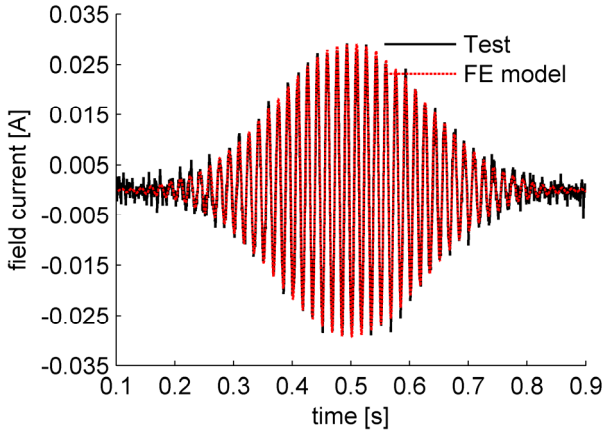

Fig. 6. FE model prediction and standstill test results for the field current.

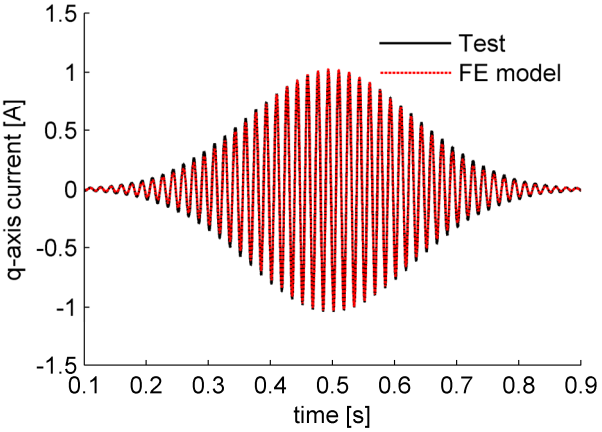

Fig. 7. FE model prediction and experimental results for the *q*-axis standstill test.

IV. PARAMETER ESTIMATION

The lumped model of the synchronous generator is represented with equivalent electric circuits and they are shown in Fig. 8. These circuit parameters need to be estimated and validated for its proper application in simulation studies. The machine voltage equations based on the two-axis theory are given by (10)-(14).

$$v_d = d\psi_d/dt + \omega\psi_q + r_a i_d, \tag{10}$$

$$v_f = d\psi_f/dt + r_f i_f, \tag{11}$$

$$0 = d\psi_{kd}/dt + r_{kd} i_{kd}, \tag{12}$$

$$v_q = d\psi_q/dt - \omega\psi_d + r_a i_q, \tag{13}$$

$$0 = d\psi_{kq}/dt + r_{kq} i_{kq}, \tag{14}$$

where v_d, v_f, v_q, i_d, i_f, and i_q are the *d*-axis, field, and *q*-axis voltages and currents respectively. ψ denotes flux linkages.

The set of state-equations can be derived using the equivalent circuits of the machine at standstill. A model structure with one damper winding and a differential leakage reactance (X_{kf}) was selected for the *d*-axis. The currents were chosen as state variables and the resulting equations for the *d*-axis model are given by (15).

$$\dot{\mathbf{I}}_d = \omega_0 \mathbf{X}_d^{-1} \mathbf{V}_d - \omega_0 \mathbf{X}_d^{-1} \mathbf{R}_d \mathbf{I}_d, \tag{15}$$

where I_d, R_d, V_d, and X_d are the *d*-axis current vector, resistance matrix, *d*-axis voltage vector, and *d*-axis reactance matrix, respectively. ω_0 is the rated angular speed.

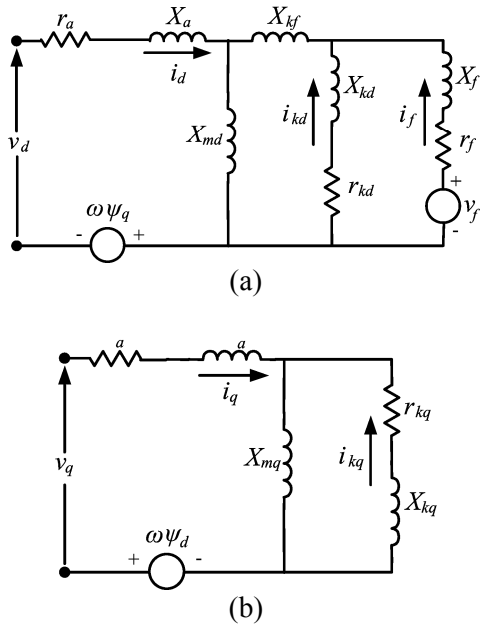

Fig. 8. Equivalent circuits. a) *d* -axis, b) *q*-axis.

In the *q*-axis model, one damper winding was considered and its state-space equations are given by (16).

$$\dot{\mathbf{I}}_q = \omega_0 \mathbf{X}_q^{-1} \mathbf{V}_q - \omega_0 \mathbf{X}_q^{-1} \mathbf{R}_q \mathbf{I}_q, \qquad (16)$$

where $\mathbf{I}_q$, $\mathbf{R}_q$, $\mathbf{V}_q$, and $\mathbf{X}_q$ stand for *q*-axis current vector, resistance matrix, voltage vector, and *q*-axis reactance matrix, respectively.

The equivalent-circuit parameter estimation was made using the least squares approach. The objective function can be expressed by (17) and it is minimized by a GA.

$$\min J(\theta) = \frac{1}{2}\sum_{i=1}^{N}(y_i - \hat{y}_i)^2, \qquad (17)$$

where $J(\theta)$ is the objective function, y_i is the set of experimental data, and $\hat{y}_i$ is the set of estimated responses from the proposed model. N is the number of the experimental points, and θ is the parameter vector to be determined.

The GA optimization is based on evolution of a population of individuals throughout generations. These individuals are randomly selected, recombined and mutated. A population of 5000 individuals represented with a 32-b floating point representation was used here. Each individual is composed by genes that represent the different variables of the search space. In this case, they correspond to the resistances and reactances of the equivalent circuits. The performance of each individual is evaluated by employing the cost function defined by (17). In the evaluation of the objective function, the fitness proportional selection, along with an elitist succession, were applied to produce offsprings. Crossover and mutation values of 0.9 and 0.001 were used, respectively [13]. The final model parameters were determined using the quasi-Newton algorithm [14] and the estimated set of parameters is shown in Table 1. The reactance X_{kf} has a negative value which means that the magnetic flux linkage between the field and *d*-axis damper windings is smaller than the magnetic flux linkage between stator and *d*-axis damper windings.

Table 1: Set of estimated parameters.

Parameter	**Value (pu)**
direct axis magnetizing reactance (X_{md})	1.43299600
armature leakage reactance (X_a)	0.12460000
field leakage reactance (X_f)	0.17413213
direct-axis damper leakage reactance (X_{kd})	0.02386047
direct-axis damper-field leakage reactance (X_{kf})	-0.10320315
direct-axis damper resistance (r_{kd})	0.30042507
quadrature axis magnetizing reactance (X_{mq})	0.98989783
quadrature-axis damper leakage reactance (X_{kq})	0.20369278
quadrature-axis damper resistance (r_{kq})	1.59745263
armature resistance (r_a)	0.08568540
field resistance (r_f)	0.01113500

The fitting of (15) for the *d*-axis test is shown in Figs. 9-10. The comparison of the *d*-axis current between the FE model and the *d*-axis equivalent circuit is illustrated in Fig. 9. The resulting fitting for the field current is shown in Fig. 10. Good estimation results were also obtained for the *q*-axis GMSP test. A previous research was carried out by the authors to estimate the synchronous machine parameters with the step voltage and the sine cardinal excitations [15-16]. Although these excitation signals are different, the results were similar to the ones obtained with the proposed GMSP test approach. However, the proposed methodology based on the usage of a FE model,

represents an advantage because it does not depend on the availability of high current power amplifiers. In addition, this approach can be applied at the design state of a large generator that allows having the model parameters of the machine before it is built.

V. LUMPED MODEL VALIDATION

The parameters were estimated using data from the GMSP-FE model simulations of the generator at standstill. However, these model parameters need to be validated. This was achieved by applying a sudden three-phase short-circuit fault to the synchronous generator. The fault was carried out at 70% of the rated terminal voltage. The generator was properly instrumented with current and voltage Hall effect sensors. The

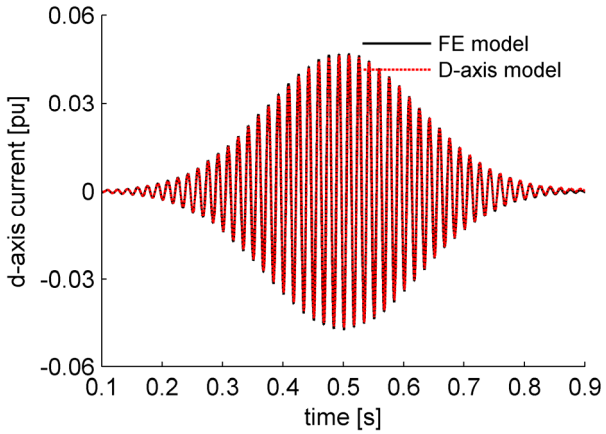

Fig. 9. FE and estimated lumped model results for the d-axis current at standstill.

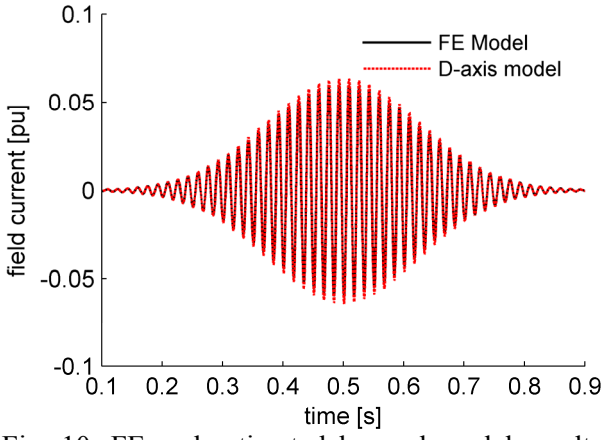

Fig. 10. FE and estimated lumped model results for the field current at standstill.

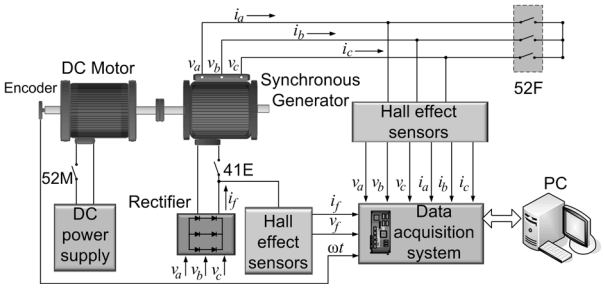

Fig. 11. Setup for the sudden short-circuit fault.

which has its own breaker (51M). An acquisition rotor position was measured with an encoder and the electrical operation was performed with the field winding breaker 41E, and a fault breaker 52F. The generator was driven with a dc motor system was used to collect all data as it is shown in Fig. 11. The 52F breaker was triggered at 0.3s causing the sudden short-circuit fault and the stator currents (i_{abc}), phase voltages (v_{abc}), rotor position, field voltage and field current were recorded.

The two-axis non-linear model of the synchronous generator can be represented by (18), and it can be derived from (10)-(14) [1].

$$\dot{\mathbf{x}} = \mathbf{A}\mathbf{x} + \mathbf{F}(\mathbf{x}) + \mathbf{B}\mathbf{z}, \qquad (18)$$

where **x** denotes the flux linkage state-variables, F is a function of nonlinear terms, **A** is the system matrix, **B** is the input vector and **z** is the input variable vector.

The comparison of the lumped model prediction against test results for the phase current in the short-circuit fault is shown in Fig. 12. It can be seen that the phase current is predicted with an accuracy of 6.5% at the first peak current swing. The field winding current is also predicted with an accuracy of 1.8% in the first current oscillation as it can be seen in Fig. 13. This demonstrates the validity of the estimated parameters. On the other hand, it was found that the peak stator current was predicted with the same accuracy as in [16] and the peak field current was reproduced more accurately than in [15]. However, in the second and third swings of the field current the three methods need improvement.

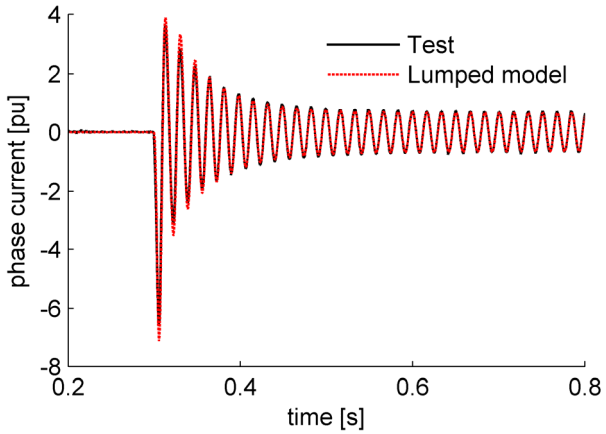

Fig. 12. Phase current in the sudden three-phase short-circuit test using the estimated set of parameters from the GMSP-FE model.

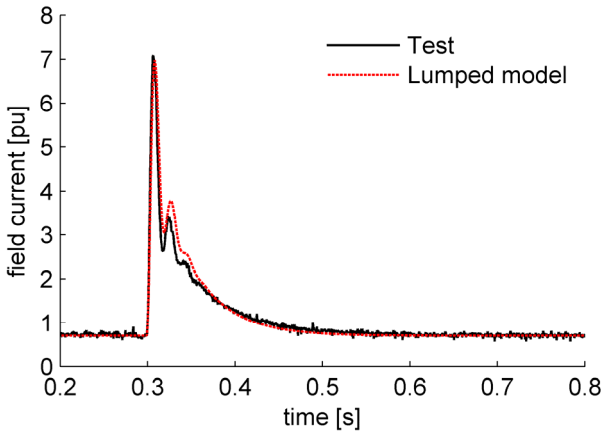

Fig. 13. Field current in the sudden three-phase short-circuit test using the estimated set of parameters from the GMSP-FE model.

VI. CONCLUSION

This paper has presented the parameter estimation of a synchronous generator model based on the use of a new excitation signal. The Gaussian Modulated Sinusoidal Pulse voltage was used to excite the generator at standstill. A FE model was developed and validated against standstill experiments and it was used to simulate the GMSP test. Afterwards, the FE simulation results were used to estimate the parameters of the *d-q* equivalent circuits of the synchronous generator. The Genetic and quasi-Newton algorithms were used to obtain the equivalent circuit parameters. Finally, the estimated parameters were employed in a non-linear lumped model to simulate the sudden three-phase short-circuit fault. The simulation results of the lumped model were compared against test data and a good agreement was achieved which demonstrates the validity of the proposed approach.

ACKNOWLEDGMENT

The authors would like to thank to CONACYT, PROMEP, and DGEST for their financial support to carry out this work.

REFERENCES

[1] B. Adkins and R.G. Harley. *The General Theory of Alternating Current Machines*. Chapman and Hall London, 1979.

[2] L. Qaseer, F. de León, S. Purushothaman, "Combined Field and Circuit Theories in Squirrel Cage Induction Motors Based on Micro-T Circuit Model," *The Applied Computational Electromagnetics Society (ACES) Journal*, vol. 26, no. 7, pp. 551-560, July 2011.

[3] J. Jin, W. Quan-di, Y. Ji-hui, and Z. Ya-li, "Wideband Equivalent Circuit Model and Parameter Computation of Automotive Ignition Coil based on Finite Element Analysis," *The Applied Computational Electromagnetics Society (ACES) Journal*, vol. 25, no. 7, pp. 612-619, July 2010.

[4] IEEE Std. 115-1995. *IEEE Guide: Test Procedures for Synchronous Machines*. 1995.

[5] A. K. Repo, P. Rasilo, A. Niemenmaa, and A. Arkkio, "Identification of Electromagnetic Torque Model for Induction Machines with Numerical Magnetic Field Solution," *IEEE Trans. on Magnetics*, vol. 44, no. 6, pp 1586-1589, June 2008.

[6] M. A. Arjona and D.C. MacDonald, "Characterising the d-axis Machine Model of a Turbogenerator using Finite Elements," *IEEE Trans. on Energy Conversion*, vol. 14, no. 3, pp. 340-346, Sept. 1999.

[7] M. A. Arjona, "Parameter Calculation of a Turbogenerador during an Open-Circuit Transient Excitation," *IEEE Trans. on Energy Conversion*, vol. 19, no. 1, pp. 46-52, March 2004.

[8] J. P. A. Bastos and N. Sadowski. *Electromagnetic Modeling by Finite Element Methods*, Marcel Dekker, Inc 2003.

[9] E. Afjei, H. Torkaman, "Finite Element Analysis of Switched Reluctance Generator under Fault Condition Oriented towards Diagnosis of Eccentricity Fault," *The Applied Computational Electromagnetics Society (ACES) Journal*, vol. 26, no. 1, pp. 8-16, January 2011.

[10] J. H. Alwash and L. J. Qaseer, "Three-Dimension Finite Element Analysis of a Helical Motion Induction Motor," *The Applied Computational Electromagnetics Society (ACES) Journal*, vol. 25, no. 8, pp. 703-712, August 2010.

[11] E. Başaran, H. A. Serim, S. Aksoy, "The Distortion Analysis of Pulse Propagation along a Rectangular Waveguide which is Partially Filled with a Dispersive Dielectric Film," *Fourth International Workshop on Electromagnetic Wave Scattering*, Gebze Institute of Technology, Kocaeli, Turkey. pp. 9-14, Sept. 2006.

[12] AREVA T&D, *SLIM Electromagnetic Software*, England, UK, 2008.

[13] D. E. Goldberg, *Genetic Algorithms in Search, Optimization and Machine Learning*, Addison-Wesley, 1989.

[14] S. S. Rao. *Engineering Optimization, Theory and Practice*, John Wiley & Sons, Inc, 1996.

[15] M. A. Arjona, C. Hernandez, M. Cisneros-Gonzalez, R. Escarela-Perez, "Estimation of Synchronous Generator Parameters using the Standstill Step-Voltage Test and a Hybrid Genetic Algorithm," *Electrical Power and Energy Systems*, vol. 35, pp. 105-111, 2012.

[16] M. A Arjona, C. Hernandez, M. Cisneros-Gonzalez, "Parameter Estimation of a Synchronous Generator using a Sine Cardinal Perturbation and Mixed Stochastic-Deterministic Algorithms," *IEEE Trans. on Industrial Electronics*, vol. 58, no. 2, pp. 486-493, February 2011.

C. Hernandez received the B.Sc. degree in computer science from the Instituto Tecnológico de Estudios Superiores de Monterrey, Monterrey, México, in 1990, the M.Sc. degree in foundations of advanced information technology from Imperial College, London, U.K., in 1995, and the Sc.D. degree in electrical engineering from the Instituto Tecnológico de la Laguna, Torreón, México, in 2007.

She was with the Simulation Department, Instituto de Investigaciones Eléctricas from 1991 to 2000. She is currently with the Instituto Tecnológico de la Laguna, Torreón, México. Her interests are in artificial intelligence and global optimization algorithms applied to electrical machines.

M. Cisneros-González received the B.Sc. and M.Sc. degrees in electronic engineering from the Instituto Tecnológico de Durango, Durango, México, in 2002 and 2005, respectively, and the Sc. D. degree in electrical engineering from Instituto Tecnológico de la Laguna in 2010. She is currently working with the Instituto Tecnológico del Valle del Guadiana, Durango, México. Her research interests include parameter estimation of electrical machines and electromagnetics.

M. A. Arjona received the B.Sc. degree in electrical engineering from the Instituto Tecnológico de Durango, Durango, México, in 1988, the M.Sc. degree in electrical engineering from the Instituto Tecnológico de la Laguna, Torreón, México, in 1990, and the Ph.D. degree in electrical engineering from Imperial College, London, U.K., in 1996.

He was with the Simulation Department, Instituto de Investigaciones Eléctricas from 1991 to 1999. He is currently a Professor of electrical machines with the Instituto Tecnológico de la Laguna. His research interests are in the electromagnetic design, analysis, and control of electrical machines.

2-D DOA Estimation with Matrix Pencil Method in the Presence of Mutual Coupling

A. Azarbar [1], G. R. Dadashzadeh [2], and H. R. Bakhshi[2]

[1] Department of Computer and Information Technology Engineering,
Islamic Azad University, Parand Branch,Tehran, 37613 96361, Iran
aliazarbar@piau.ac.ir

[2]Faculty of Engineering, Shahed University, Tehran 33191 18651, Iran
gdadashzadeh@shahed.ac.ir, bakhshi@shahed.ac.ir

Abstract ─ A new 2-D Direction of Arrival (DOA) estimation algorithm in the presence of mutual coupling for the Uniform Rectangular Array (URA) based on Matrix Pencil (MP) method is presented. By setting a group of elements as auxiliary on each side of the URA, it can accurately estimate the DOAs using a single snapshot of data and the effect of mutual coupling can be eliminated by the inherent mechanism of the proposed method. Theoretical analysis and simulation results demonstrated the effectiveness of the proposed algorithm.

Index Terms ─ 2-D DOA estimation, Matrix pencil, Mutual coupling, URA..

I. INTRODUCTION

The study of adaptive antennas in radar and wireless communications has been an attractive research topic for several decades. Furthermore, direction of arrival estimation is an important feature of adaptive antenna arrays. MUltiple SIgnal Classification (MUSIC), Estimation of Signal Parameters via Rotational Invariance Techniques (ESPRIT) [1] and MP [2-5] are some popular conventional methods of DOA estimation.

In array signal processing, most adaptive algorithms assume that the array elements are isotropic sensors; thus the mutual coupling effects are ignored. However, in practical applications, each array element receives signals reradiated from other sensors within the array and the performance of an adaptive antenna array is drastically affected by the existence of the mutual coupling effect between antenna elements [6-8]. Such an effect needs to be removed in order to achieve a high performance in an actual system [8]. Many efforts have been made to reduce or compensate for this effect on Uniform Linear Array (ULA) and Uniform Circular Array (UCA) [8-14]. But few authors have dealt with 2-D cases and considered the effect of mutual coupling or any other array errors [15-16].

Some studies have stated that using auxiliary elements can reduce the effect of mutual coupling [16–17]. It was shown in [14] and [16], that by providing a modest number of auxiliary array elements, the MUSIC algorithm can be adopted directly for DOA estimation in ULA and URA and the approach is resilient against a well-known mutual coupling model with some unknown parameters. But, these proposed algorithms suffer from two major drawbacks: first, the MUSIC algorithm is based on the covariance matrix and it requires independent identically-distributed secondary data to estimate the covariance matrix; also the estimation of the covariance matrix requires the storage and processing of the secondary data. This is computationally intensive, requiring many calculations in real time. The second is that in the proposed algorithm there may be some blind angles caused by some particular combinations of mutual coupling coefficients which should be avoided while designing the array [14].

Submitted On: Oct. 13, 2010
Accepted On: Nov. 4, 2011

In this paper, a simple solution is presented to settle the coupling problem of URA in 2-D DOA estimation based on the MP algorithm. This algorithm can overcome the drawbacks of statistical techniques. Because it is based on the spatial samples of the data and the analysis is done on a snapshot-by-snapshot basis, non-stationary environments can be handled easily [2]. It is proposed that the array elements on the boundary of URA should be of auxiliary elements and only use the output of the rest array to estimate the DOA of incoming signals. Through this process, the MP algorithm can be directly applied for 2-D DOA estimation.

II. 2-D MATRIX PENCIL METHOD

The DOA estimation of several signals which simultaneously impinge on a two-dimensional planar array can also be performed using the Matrix Pencil method. Consider a URA consisting of $M\times N$ equally spaced elements in rows and columns. The space between neighboring columns is d_x and that of neighboring rows is d_y. The array receives P narrow band signals, $s_p(t)$, from unknown directions, $(\theta_p,\ \varphi_p)$, p=1, 2,..., P, as shown in Fig. 1.

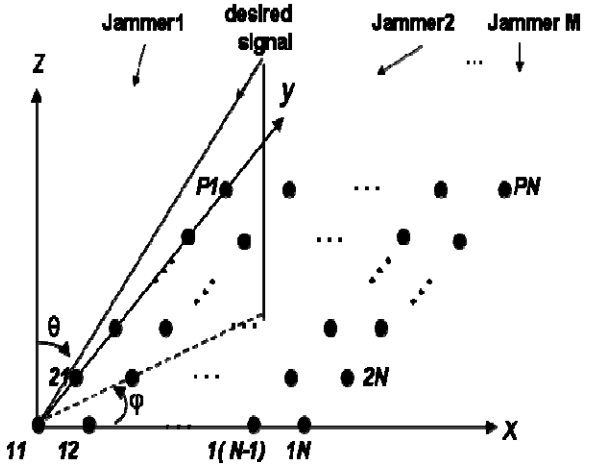

Fig. 1. URA with $M\times N$ elements.

Hence, the voltage $x(m, n)$ induced at the feed point of the antenna elements of the URA which can be modeled by summing the complex exponentials, i.e.,

$$y(m,n) = x(m,n) + n(m,n).$$
$$m = 1,...,\ M\ ,n = 1,...,\ N. \tag{1}$$

where

$$x(m,n) = \sum_{p=1}^{P} r_p\, y_p^m\, z_p^n,$$

$$y_p = \exp(j\frac{2\pi}{\lambda} d_y \sin\theta_p \sin\varphi_p), \tag{2}$$

$$z_p = \exp(j\frac{2\pi}{\lambda} d_x \sin\theta_p \cos\varphi_p).$$

where r_p is the complex amplitude of pth signal and $n(m,n)$ is the additive noise,

Basically, in 2-D MP method, 2-D problem is divided into two 1-D problems. Solved for each pole in each dimension and paired together to get the correct DOA angles. The formulation of the 2-D matrix pencil method was discussed in detail in [4]. The noiseless data matrix $x(m,n)$ can be written as follows:

$$\mathbf{X} = \begin{bmatrix} \mathbf{X_1} \\ \mathbf{X_2} \\ \vdots \\ \mathbf{X_M} \end{bmatrix} = \begin{bmatrix} x(1,1) & x(1,2) & \dots & x(1,N) \\ x(2,1) & x(2,2) & \dots & x(2,N) \\ \vdots & \vdots & \ddots & \vdots \\ x(M,1) & x(M,2) & \dots & x(M,N) \end{bmatrix}. \tag{3}$$

The data matrix $\mathbf{X}$ can be enhanced and written in Hankel block matrix structure as follows:

$$\mathbf{D} = \begin{bmatrix} \mathbf{X_1} & \mathbf{X_2} & \mathbf{X_3} \\ \mathbf{X_2} & \mathbf{X_3} & \mathbf{X_4} \\ \vdots & \vdots & \vdots \\ \mathbf{X_{M-2}} & \mathbf{X_{M-1}} & \mathbf{X_M} \end{bmatrix}. \tag{4}$$

Two matrices of $\mathbf{D_1}$ and $\mathbf{D_2}$ are defined in order to extract the poles associated with the one dimension. $\mathbf{D_1}$ is obtained from $\mathbf{X}$ by deleting the last row and $\mathbf{D_2}$ is obtained from $\mathbf{X}$ by deleting the first row. One can also write

$$\mathbf{D_2} = \mathbf{Y_1 R Y_0 Y_2}, \tag{5}$$

$$\mathbf{D_1} = \mathbf{Y_1 R Y_2}. \tag{6}$$

where

$$\mathbf{Y_2} = \begin{bmatrix} 1 & z_1 & \dots & z_1^{N-1} & y_1 & y_1z_1 & \dots & y_1z_1^{N-1} & \dots & y_1^2 & y_1^2z_1 & \dots & y_1^2z_1^{N-1} \\ 1 & z_2 & \dots & z_2^{N-1} & y_2 & y_2z_2 & \dots & y_2z_2^{N-1} & \dots & y_2^2 & y_2^2z_2 & \dots & y_2^2z_2^{N-1} \\ \vdots & \vdots & & \vdots & & & & & & & & & \\ 1 & z_P & \dots & z_P^{N-1} & y_P & y_Pz_P & \dots & y_Pz_P^{N-1} & \dots & y_P^2 & y_P^2z_P & \dots & y_P^2z_P^{N-1} \end{bmatrix}_{P\times(3N)}. \tag{7}$$

$$\mathbf{Y_1}=\begin{bmatrix} 1 & 1 & \dots & 1 \\ y_1 & y_2 & \dots & y_P \\ \vdots & \vdots & & \vdots \\ y_1^{M-2} & y_2^{M-2} & \dots & y_P^{M-2} \end{bmatrix}_{(M-1)\times P}, \quad (8)$$

$$\mathbf{Y_0} = diag[y_1, y_2, ..., y_P], \quad (9)$$

$$\mathbf{R} = diag[r_1, r_2, ..., r_P]. \quad (10)$$

where diag [•] represents a $P \times P$ diagonal matrix. Now, consider the matrix pencil

$$\mathbf{D_2} - \lambda \mathbf{D_1} = \mathbf{Y_1 R}\{\mathbf{Y_0} - \lambda \mathbf{I}\}\mathbf{Y_2}. \quad (11)$$

while **I** is the $P \times P$ identity matrix. It was shown in [3] that this problem can be reduced to an ordinary eigenvalue problem such that $\mathbf{Y_0} = diag[y_1, y_2, ..., y_P]$ is the eigenvalues of:

$$\mathbf{D_1^+ D_2} - \lambda \mathbf{I}. \quad (12)$$

where $\mathbf{D_1}^+$ is the Moore-Penrose pseudo-inverse of $\mathbf{D_1}$. This, in turn, is defined as:

$$\mathbf{D_1^+} = (\mathbf{D_1^H D_1})^{-1} \mathbf{D_1^H} \quad (13)$$

Similarly, the data $x(m;n)$ can be written in a new matrix form as follows:

$$\mathbf{X'} = \begin{bmatrix} \mathbf{X'_1} \\ \mathbf{X'_2} \\ \vdots \\ \mathbf{X'_N} \end{bmatrix} = \begin{bmatrix} x(1,1) & x(2,1) & \dots & x(M,1) \\ x(1,2) & x(2,2) & \dots & x(M,2) \\ \vdots & \vdots & \ddots & \vdots \\ x(1,N) & x(2,N) & \dots & x(M,N) \end{bmatrix}. \quad (14)$$

The data matrix **X'** can be enhanced and written in Hankel block matrix structure as follow:

$$\mathbf{D'} = \begin{bmatrix} \mathbf{X'_1} & \mathbf{X'_2} & \mathbf{X'_3} \\ \mathbf{X'_2} & \mathbf{X'_3} & \mathbf{X'_4} \\ \vdots & \vdots & \vdots \\ \mathbf{X'_{N-2}} & \mathbf{X'_{N-1}} & \mathbf{X'_N} \end{bmatrix}. \quad (15)$$

So, $\mathbf{Z_0} = diag[z_1, z_2, ..., z_P]$ will be the eigenvalues of:

$$\mathbf{D'^+_1 D'_2} - \lambda \mathbf{I}. \quad (16)$$

where $\mathbf{D'_1}$ is obtained from **D'** by deleting the last row and $\mathbf{D'_2}$ is obtained from **D'** by deleting the first row.

In the presence of noise, some pre-filtering needs to be done. Noise reduction can be performed via the Singular Value Decomposition (SVD) [18]. **D** and **D'** are decomposed using the SVD yielding:

$$\mathbf{D} = \mathbf{U}_s \ \mathbf{\Sigma}_s \ \mathbf{V_s^H} + \mathbf{U}_n \ \mathbf{\Sigma}_n \ \mathbf{V_n^H}. \quad (17)$$

where $(\bullet)^H$ denotes conjugate transpose and the $\mathbf{U_s}$, $\mathbf{\Sigma_s}$ and $\mathbf{V_s^H}$ are in the signal subspace corresponding to the P principal components whereas $\mathbf{U_n}$, $\mathbf{\Sigma_n}$ and $\mathbf{V_n^H}$ are in the noise subspace.

. It was shown in [3] that, for the noisy case, the eigenvalues of the following matrix was the solution for determining y_p:

$$\mathbf{U_{s1}^+ \ U_{s2}} - \lambda \mathbf{I}. \quad (18)$$

where $\mathbf{U_{s1}}$ is obtained from $\mathbf{U_s}$ with its the last row of $\mathbf{U_s}$ deleted and $\mathbf{U_{s2}}$ is obtained by deleting the first row of $\mathbf{U_s}$. Second, **D'** was decomposed using the SVD yielding:

$$\mathbf{D'} = \mathbf{U'}_s \ \mathbf{\Sigma'}_s \ \mathbf{V'_s^H} + \mathbf{U'}_n \ \mathbf{\Sigma'}_n \ \mathbf{V'_n^H}. \quad (19)$$

Similarly, the eigenvalues of the following matrix is the solution for determining z_p:

$$\mathbf{U'^+_{s1} \ U'_{s2}} - \lambda \mathbf{I}. \quad (20)$$

III. THE PROPOSED ALGORITHM

Most DOA estimation algorithms, including MP assume an ideal, linear array of isotropic sensors. Unfortunately, such an ideal sensor is obviously not realizable. A practical antenna array is composed of the elements in some physical sizes. The elements sample and reradiate incident fields and cause mutual coupling. Mutual coupling severely degrades the accuracy of the DOA estimator [8]. Any implementation of DOA estimation requires a compensation for the mutual coupling.

In this paper, in order to nullify the effect of mutual coupling, the array sensors on the boundary of URA are set to be auxiliary sensors and only the output of the rest array are used to estimate the DOAs. Utilizing this process, the MP algorithm can be directly applied for 2-D DOA estimation.

Assuming that **C** denotes the mutual coupling matrix of the URA, the array's output can be expressed as $\mathbf{x_c} = \mathbf{C x}_c$ where $\mathbf{x_c}$ denotes the received signal vector in the presence of mutual coupling and is defined as $\mathbf{x_c}$=[$x_c(1,1)$, $x_c(1,2)$,..., $x_c(1,N)$, $x_c(2,1)$, ..., $x_c(2,N)$, …,$x_c(M,1)$,...,$x_c(M,N)$]

According to [19], the coupling between neighboring elements of a ULA is almost the same and the magnitude of the coupling parameters decreases very fast by increasing the sensor

spacing. Essentially, the mutual coupling coefficient between two far-apart elements can be approximated to zero. Thus, it is often sufficient to consider the ULA coupling model with only finite non-zero coefficients, and a banded symmetric toeplitz matrix can be used as a model for the mutual coupling. This model can be extended to the mutual coupling of URA. Because the mutual coupling of the URA is more complex than the ULA and UCA, in this paper we assume that one sensor is only affected by the coupling of the 8 sensors around it [16], which is shown in Fig. 2.

The mutual coupling matrix can be expressed as:

$$\mathbf{C}=\begin{bmatrix} \mathbf{C}_1 & \mathbf{C}_2 & 0 & \cdots & 0 & 0 & 0 \\ \mathbf{C}_2 & \mathbf{C}_1 & \mathbf{C}_2 & \cdots & 0 & 0 & 0 \\ \vdots & \ddots & & \ddots & & \vdots & \\ 0 & 0 & 0 & \cdots & \mathbf{C}_2 & \mathbf{C}_1 & \mathbf{C}_2 \\ 0 & 0 & 0 & \cdots & 0 & \mathbf{C}_2 & \mathbf{C}_1 \end{bmatrix}_{MN\times MN}. \quad (21)$$

where $\mathbf{C}_1$ and $\mathbf{C}_2$ are $N\times N$ sub-matrices of $\mathbf{C}$ and can be given by:

$$\begin{aligned} \mathbf{C}_1 &= toeplitz\{[1, c_x, 0, ..., 0]\}, \\ \mathbf{C}_2 &= toeplitz\{[c_y, c_{xy}, 0, ..., 0]\}. \end{aligned} \quad (22)$$

where the symbol $toeplitz\{\mathbf{v}\}$ denotes the symmetric toeplitz matrix constructed by the vector $\mathbf{v}$. In order to eliminate the effect of the mutual coupling, the sensors on the boundary of the URA are set to be auxiliary sensors.

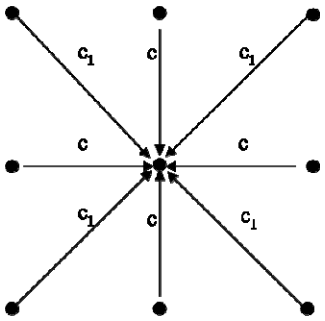

Fig. 2. Scheme of mutual coupling.

Now, a new matrix $\mathbf{D}_c$ can be formed, which is obtained from the output of the middle $(M\text{-}2)\times N$ in URA:

$$\mathbf{D}_c=\begin{bmatrix} \mathbf{X}_{c2} \\ \mathbf{X}_{c3} \\ \vdots \\ \mathbf{X}_{c(M-1)} \end{bmatrix}=\begin{bmatrix} x(2,1) & x(2,2) & \dots & x(2,N) \\ x(3,1) & x(3,2) & \dots & x(3,N) \\ \vdots & \vdots & \ddots & \vdots \\ x(M-1,1) & x(M-1,2) & \dots & x(M-1,N) \end{bmatrix}. \quad (23)$$

Let us define:

$$\overline{\mathbf{C}}=\begin{bmatrix} \mathbf{C}_2 \\ \mathbf{C}_1 \\ \mathbf{C}_2 \end{bmatrix}_{(3N)\times N}. \quad (24)$$

After this definition, a very important relationship between $\mathbf{D}$ and $\mathbf{D}_c$ is obtained as follows:

$$\mathbf{D}_c = \mathbf{D}\,\overline{\mathbf{C}}. \quad (25)$$

So, two matrices of $\mathbf{D}_{c1}$ and $\mathbf{D}_{c2}$ are defined. $\mathbf{D}_{c1}$ is obtained from $\mathbf{D}_c$ by deleting the last row and $\mathbf{D}_{c2}$ is obtained from $\mathbf{D}_c$ by deleting the first row. Therefore:

$$\begin{aligned} \mathbf{D}_{c1} &= \mathbf{D}_1\overline{\mathbf{C}}\ , \\ \mathbf{D}_{c2} &= \mathbf{D}_2\overline{\mathbf{C}}\ . \end{aligned} \quad (26)$$

Using (5) and (6), the following can be obtained:

$$\begin{aligned} \mathbf{D}_{c2} &= \mathbf{Y}_1\mathbf{R}\mathbf{Y}_0\mathbf{Y}_2\overline{\mathbf{C}}, \\ \mathbf{D}_{c1} &= \mathbf{Y}_1\mathbf{R}\mathbf{Y}_2\overline{\mathbf{C}}. \end{aligned} \quad (27)$$

Now, the matrix pencil can be formed:

$$\mathbf{D}_{c2} - \lambda\mathbf{D}_{c1} = \mathbf{Y}_1\mathbf{R}\{\mathbf{Y}_0 - \lambda\mathbf{I}\}\mathbf{Y}_2\overline{\mathbf{C}}. \quad (28)$$

This problem can be reduced to an ordinary eigenvalue problem and $\mathbf{Y}_0 = diag[y_1, y_2, ..., y_P]$ will be the eigenvalues of:

$$\mathbf{D}_{c1}^{+}\mathbf{D}_{c2} - \lambda\mathbf{I}. \quad (29)$$

Similar to $\mathbf{D}_c$, a new matrix $\mathbf{D'}_c$ can be formed, which is obtained from the output of the middle $M\times(N\text{-}2)$ in the URA:

$$\mathbf{D}'_c=\begin{bmatrix} \mathbf{X}'_{c2} \\ \mathbf{X}'_{c3} \\ \vdots \\ \mathbf{X}'_{c(N-1)} \end{bmatrix}=\begin{bmatrix} x(1,2) & x(2,2) & \dots & x(M,2) \\ x(1,3) & x(2,3) & \dots & x(M,3) \\ \vdots & \vdots & \ddots & \vdots \\ x(1,N-1) & x(2,N-1) & \dots & x(M,N-1) \end{bmatrix}. \quad (30)$$

So, $\mathbf{Z}_0 = diag[z_1, z_2, ..., z_P]$ will be the eigenvalues of:

$$\mathbf{D}'^{+}_{c1}\mathbf{D}'_{c2} - \lambda\mathbf{I}. \quad (31)$$

where $\mathbf{D'}_{c1}$ is obtained from $\mathbf{D'}_c$ by deleting the last row and $\mathbf{D'}_{c2}$ is obtained from $\mathbf{D'}_c$ by deleting the first row.

For the noisy case, the eigen-structure of the matrices $\mathbf{D}_c$ and $\mathbf{D'}_c$ is found by considering the SVD:

$$\mathbf{D}_c = \mathbf{U}_c\ \ \mathbf{\Sigma}_c\ \ \mathbf{V}_c^{H} \quad (32)$$

Here, $\mathbf{U}_c$ and $\mathbf{V}_c$ are unitary matrices, composed of the eigenvectors of $\mathbf{D}_c\mathbf{D}_c^{H}$ and,

$\mathbf{D_c}^H\mathbf{D_c}$, respectively. $\mathbf{\Sigma_c}$ is the singular values of $\mathbf{D_c}$. For simplicity, it is assumed that the number of signals is known in this paper. After SVD of data matrix $\mathbf{D_c}$ is computed, the matrix space is divided into two subspaces, signal subspace and noise subspace. Here, the matrices $\mathbf{D_{c1}}$ and $\mathbf{D_{c2}}$ are constructed from the signal subspace matrix. So, the "filtered" matrix $\mathbf{U_{cs}}$ is constructed. It consists of the first P columns of $\mathbf{U_c}$ and the rest of right-singular vectors, corresponding to the small singular values, are discarded. Therefore, the following can be written:

$$\begin{aligned}\mathbf{D}_{c1} &= \mathbf{U}_{cs1}\ \ \mathbf{\Sigma}_{cs}\ \ \mathbf{V}_{cs}^{\ H},\\ \mathbf{D}_{c2} &= \mathbf{U}_{cs2}\ \ \mathbf{\Sigma}_{cs}\ \ \mathbf{V}_{cs}^{\ H}.\end{aligned} \tag{33}$$

where $\mathbf{U_{cs1}}$ is obtained from $\mathbf{U_{cs}}$ with its the last row of $\mathbf{U_{cs}}$ deleted and $\mathbf{U_{cs2}}$ is obtained by deleting the first row of $\mathbf{U_{cs}}$. Then, the eigenvalues of the following matrix is the solution for determining y_p:

$$\mathbf{U}_{cs1}^{+}\ \mathbf{U}_{cs2}\ -\lambda\mathbf{I} \tag{34}$$

Similarly, $\mathbf{D'_c}$ was decomposed using the SVD yielding:

$$\mathbf{D}'_{\mathbf{c}} = \mathbf{U}'_{cs}\ \ \mathbf{\Sigma}'_{cs}\ \ \mathbf{V}'^{\,H}_{cs} + \mathbf{U}'_{cn}\ \ \mathbf{\Sigma}'_{cn}\ \ \mathbf{V}'^{\,H}_{cn}. \tag{35}$$

where $\mathbf{U_{cs1}}$ and $\mathbf{U_{cs2}}$ are obtained by deleting the last row and the first row of $\mathbf{U_{cs}}$, respectively.

Then, the eigenvalues of the following matrix is the solution for determining z_p:

$$\mathbf{U}'^{+}_{cs1}\ \mathbf{U}'_{cs2}\ -\lambda\mathbf{I}. \tag{36}$$

Most of adaptive algorithms which compensate mutual coupling, must be computed the inverse coupling matrix. That is computationally intensive and requires many calculations in the real time. The proposed algorithm can be directly applied for 2-D DOA estimation and don't use the inverse mutual coupling matrix. In addition, the data matrices of the proposed algorithm ($\mathbf{D_c}$ and $\mathbf{D'_c}$) are as order of N×(M-2). But, the data matrices of the MP algorithm ($\mathbf{D}$ and $\mathbf{D'}$) are as order of 3N×(M-2). Hence, the proposed algorithm is faster than the MP algorithm.

IV. NUMERICAL SIMULATIONS

In this section, 5×5 elements z-direction parallel identical dipoles are used, which are equally spaced in rows and columns with the distance of λ/2, where λ is the wavelength. Each dipole is 0.5λ long and λ/200 in radius and all the elements are loaded with a terminal load of Z_L = 50 Ω. The Method of Moments (MOM) is used to accurately model the interactions between antenna elements. The array receives two signals from (20˚, 15˚) and (35˚, 60˚). The MP algorithm and the proposed algorithm use only a single snapshot. Table.1 shows the accuracy of DOA estimation using the new proposed algorithm in the presence of MC.

Table 1: Comparing Accuracy of MP and Proposed Algorithm

	The MP method in the presence of MC	The proposed algorithm in the presence of MC
Signal 1	(19.89˚,13.82˚)	(20.00˚,15.00˚)
Signal 2	(32.64˚,57.87˚)	(35.00˚,60.00˚)

In the next example, the noisy data are used. The Signal-to-Noise Ratio (SNR) was set at 20 dB. 1000 independent trials are used. The scatter plot of the estimated elevation and azimuth angles with conventional MP algorithm and the proposed algorithm in the presence of the mutual coupling are shown in Figs. 3 and 4.

As can be seen, using the proposed algorithm, the error of bias is very low and accuracy is high and very close to ideal.

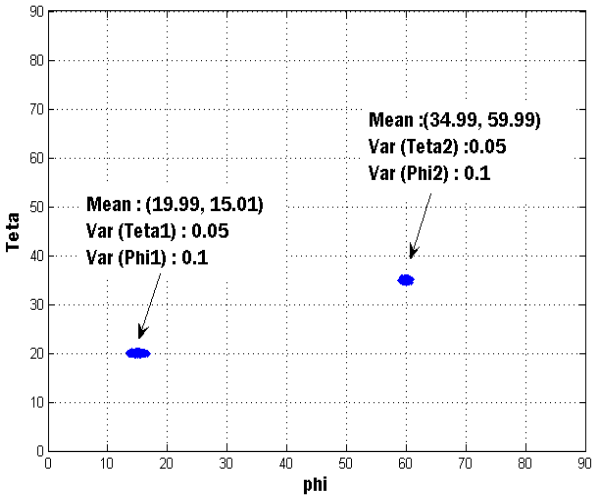

Fig. 3. The scatter plot of direction of arrival angles of 2 impinging signals in the absence of MC.

The performance of the proposed method is compared with ideal MP algorithm, under different SNR. The variances of the estimators are plotted in Fig. 5. As can be seen from Fig. 5, the

proposed algorithm in the presence of mutual coupling has a close variance to the ideal MP method.

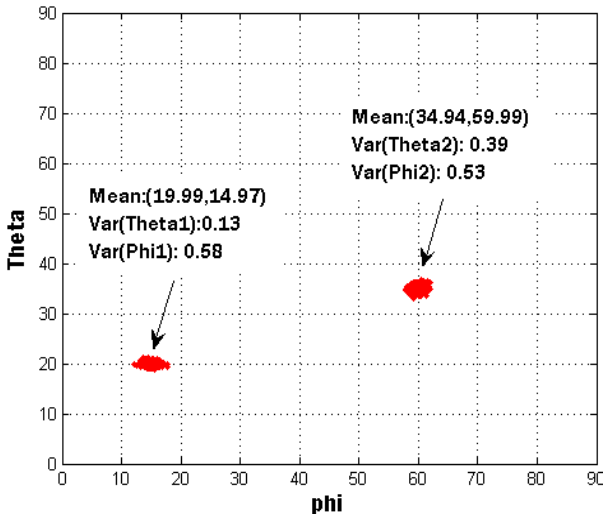

Fig. 4. The scatter plot of direction of arrival angles of 2 impinging signals with the proposed algorithm in the presence of MC.

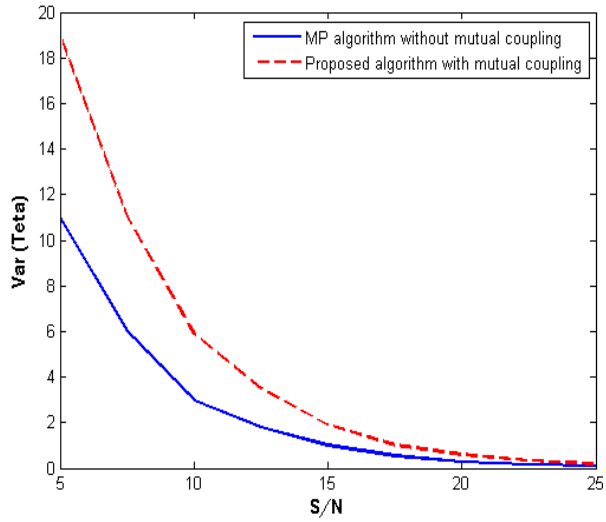

Fig. 5. Comparing of the performance of MP and the proposed algorithm for different SNR.

V. CONCLUSION

In this paper, the problem of 2-DDOA estimation was studied for the URA in the presence of mutual coupling. By setting the sensors on the boundary of the URA as auxiliary sensors, the robustness of the proposed algorithm was proved to be against sensor coupling. Without using the mutual coupling coefficient calculation, this method can accurately estimate the 2-D DOAs only by using one snapshot of data.

REFERENCES

[1] J. C. Jr. Liberti, and T. S. Rappaport, "*Smart Antennas for Wireless Communications*,": IS-95 and Third Generation CDMA Applications. Englewood Cliffs, Prentice Hall, pp. 123-135, 1993.

[2] Y. Hua, and T. K. Sarkar, "Matrix Pencil Method for Estimation Parameters of Exponentially Damped/Undamped Sinusoids in Noise," *IEEE Trans. Acoust. Speech and Signal Processing*, vol. 38, pp. 814-24, 1990.

[3] T. K. Sarkar, and O. Pereira, "Using the Matrix Pencil Method to Estimate the Parameters of a Sum of Complex Exponentials," *IEEE Antennas and Propagation Magazine*, vol. 37, no. 1, pp. 48-55, February 1995.

[4] Y. Hua, Estimating Two-Dimensional Frequencies by Matrix Enhancement and Matrix Pencil, *IEEE Trans. Signal Process*, vol. 40, no. 9, pp. 2267-2280, 1992.

[5] N. Yilmazer, S. Ari and T. K. Sarkar, "Multiple Snapshot Direct Data Domain Approach and ESPRIT Method for Direction of Arrival Estimation," *Digital Signal Processing,* vol. 18, pp.561-567, 2008.

[6] K. R. Dandekar, H. Ling and G. Xu,: 'Effect of Mutual Coupling on Direction Finding in Smart Antenna Applications', *Electron. Lett.*, 36, pp. 1889-1891, 2000.

[7] P. N. Fletcher, A. E. Wicks, and M. Dean: 'Improvement of Coupling Corrected Difference Beams in Small Phased Arrays', *Electron. Lett.*, vol. 33, no. 5, pp. 352-353, 1997.

[8] I. J. Gupta and A. A. Ksienski "Effect of Mutual Coupling on the Performance of Adaptive Array," *IEEE Trans. Ant. Propagat.,* vol. 31, pp. 785-91, Sep. 1983.

[9] H. T. Hui "Compensating for the Mutual Coupling Effect in Direction Finding based on a New Calculation Method for Mutual Impedance," *IEEE Antenna and wireless Propagation Letters*. vol. 2, pp. 26-29, 2003.

[10] E. Lau, R. Adve and T. K. Sarkar, "Minimum Norm Mutual Coupling Compensation with Applications in Direction of Arrival Estimation". *IEEE Trans. Antennas Propag.,* vol. 52, no. 8, pp.2034-2041, Aug. 2004.

[11] M. Lin, and L. Yang "Blind Calibration and DOA Estimation with Uniform Circular Arrays in the Presence of Mutual Coupling," *IEEE Antenna and wireless Propagation Letters.* vol. 5, pp. 315-318, 2006.

[12] J. Corcoles, M. A. Gonzalez and J. Rubio, "Mutual Coupling Compensation in Arrays Using a Spherical Wave Expansion of the Radiated Field," *IEEE Antenna and wireless Propagation Letters.* 8: pp. 108-111, 2009.

[13] H. S. Lui, and H. T. Hui, "Effective Mutual Coupling Compensation for Direction-of-Arrival Estimations Using a New, Accurate Determination Method for the Receiving Mutual Impedance," *J. of Electromagn. Waves and Appl.*, vol. 24, pp. 271-281, 2010.

[14] Z. Ye, and C. Liu, "On the Resiliency of MUSIC Direction Finding Against Antenna Sensor Coupling," *IEEE Trans. Ant. Propagat.,* vol. 56, no. 2, 2008.

[15] M. D. Zoltowski, M. Haardt and C. P. Mathews, 'Closed-form 2-D Angle Estimation with Rectangular Arrays in Element Space or Beam Space via Unitary ESPRIT', *IEEE Trans. Signal Process.,* vol. 44, pp. 316-328, 1996.

[16] Z. Ye, and C. Liu, "2D DOA Estimation in the Presence of Mutual Coupling," *IEEE Trans. Antennas and Propagat.,* vol. 56, no. 10, 2008.

[17] Y. C. Yu, M. Okada and Yamamoto, "Dummy Elements Add on Both Sides of Monopole- Array Assisted Doppler Spread Compensator for Digital Terrestrial Television Broadcasting Receiver," *in Proc. IEEE Int. Workshop on antenna Technology Small Antennas and Novel Metamaterials*, pp. 377-380. 2006.

[18] Y. Hua and T. K. Sarkar "On SVD for Estimating Generalized Eigenvalues of Singular Matrix Pencil in Noise," *IEEE Transactions on Signal Processing,* SP-39, 4, pp. 892-900, April 1991.

[19] T. Svantesson, "Modeling and Estimation of Mutual Coupling in a Uniform Linear Array of Dipoles," *in Proc. IEEE Int. Conf. Acoustics, Speech, Signal Processing,* vol. 5, pp. 2961-2964, Mar. 1999.

Ali Azarbar was born in Tehran, Iran, in 1972. He received the B.Sc. and M.Sc. degree, both in communication engineering from Sharif University, Tehran, Iran in 1994 and 1997, respectively and Ph.D. degree in communication engineering from Islamic Azad University, Tehran, Iran in 2011. His research interests are in adaptive signal processing algorithms and antenna design.

Gholamreza Dadashzadeh was born in Urmia, IRAN, in 1964. He received the B.Sc. degree in communication engineering from Shiraz University, Shiraz, Iran in 1992 and M.Sc. and Ph.D. degree in communication engineering from Tarbiat Modarres University (TMU), Tehran, Iran, in 1996 and 2002, respectively.

He is a member of IEEE, Institute of Electronics, Information and Communication Engineers (IEICE) of Japan and Iranian Association of Electrical and Electronics Engineers (IAEEE) of Iran. He honored received the first degree of national researcher in 2007 from Iran's ministry of ICT. He has published more than 70 papers in referred journals and international conferences in the area of antenna design and smart antennas.

Hamidreza Bakhshi was born in Tehran, Iran on April 25, 1971. He received the B.Sc. degree in electrical engineering from Tehran University, Iran in 1992, the M.Sc. and Ph.D. degree in Electrical Engineering from Tarbiat Modarres University, Iran in 1995 and 2001, respectively. Since 2001, he has been as an Assistant Professor of Electrical Engineering at Shahed University, Tehran, Iran. His research interests include wireless communications, multiuser detection, and smart antennas.

A Novel UWB Filter with WLAN and RFID Stop-Band Rejection Characteristic using Tri-Stage Radial Loaded Stub Resonators

Chengyuan Liu, Tao Jiang, Yingsong Li, and Jing Zhang

College of Information and Communications Engineering,
Harbin Engineering University, Harbin, Heilongjiang, 150001, China
liuchengyuan@hrbeu.edu.cn, liyingsong@hrbeu.edu.cn

Abstract ─ The paper presents a novel approach for designing compact ultra-wideband (UWB) band-pass filter with WLAN and RFID stop-band rejection characteristic which is obtained by using tri-stage radial loaded stub resonators. The main advantage of the proposed filter is that the Stop-band can perfectly reject the WLAN and RFID (5.2GHz-6.1GHz) signals. The density and the equivalent model of one filter for testing the presented design is given depending on the odd/even excitation resonance condition. The characteristics of the filter are analyzed and discussed. To verify the proposed methods, two filters are designed and fabricated. Measured results show the proposed UWB properties from 3 GHz to 10.8 GHz and stop-band properties from 5.2 GHz to 6.1GHz. The designed filters can be integrated in UWB radio systems and can efficiently enhance the interference immunity from undesired signals such as wireless local area network (WLAN) and RFID.

Index Terms - Band-pass filter, dual-band, tri-stage radial loaded stub resonator, UWB, WLAN and RFID stop-band rejection

I. INTRODUCTION

Since the Federal Communications Commission (FCC) released the frequency band from 3.1GHz to 10.6 GHz for commercial applications in February 2002, the ultra-wideband (UWB) radio system has been receiving great attention from both academy and industry [1]. UWB bandpass filter (BPF) is one of the key passive components to implement UWB radio systems. Therefore, more requirements have been proposed on the design methodology of BPFs with large fractional bandwidths (FBWs). Recently, a few methods and structures have been presented to develop UWB BPFs [2]-[5]. Generally, typical structures include a low and high-pass filter configuration [2], coplanar waveguide (CPW) [3], Right/Left-Handed Structure [4], microstrip fork-form resonators [5], split-ring resonators [6], circular slots in ground plane [7], multi-mode resonators (MMR) [8]. Though most of the UWB BPFs are suitable for application, they have some imperfections, such as bad out-of-band performance and complex structure.

Moreover, the UWB frequency band overlaps with some existing telecommunication bands such as WLAN RFID and WiMAX which indicate that they may interfere with UWB systems and vice versa. Therefore, a compact communication system which operates in UWB frequency band requires two types of filters. The first is a small BPF with a notched band (bandwidth is less than 150MHz.) in order to avoid being interfered by the undesired radio signals. The second is a compact BPF with stop-band rejection characteristic in order to avoid being interfered by the undesired radio signals and to get good UWB signal. Recently, there are many methods that have been investigated to design filters for the first kind with a notched band, such as embedded open-circuited stub [9], defected ground structures (DGS) [10], mismatch transmission line [11], Tri-layer structure [12], open-loop structure [13], E-shaped Microstrip SIR [14], surface-coupled structure [15] and parasitic coupled line [16] which can effectively isolate undesired radio signals. For the second kind UWB filter, there are not effective ways to complete this design. Because general

Submitted On: Feb. 23, 2012
Accepted On: July 24, 2012

structures cannot achieve stop-band rejection characteristic near 1GHz (5.2GHz-6.1GHz). Several methods have been developed and investigated for designing this kind of filters [17-18]. However, these structures are difficult in integrating into UWB filter.

The present paper provides a new implementation of stop-band rejection characteristic by using tri-stage radial loaded stub resonators. The tri-stage radial loaded stub resonators is designed based on the loaded stub resonator. The loaded stub resonator has a good dual-mode resonance characteristic which is widely used to design dual-band UWB bandpass filter [19-20]. Different with the general dual-band filter designed, in this article we use tri-stage radial loaded stub resonators to get WLAN and RFID stop-band rejection characteristic. The tri-stage radial loaded stub resonator also has good dual-mode characteristic. The odd mode resonance is used to design the UWB filter. At the same time, the even mode resonance is regarded as a band reject block. By changing the tri-stage radial loaded stub resonator, the odd mode is hardly changed. So the frequency of the stop-band can alter optionally to reject different signals. Furthermore, the width of the stop-band could be expanded by adjusting the length of the middle stage radial loaded stub. The filter performance is simulated by using the CST software and it is implemented on the substrate with a relative dielectric constant of 10.8 and a thickness of 0.635 mm. Simulated and measured results agree reasonably well.

II. FILTER DESIGN AND ANALYSIS

In this Section, the theoretical design and synthesis of a compact UWB BPF with stop-band rejection characteristic using dual-/tri-stage radial loaded stub resonators is presented. The proposed filter design essentially exploits the dual-/tri-stage radial loaded stub structures for the realization of good WLAN and RFID stop-band rejection characteristic. This section is organized as follows. Section 2.1 outlines the characteristics of the compact UWB BPF with good WLAN and RFID stop-band rejection characteristic using dual-stage radial loaded stub. In addition, the corresponding lumped equivalent circuits and formulas are provided. But this method still has a little disadvantage such as narrow bandwidth of stop-band rejection characteristic. To overcome that problem, we use the tri-stage radial loaded stub to substitute for dual-stage radial loaded stub. The modified filter using tri-stage radial loaded stub is described in section B.

A. UWB BPF with Stop-band characteristic using Dual-stage radial loaded stub

The schematic and equivalent transmission line model of the investigated UWB BPF with wide stop-band rejection is shown in Fig. 1.

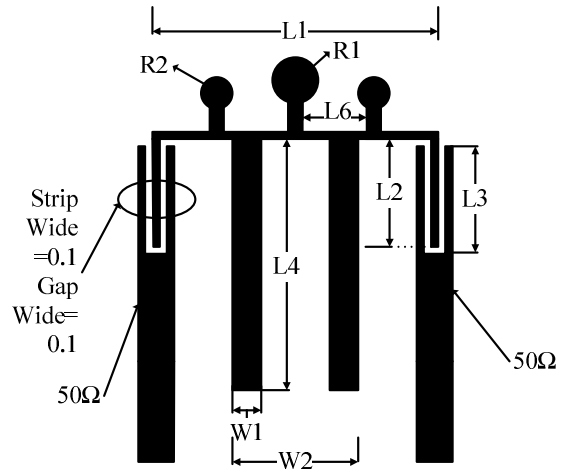

(a) The layout,

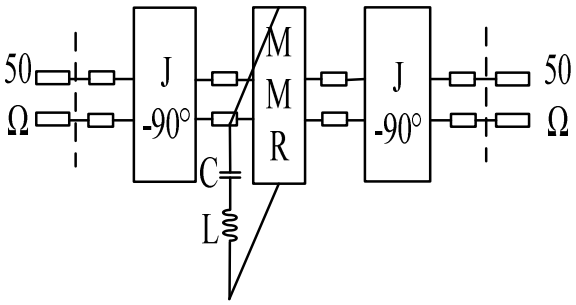

(b) equivalent circuit network of the filter,

Fig. 1 Geometry of the proposed UWB filter using dual-stage radial loaded stub.

The proposed UWB filter consists of stubs-loaded MMR at the center section and two identical coupled-lines located at the left and right section. The proposed BPF is a modified form of [8] and the dual-stage radial loaded stub is coupled to the middle MMR section to achieve the stop-band rejection characteristic. Fig. 1 (b) illustrates the equivalent transmission line network of the proposed filter. The inter-digital coupled line can be

equaled as two single transmission lines at two sides and a J-inverter susceptance in the middle. This MMR is formed by attaching three round stubs in the middle section. They can work together to produce an extended stop-band in the higher frequency range. On the other hand, the middle section of the constituted MMR also exhibits an excellent low-pass property with sharpened rejection skirt.

The dual-stage radial loaded stub inserted into the middle section of the MMR can be seen as a shunt series resonant branch. This branch is regarded as a capacitor and cascade inductors. The dual-stage radial loaded stub is designed based on the radial-UIR loaded stub. The detailed analysis of radial-UIR loaded stub could be found in our previous study [21]. The radial-UIR loaded stub's equivalent model can be seeing shown in Fig. 2.

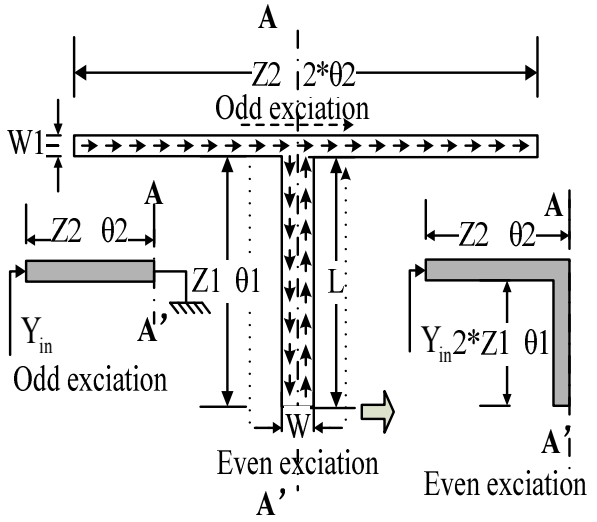

Fig. 2 equivalent mode diagram of the radial-UIR loaded stub.

From Fig. 2, the radial-UIR loaded stub can be analyzed in terms of even and odd mode (the AA' plane behaves as an electric/magnetic wall for odd/even mode). For odd mode, the center UIR has no influence on the electrical response while the radial-UIR loaded stub is relevant to even mode response. The even mode excitation condition can be extracted from resonant condition is expressed as follows [22]:

$$Y_{in} = jY_2 * \frac{2(R_Z \tan\theta_1 + \tan\theta_2)(R_Z - \tan\theta_1 \tan\theta_2)}{R_Z(1-\tan^2\theta_1)(1-\tan^2\theta_2) - 2(1-R_Z^2)\tan\theta_1 \tan\theta_2},$$

$R_Z = \frac{Z_2}{Z_1}$. Resonant conditions are obtained by taking $Y_{in} = 0$. Thus we can get

$$(R_Z \cot\theta_2 + \cot\theta_1)(R_Z \cot\theta_1 \cot\theta_2 - 1) = 0.$$

In this filter $Z_2 = 90\Omega$, $\theta_2 = 90°$ and $Z_1 = 72\Omega$. So we can get $\theta_1 = 90°$. Then the length of the stub is designed near $\lambda_{notch}/4$ which is illustrated as follows:

$$\lambda_{notch} = \frac{C}{f_{notch}\sqrt{\varepsilon_{eff}}},$$

$$\varepsilon_{eff} = \sqrt{\frac{\varepsilon_r + 1}{2}},$$

where λ_{notch} is the wavelength of the center frequency of the notch band, f_{notch} is the center frequency of the notch band, ε_r is the relative dielectric constant, ε_{eff} is the effective dielectric constant, and C is the speed of light.

In this paper, we want to get a wide stop-band rejection characteristic. From [19], we know that the width of the radial-UIR loaded stub can control the width of the stop-band. The effects of the wide stop-band characteristic has been investigated. Fig. 3 shows the response |S21| of the mentioned filter with various W. By increasing the width of radial-UIR loaded stub, the width of the stop-band is changed.

From Fig. 3, it is clear that the bandwidth of the stop-band increases to the wider level with the increase of W. More specifically, the width of the stop-band (-20dB) would increase to near 1GHz

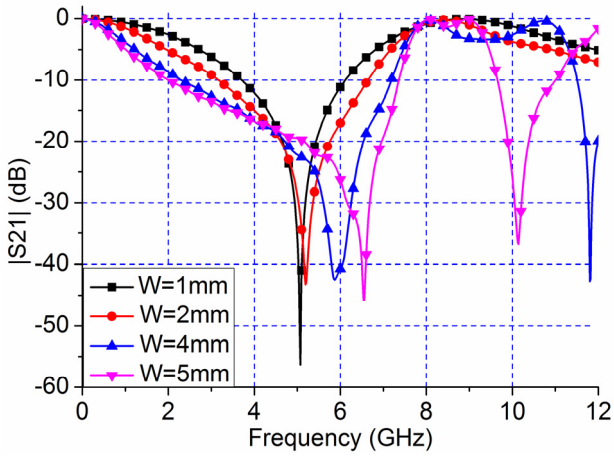

Fig. 3 Simulated |S21| of the stub for different W with other parameter fixed.

when the width of the stub is increased to 4mm. Although this method could obtain enough bandwidth of the stop-band, there is a very poor rectangular coefficient. In addition, there would be a spurious frequency from 10GHz to 14GHz. The spurious frequency could influence the pass-band of UWB filter. In another case, the width of the stub (W) is far greater than the width of branch (W1). So discontinuities in the transmission-line should be taken into consideration. This will increase the difficulty of accurate design.

To overcome that problem, we should use other structures to substitute for general radial-loaded stub. At first, we analyze the current density of the proposed general radial-loaded stub. Figure 4 shows the current density of the general stub at the frequency of pass-band and at the stop-band frequency.

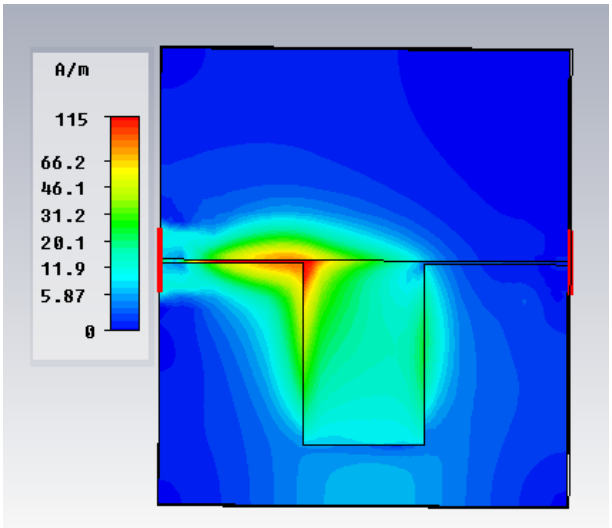

Fig. 4 Current density of the general stub at the stop-band frequency (f=6GHz).

It can be seen from the current density of the structure in the pass-band frequency that the stub does not resonate and has no effect on the overall performance. At the stop-band frequency (f=6GHz), the stub resonates with a much higher current density along the two edges of the general radial-loaded stub. At the same time, we can clearly see that the middle of the stub has lower current density. By cutting out the lower current density part and retain the higher current density part, we could get degenerate radial loaded stub (dual-stage radial loaded stub). By using this method, we could obtain reasonable current distribution. The (the ratio of W/W1) discontinuities of this structure is also reduced at the same time.

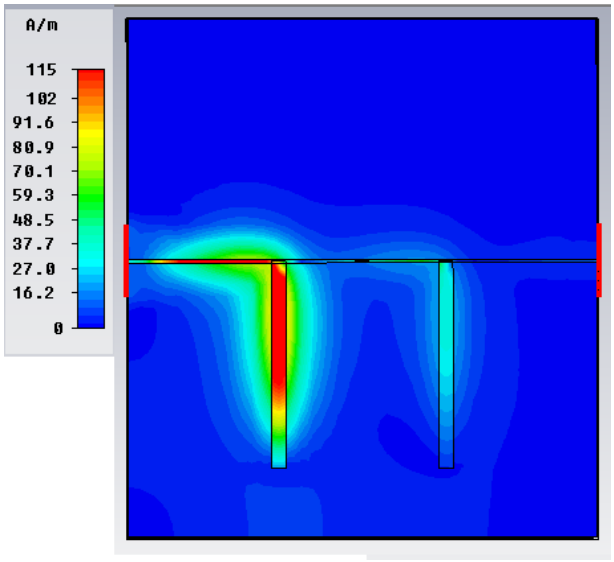

Fig. 5 Current density of the dual-stage radial loaded stub at the stop-band frequency (f=6GHz).

From Fig. 5, it can be seen clearly that the degenerated radial loaded stub (dual-stage radial loaded stub) could achieve the function of the general stub well. Next, we compare the simulation results of the two kinds of stubs to verify the effectiveness of the method further.

It can be seen from Fig. 6 that good wide stop-band rejection has been achieved by using the dual-stage radial loaded stub. From the comparison

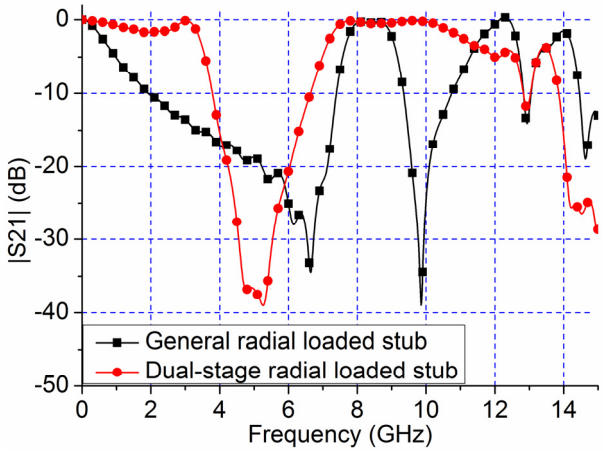

Fig. 6 Comparison of simulated |S21| of Dual-stage stub and general stub.

of simulated |S21| of the dual-stage stub and general stub, we can see that dual-stage stub can generate good rectangular coefficient and reject spurious frequency response at the same time. Figure 7 shows response |S21|of the mentioned filter with various L4.

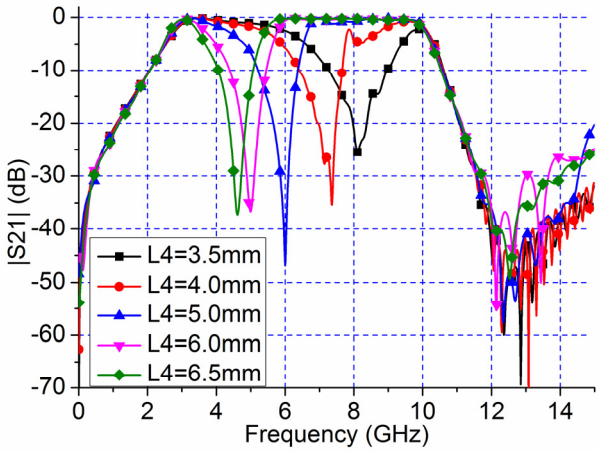

Fig. 7 Simulated |S21| of the proposed filter in Fig. 1 for different L4 with other parameter fixed.

Form Fig. 7, it is found that the center frequency of the stop-band shifts to the lower level with the increase of L4. However, the filter can always maintain nearly 500 MHz of bandwidth within stop-band. Because the dual-stage radial loaded stub resonators is a degenerated form of general stub, so this structure inherited the advantages of the original structure. The frequency of the stop-band can be easily controlled by adjusting the dimensions of the dual-stage radial loaded stub resonator. More specifically, the filter could block undesired existed radio signals (except WLAN and RFID) from UWB communication. Although the dual-stage radial loaded stub resonator can get a good stop-band rejection characteristic, it is still not convenient for the design via limited design parameters. On the other hand, the rectangular coefficients of dual-stage radial loaded stub are not good enough from the Fig. 7. To overcome that problem, we substitute the tri-stage radial loaded stub for the dual-stage radial loaded stub.

B. UWB BPF with stop-band characteristic using Tri-stage radial loaded stub resonator

Compared with the dual-stage radial loaded stub resonator, tri-stage radial loaded stub resonator has a wider degree of the freedom in structure and design. The schematic of the proposed filter using tri-stage radial loaded stub is shown in Fig. 8. Compared with the designed filter in Fig. 1, the difference is the inner stub. The additional stub can bring extra resonant frequency and expand the stop-band bandwidth. Comparison of simulated |S21| of these mentioned two filters is shown in Fig. 9. From the Fig. 9, it is clear to see that if the middle stub is added, the width of stop-band would be twice of that of the dual-stage radial loaded stub. In order to get more detailed research results, the UWB filter using tri-stage radial loaded stub resonator is analyzed using CST and discussed herein. Figures 10 and 11 show the filter response |S21| of with varying L5 (L5<5mm and L5>5mm).

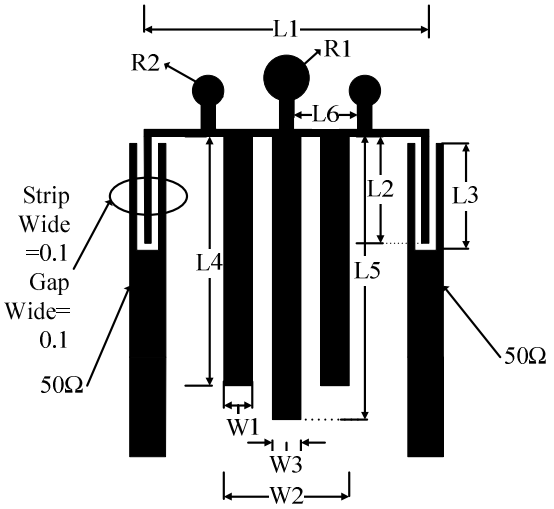

Fig. 8 Geometry of the proposed UWB filter using tri-stage radial loaded stub.

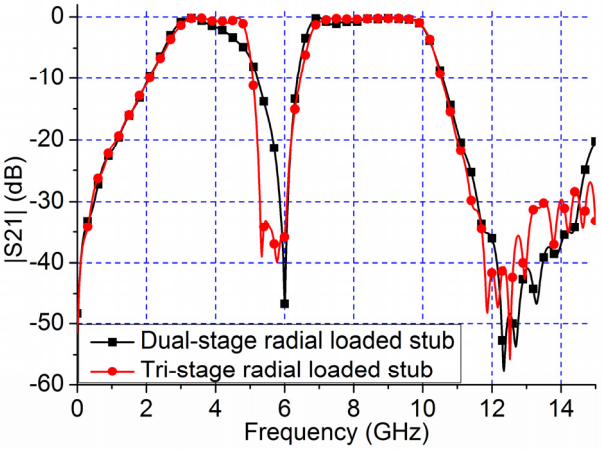

Fig. 9 Comparison of simulated |S21| of these mentioned two filters.

There have one point need to be noted is that when L4=L5=5mm, the bandwidth of stop-band is the same as using the dual-stage radial loaded stub. This is because of that the tri-stage radial loaded stub could be seen as degenerated radial loaded stub when L4=L5=5mm.

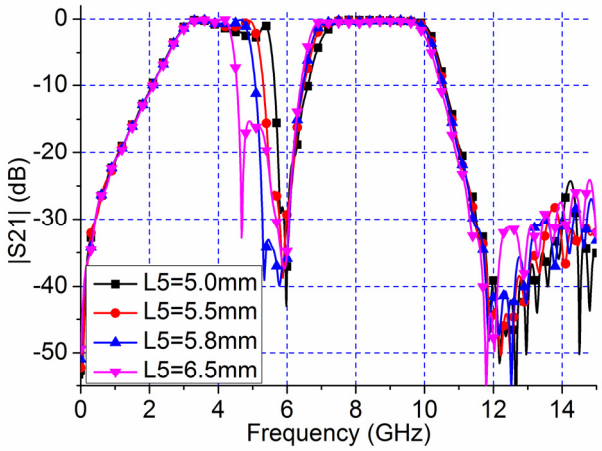

Fig. 10 Simulated |S21| of the proposed filter for different L5 with other parameter fixed (L5>5mm).

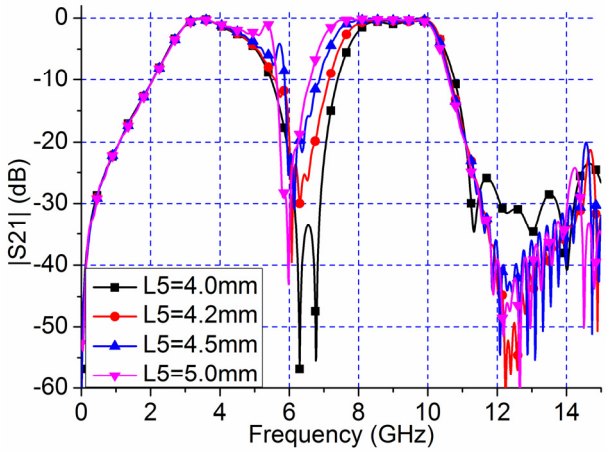

Fig. 11 Simulated |S21| of the proposed filter for different L5 with other parameter fixed (L5<5mm).

From the Fig. 10, it is clear to see that if the middle stub L5 increases (L5), the stop-band would expand to a lower level. In other words, an increase of L5 can expand the stop-band to the lower level. Furthermore we could see that the middle stub brings out an additional frequency. When the additional frequency moved to the lower, the stop-band could expand to near 1GHz. It's worth noting that the stop-band would be distorted with L5=6.5mm.

From Fig. 11, it is clear to see that if the middle stub L5 decreases (L5), the stop-band could expand to a higher level. In other words, a decrease of L5 could expand the stop-band to a higher level. As the same as Fig. 10, the middle stub brings out an additional resonance frequency. When the additional frequency moves to a higher level, the stop-band also expands to near 1GHz. Based on the above discussions, the resonance frequency of the stop-band can be easily controlled by adjusting the dimensions of the dual/tri-stage radial loaded stub. More specifically, the filter using dual-stage radial loaded stub could block most undesired existed radio signal (except WLAN and RFID) within the UWB operation band. The filter using tri-stage radial loaded stub could block all undesired existed radio signals within UWB communication.

Based on the above parametric study, the proposed filter is optimized and manufactured after several adjustments of different parameters. Figure 12 and Fig. 13 shows the simulated results of different L3 and W3. According to the details of Fig. 12 and Fig. 13, the optimal dimensions can be determined. The final dimensions of the designed filter are as follows: L1=6.4mm, L2=3.7mm, L3=4mm, L4=6mm, L5=1.8mm, L6=1.5mm, R1=0.6mm, R2=0.5mm, W1=0.1mm, W2=1mm.

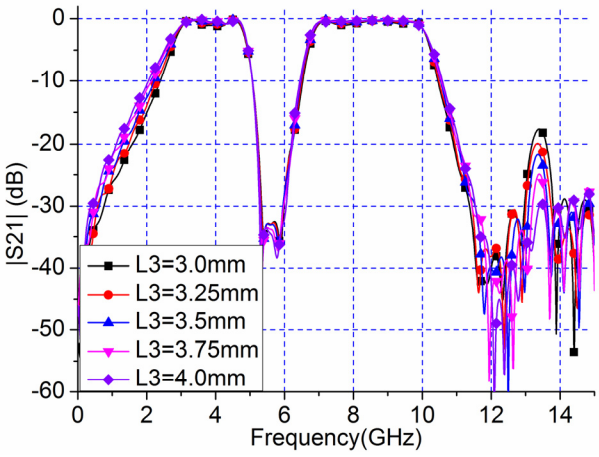

Fig. 12 Simulated |S21| of the proposed filter for different L3.

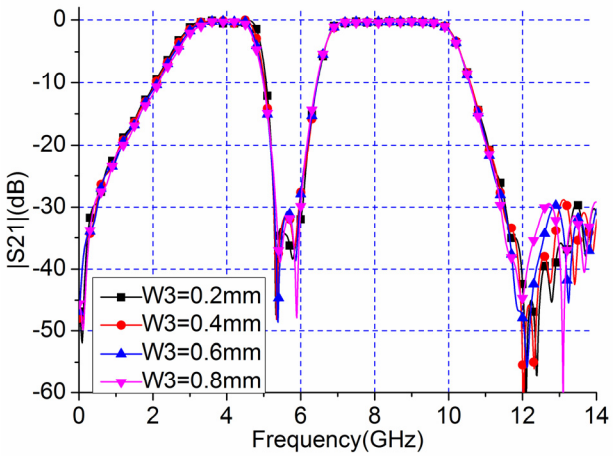

Fig. 13 Simulated |S21| of the proposed filter for different W3.

III. EXPERIMENTAL RESULT

To verify the effectiveness of the proposed filters, the proposed dual-wideband BPFs with stop-band rejection characteristic using dual/tri-stage radial loaded stub resonators are designed, simulated, fabricated and measured. To compare the difference of the two designs, basic parameters of the two filters are the same. Figure 14 is the photograph of the fabricated filters. The overall circuit size of these filters are less than 10mm×10mm, so these filters are compact.

The proposed dual-wideband BPFs with wide stop-band rejection characteristic using dual/tri-stage radial loaded stub is measured by Anristu 37347D vector network analyzer. Figure 15, Fig. 16, Fig. 17 and Fig. 18 demonstrate the frequency responses and group delay of proposed filters. The excellent agreement is obtained when compared with simulated ones. Both of the simulation and modified filter using dual-stage radial-loaded stub. Measured results of the two filters show that the two filters have two pass bands and a stop-band rejection characteristic. Form Fig. 15, the first one is a filter whose center frequency is 6GHz, -3dB fractional bandwidths are 3.1GHz-4.2GHz and 6.5GHz-10.6GHz and -20dB fractional stop-band bandwidths is 5.6-6.2GHz (591MHz). The second one, shown in the Fig. 17, is a filter whose center frequency is 5.6 GHz, -3dB fractional bandwidths are 3.1GHz-4.86GHz and 6.76GHz-10.6GHz and -20dB fractional stop-band bandwidths is 5.2GHz-6.2GHz (1GHz). The only difference of the two filters is that we substituted the tri-stage radial loaded stub for the dual-stage radial loaded stub when the second filter was designed. So we expanded the bandwidth of the stop-band to the higher level. The changing trends of the stop-band show that the filter using tri-stage radial loaded stub can improve rectangular coefficient effectively comparing to the dual-stage radial loaded stub. Because the tri-stage radial loaded stub add a parameter, which made the modified filter have a wide degree of the freedom in structure and design.

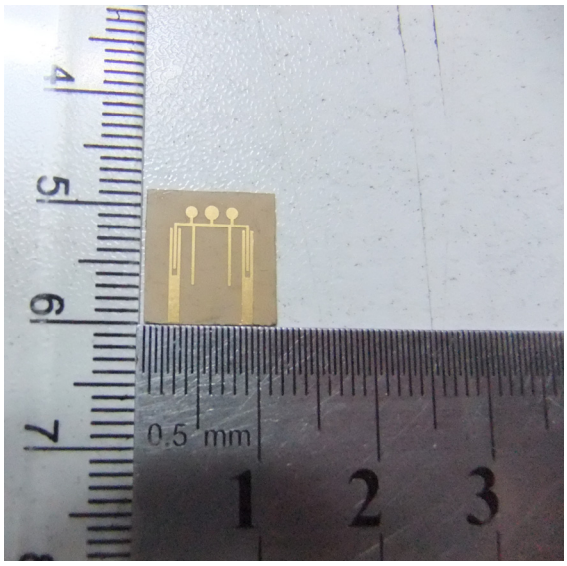

(a) filter using dual-stage radial loaded stub,

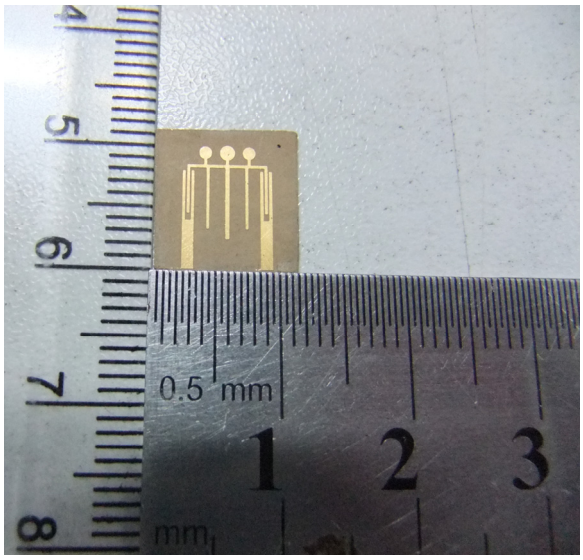

(b) filter using tri-stage radial loaded stub

Fig. 14 Phototype and of the fabricated filter.

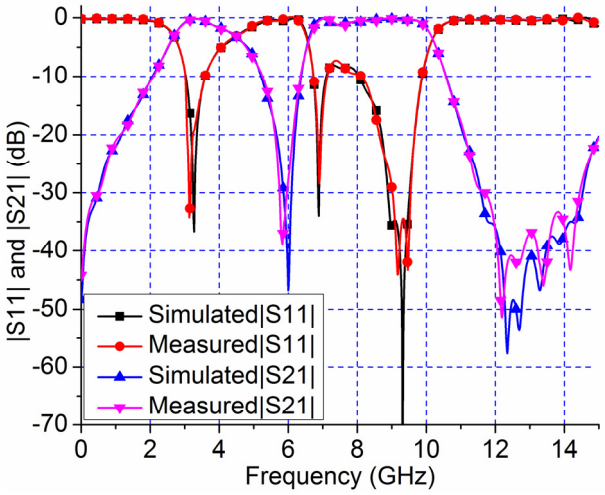

Fig. 15 Comparison of simulated and measured |S11| and |S21| using dual-stage radial-loaded stub.

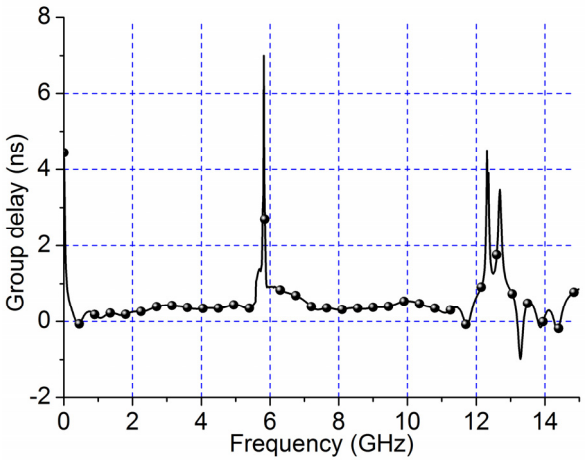

Fig. 16 Measured group delay of the fabricated.

The simulated and measured results show good agreement. This minor discrepancy between simulated and measured results should be caused by insertion loss of SMA connectors and unexpected tolerances in fabrication, material parameters and solder etc. As shown in Fig. 15 and Fig. 17 the measured insertion loss is less than 0.5dB. The rejection between the two transmission bands is more than 25 dB. As shown in Fig. 16 and Fig. 18, the measured group delay is between 0.2ns and 0.6 ns with a maximum variation of 0.6 ns in the two pass-band and more than 2ns in the middle stop-band. At upper rejection band, the presented filters have deeper and wider stop-band attenuation which is more than -25 dB from 11 to 15 GHz.

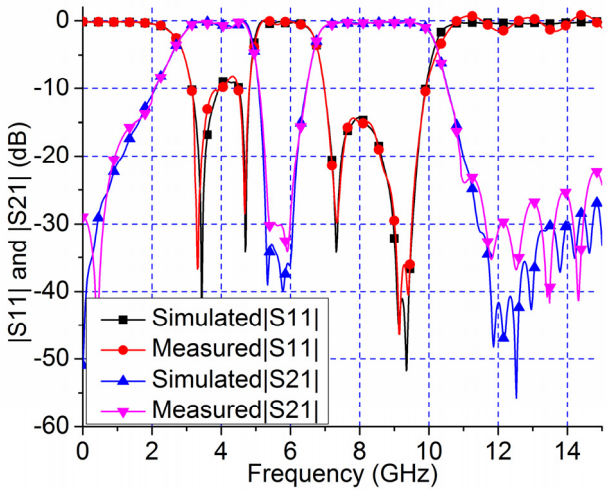

Fig. 17 Comparison of simulated and measured |S11| and |S21| using Tri-stage radial-loaded stub.

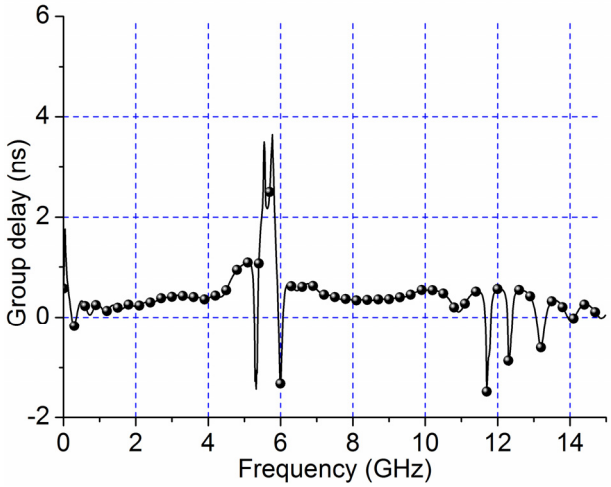

Fig. 18 measured group delay of the fabricated modified filter using Tri-stage radial-loaded stub.

It should be noted that the filters are embarrassed in that the return loss is quite high in the first pass-band since three round stubs of the origin structure [8] are cut by the filters to get enough space to design, which would reduce the strength of the resonance. So the insertion loss would have some attenuation. However, in this structure, the gap and size are so small that the attenuation can be controlled in an acceptable range. At the same time, the attenuation of the filters in the pass-band is nearly constant. Based on the above analysis, although the two filters have little defect, they are still good UWB filters with notch-band character. Simualed and

measured results show that the two filters are good ultra-wide notch-band BPFs, which can be suitable for implementing the functions of UWB system.

IV. CONCLUSION

In this paper, two compact UWB BPFs with WLAN and RFID stop-band rejection characteristic have been developed and manufactured. Inserting dual/tri-stage radial loaded stub to the original UWB BPF leads to rejection of undesired existed radio signals such as wireless local area network (WLAN) and RFID. The dual/tri-stage radial loaded stub can bring out a stop-band rejection characteristic at the desired frequency with no significant influence on the wide passband performance of the filter. In particular, changing the length of the dual-stage radial loaded stub can adjust the stop-band optionally in a wide range. Changing the length of the third-stage radial loaded stub can expand the bandwith of stop-band to 1GHz for perfect WLAN and RFID stop-band rejection characteristic.The proposed filters are promising for use in UWB systems due to their simple structures, compact size, and excellent performance.

ACKNOWLEDGMENT

This work was supported by a grant from the National Defense "973" Basic Research Development Program of China (No.6131380101), the National Nature Science Fund of China (No.60902014), Nature Science Fund of Heilongjiang (No.2006F11), Core Young Teacher Fund of Harbin Engineering University (No.0812) and Fundamental Research Funds for the Central Universities (HEUCF1208).

REFERENCES

[1] FCC, Revision of Part 15, *the Commission's Rules Regarding to Ultra-Wide-Band Transmission System, First Note and Order Federal Communication Commission*, ET-Docket pp. 98-153, 2002.

[2] C. L. Hsu, F. C. Hsu, and J. T. Kuo, "Microstrip Bandpass Filters for Ultra-Wideband (UWB) Wireless Communications", *2005 IEEE MTT-S International Microwave Symposium Digest*, pp. 679-682, 2005.

[3] H. Wang, L. Zhu, and W. Menzel, "Ultra-Wideband Bandpass Filter with Hybrid Microstrip/CPW Structure", *IEEE Microwave Wireless Compon Lett.*, vol. 15, pp. 844-846, 2005.

[4] J. Q. Huang and Q. X. Chu, "Compact UWB Band-Pass Filter Utilizing Modified Composite Right/Left-Handed Structure with Cross Coupling," *Progress In Electromagnetics Research*, vol. 107, pp. 179-186, 2010.

[5] H. Chen and Y. X. Zhang, "A Novel and Compact UWB Bandpass Filter using Microstrip Fork-Form Resonators," *Progress In Electromagnetics Research*, vol. 77, pp. 273-280, 2007.

[6] L. Qiang, Y. J. Zhao, Q. Sun, W. Zhao, and B. Liu, "A Compact UWB Bandpass Filter based on Complementary Split-Ring Resonators," *Progress In Electromagnetics Research C*, vol. 11, pp. 237-243, 2009.

[7] M. NaghshvarianJahromi and M. Tayarani, "Miniature Planar UWB Bandpass Filters with Circular Slots in Ground," *Progress In Electromagnetics Research Letters*, vol. 3, pp. 87-93, 2008.

[8] B. Yao, Y. Zhou, Q. Cao, and Y. Chen, "Compact UWB Bandpass Filter With Improved Upper-Stopband Performance", *IEEE Microwave and Wireless Components Lett.*, vol. 19, pp. 27-29, 2009.

[9] H. Shaman and J. S. Hong, "Ultra-Wideband (UWB) Bandpass Filter with Embedded Band Notch Structures," *IEEE Microw. Wireless Compon Lett.*, vol. 17, pp. 193-195, 2007.

[10] L. Chen, Y. Shang, and Y. L. Zhang, "Design of a UWB Bandpass Filter with a Notched Band and Wide Stopband," *Microwave Journal*, vol. 52, pp. 96-105, 2009.

[11] T. Jiang, C. Y. Liu, Y. S. Li, and M. Y. Zhu, "Research on a Novel Microstrip UWB Notch-Band BPF," *Asia Pacific Microwave Conference*, pp. 261-264, 2009.

[12] P. Y. Hsiao and R. M. Weng , "Compact Tri-layer Ultra-wideband Bandpass Filter with Dual Notch Bands," *Progress In Electromagnetics Research,* vol. 106, pp. 49-60, 2010.

[13] P. Y. Hsiao and R. M. Weng, "Compact Open-loop UWB Filter with Notched Band," *Progress In Electromagnetics Research Letters*, vol. 7, pp. 149-159, 2009.

[14] Y. L. Wu, C. Liao, and X. Z. Xiong, "A Dual-Wideband Bandpass Filter based on E-shaped Microstrip SIR with Improved Upperstopband Performance," *Progress In Electromagnetics Research*, vol. 108, pp. 141-153, 2010.

[15] J. Q. Huang, Q. X. Chu, and C. Y. Liu, "Compact UWB Filter based on Surface-coupled Structure with Dual Notch Bands," *Progress In Electromagnetics Research*, vol. 106, pp. 311-319, 2010.

[16] S. Pirani, J. Nourinia, and C. Ghobadi, "Band-Notched UWB BPF Design Using Parasitic Coupled Line," *IEEE Microwave and Wireless Components Lett.*, vol. 20, pp. 444-446, 2010.

[17] R. N. Baral, P. K. Singhal, "Design and Analysis of Microstrip Photonic Band Gap Filter for Suppression of Periodicity," *Applied Computational Electromagnetics Society (ACES) Journal*, vol. 25, no. 2, pp. 156-159, Feb. 2010.

[18] A. Boutejdar, M. Challal, A. Azrar, "A Novel Band-Stop Filter using Octagonal-Shaped Patterned Ground Structures along with Interdigital and Compensated Capacitors," *Applied Computational Electromagnetics Society (ACES) Journal*, vol. 26, no. 4, pp. 312-318, April 2011.

[19] L. Zhang, Z. Y. Yu, and S. G. Mo,"Novel Plane Multimode Bandpass Filters with Radial-line Stubs," *Progress In Electromagnetics Research*, vol. 101, pp. 33-42, 2010.

[20] M. D. C. Velazquez-Ahumada, J. Martel-Villagr, F. Medina, and F. Mesa,"Application of Stub Loaded Folded Stepped Impedance Resonators to Dual Band Filters," *Progress In Electromagnetics Research*, vol. 102, pp. 107-124, 2010.

[21] C. Y. Liu,T. Jiang,Y. S. Li, A Novel UWB Filter with Notch-band Characteristic using Radial-UIR/SIR Loaded Stub Resonators, *Journal of Electromagnetic Waves and Applications*, vol. 25, no. 2, pp. 233-245, 2011.

[22] Hong, J. S. and M. J. Lancaster, *Microstrip Filters for RF/Microwave Applications*, Wiley, New York, 2001.

Cheng-yuan Liu received his B.S. degree in electrical and information engineering in 2006, and M.S. degree in Electromagnetic Field and Microwave Technology from Harbin Engineering University, 2006 and 2011, respectively. Now he is a Ph.D. Candidate in Harbin Engineering University, China. He serves as receivers for the Journal of Electromagnetic Waves and Applications, Journal of Microwaves, Optoelectronics and Electromagnetic Applications, and Progress in Electromagnetics Research Series, Journal of Electromagnetic Waves and Applications. His research interests are mainly in microwave theory, UWB antenna and UWB filters.

Tao Jiang received his bachelor's degree in electrical engineering in 1994, his master's degree in information and signal processing in 1999 and his doctorate in communication and information systems in 2002 from Harbin Engineering University, China. He worked in the Harbin Institute of Technology, China as a post-doctoral fellow in 2003 and worked in the National University of Singapore as a research fellow in 2004. He is a professor in the Harbin Engineering University, China. His research interests are mainly in computational electromagnetics, microwave engineering, radio wave propagation and navigation and EMC.

Yingsong LI received his B.S. degree in electrical and information engineering in 2006, and M.S. degree in Electromagnetic Field and Microwave Technology from Harbin Engineering University, 2006 and 2011, respectively. Now he is a Ph.D. Candidate in Harbin Engineering University, China. He is a student member of Chinese Institute of Electronics (CIE), IEEE, IEICE and The Applied Computational Electromagnetics Society (ACES). He serves as receivers for the journals IEEE Antennas and Wireless Propagation Letters, Electronics Letters, International Journal of Electronics, Progress in Electromagnetics Research Series, Journal of Electromagnetic Waves and Applications, Applied Computational Electromagnetics Society Journal and COMPEL: The International Journal for Computation and Mathematics in Electrical and Electronic Engineering. His recent research interests are mainly in microwave theory, microwave and millimeter-wave circuits, small antenna technologies and computational electromagnetic.

Jing Zhang received her B.S. degree in electrical and information engineering in 2008, and M.S. degree in Signal and information processing from Harbin Engineering University, 2008 and 2011, respectively. Now she is a Ph.D. Candidate in Harbin Engineering University, China. His research interests are mainly in radar signal processing and UWB antenna and UWB filters.

Enhanced Bandwidth Small Square Monopole Antenna with Band-Notched Functions for UWB Wireless Communications

Behrang Hadian Siahkal-Mahalle [1], Mohammad Ojaroudi [2], and Nasser Ojaroudi [3]

[1] Department of Electrical Engineering
Aeronautical University of Science and Technology, Tehran, Iran.
(E-mail: hadian12@yahoo.com).

[2] Young Research Group
Ardabil Branch, Islamic Azad University, Ardabil, Iran
m.ojaroudi@iauardabil.ac.ir

[3] Faculty of Electrical & Computer Engineering
Shahid Rajaee Teacher Training University, Tehran, Iran
n_ojaroudi@srttu.edu

Abstract ─ A novel multi-resonance small square monopole antenna with frequency band-notched function is presented. By cutting two modified C-shaped slots in the ground plane bandwidth is increased that provides a wide usable fractional bandwidth of more than 145% (2.85- 17.83). In order to achieve band-rejected function a pair of C-shaped parasitic structures were inserted in the ground plane and a frequency notched band of 5.08–5.93 GHz has been received. The measured results reveal that the bandwidth of the proposed antenna is from 2.85 GHz to 17.83 GHz for VSWR<2. Simulated and experimental results obtained for this antenna show that it exhibits good radiation behavior within the UWB frequency range. The designed antenna has a small size of 12×18 mm^2.

Index Terms ─ Printed Monopole Antenna (PMA), C-shaped parasitic structure, modified ground plane, ultra-wideband (UWB).

I. INTRODUCTION

In UWB communication systems, one of key issues is the design of a compact antenna while providing wideband characteristic over the whole operating band [1]. Consequently, a number of printed microstrip antenna by the combination of different shapes of strips, feed lines and ground planes with different geometries to generate more resonant modes for a wider impedance bandwidth have been experimentally characterized [2-8]. In [2], two parasitic strips along the microstrip feed line are used to enhance the impedance bandwidth. Using T-shaped strips and L-shaped slots are the methods used in [3] and [4] to excite more resonances. Moreover, other strategies to improve the impedance bandwidth which do not involve a modification of the geometry of the planar antenna have been investigated [5]-[7].

The frequency range for UWB systems between 3.1 to 10.6 GHz will cause interference to the existing wireless communication systems, such as, the wireless local area network (WLAN) for IEEE 802.11a operating in 5.15–5.35 GHz and 5.725–5.825 GHz bands, so the UWB antenna with a band-stop performance is required. In order to generate the frequency band-notch function, modified planar monopoles have been recently proposed [8-11]. In [8] and [9], different shapes of the slits (i.e., W-shaped and folded trapezoid) are used to obtain the desired band-notch characteristics. Multiple half-wavelength U-shaped slits are embedded in the radiation patch to

Submitted On: Jan. 22, 2012
Accepted On: July 24, 2012

generate the single and multiple band-notch functions, respectively [11]. In [8]-[11], however the elements were developed on the same layer within the antenna radiator or on the backed side of the layer for generating single frequency band-notched antennas. Therefore, due to the space limitation, it is difficult to generate dual/multiple notches. On the other hand, in [8]-[10], the designs have complicated structures leading to increased fabrication costs, antenna size, and difficulty in the integration with microwave integrated circuits. In [12], band-notch function is achieved by using a T-shaped coupled-parasitic element in the ground plane. Two rod-shaped parasitic structures behind the radiating patch are used to generate a band-stop performance in [13].

In the proposed structure, based on Defected Ground Structure (DGS), by cutting two C-shaped slots on the ground plane, additional resonances are excited which leads to a bandwidth improvement that achieves a fractional bandwidth of more than 145% (2.85-17.83 GHz), with respect to the multi-resonance performance. Also, based on Electromagnetic Coupling Theory (ECT), band-notch function is provided by inserting two C-shaped parasitic structures. In the monopole antenna design, by reducing the antenna size, the impedance matching at lower frequencies becomes poor and the bandwidth is degraded. The distinctive point of the proposed antenna is that although it has small size respect to the antennas introduced in [6]-[12], it has wider impedance bandwidth in the frequency band of 2.85 to over 178.3 GHz with notched band, covering all the 5.2/5.8GHz WLAN band, and also the impedance matching at lower frequencies is very well obtained. Unlike other antennas reported in the literature up to date [8]-[12], the proposed antenna displays a good omni-directional with low cross-polarization level radiation pattern even at higher frequencies.

II. ANTENNA DESIGN

Figure 1 shows the geometry of the proposed planar monopole antenna fed by a microstrip line, which is printed on a FR4 substrate of thickness 1.6 mm, and loss tangent 0.018. As shown in Fig. 1, the presented antenna consists of a square radiating patch and modified ground plane with two C-shaped slots and parasitic structures. The basic antenna structure consists of a square patch, a feed line, and a ground plane. The square patch has a width W. The patch is connected to a feed line of width W_f and length L_f. On the other side of the substrate, a conducting ground plane of width W_{sub} and length L_{gnd} is placed. The proposed antenna is connected to a 50Ω SMA connector for signal transmission.

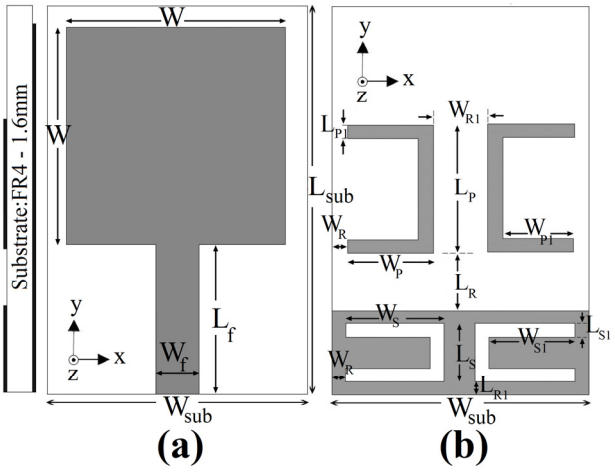

Fig. 1. Geometry of proposed square monopole antenna with modified ground plane.

In this design, to achieve a multi-resonance function and gave a bandwidth enhancement performance two C-shaped slots inserted in ground plane. By adding two C-shaped parasitic structures in the ground plane frequency band notch function (5.1-5.9GHz WLAN) is generated. Regarding Defected Ground Structures (DGS), the creating slots in the ground plane provide an additional current path. Moreover, this structure changes the inductance and capacitance of the input impedance, which in turn leads to change the bandwidth. The DGS applied to a microstrip line causes a resonant character of the structure transmission with a resonant frequency controllable by changing the shape and size of the slot [13]. Therefore, by cutting two C-shaped slots at the ground plane and carefully adjusting its parameters, much enhanced impedance bandwidth may be achieved. As illustrated in Fig. 1, the pair of C-shaped conductor-backed plane is placed under the radiating patch and is also symmetrical with respect to the longitudinal direction. The conductor-backed plane perturbs the resonant response and also acts as a parasitic half-wave resonant structure electrically

coupled to the square monopole [14]. At the notch frequency, the current flows are more dominant around the parasitic elements, and they are oppositely directed between the parasitic element and the radiation patch. As a result, the desired high attenuation near the notch frequency can be produced. The variable band-notch characteristics can be achieved by carefully choosing the parameter (L_R and L_P) for the C-shaped conductor-backed plane. In this structure, the length L_R is the critical parameter to control the filter the coupling value between ground plane and parasitic element. On the other hand, the center frequency of the notched band is insensitive to the change of L_R. The resonant frequency of the notched band is determined by L_P. In this design, the optimized length is set to band-stop resonate at approximately, where and corresponds to band-notch frequency (5.5 GHz), and also is fixed at 8 mm.

In this design, the optimized length $L_{resonance}$ is set to resonate at $0.25\lambda_{resonance}$, where $L_{resonance3} = W_S + L_{S1} + 0.5W_{S1}$, and $L_{resonance4} = 0.5W_S + 0.5W_{S1} + L_{S1}$. $\lambda_{resonance3}$ and $\lambda_{resonance4}$ corresponds to new resonance frequency at 11.5 GHz and 14.5 GHz, respectively. Also the optimized length L_{notch} is set to band-stop resonate at $0.5\lambda_{notch}$, where $L_{notch} = L_P + 2W_P$. λ_{notch} corresponds to band-notch frequency (5.5 GHz).

The final values of presented slot antenna design parameters are as follows:

TABLE I: The final dimensions of the designed antenna

Param	mm	Param	mm	Param.	mm
W_{Sub}	12	L_{Sub}	18	h_{Sub}	1.6
L_f	7	W	10	W_f	2
W_P	4.5	L_P	7.5	W_{P1}	4
L_{P1}	0.5	W_S	5	L_S	2.5
W_{S1}	4.5	L_{S1}	0.5	W_R	0.5
L_R	2	W_{R1}	2	L_{R1}	0.5

III. RESULTS AND DISCUSSIONS

In this Section, the microstrip Monopole antenna with various design parameters were constructed, and the numerical and experimental results of the input impedance and radiation characteristics are presented and discussed. The proposed microstrip-fed monopole antenna was fabricated and tested to demonstrate the effect of the presented. The parameters of this proposed antenna are studied by changing one parameter at a time and fixing the others. Ansoft HFSS simulations are used to optimize the design and agreement between the simulation and measurement is obtained [15].

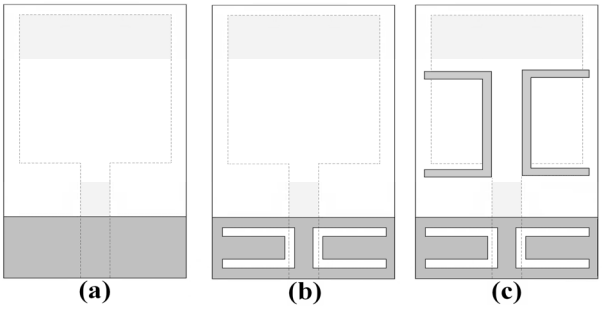

Fig. 2. (a) basic structure (ordinary monopole antenna), (b) antenna with a pair of C-shaped slots in the ground plane, (c) the proposed antenna.

The configuration of the various antennas structures are shown in Fig. 2. Return loss characteristics for ordinary square patch antenna, square antenna with two C-shaped slots in the ground plane and the proposed antenna structure are compared in Fig. 3. As shown in Fig. 3, it is observed that the upper frequency bandwidth is affected by using the C-shaped slots in the ground plane and the notch frequency bandwidth is sensitive to the C-shaped parasitic structures. Also the input impedance of the various monopole antenna structures that studied on Fig. 3, on a Smith Chart is shown in Fig. 4.

To understand the phenomenon behind this multi resonance performance, the simulated current distributions on the ground plane for the proposed antenna with two C-shaped slots at 11.5 GHz and 14.5GHz are presented in Fig. 4 (a) and 4 (b). It can be observed in Fig. 4 (a), (b) that the current concentrated on the edges of the interior and exterior of the two C-shaped slots at 11.5 GHz and 14.5 GHz. Therefore, the antenna impedance changes at these frequencies due to the resonant

properties of the C-shaped slots. It is found that by using these slots, third and fourth resonances generated at 11.5 GHz and 14.5 GHz [3]. Other important design parameters of this structure are two C-shaped parasitic structures use in the ground plane. Figure 4 (c) presents the simulated current distributions on the modified ground plane at the notch frequency (5.5 GHz). As shown in Fig. 4 (c), at the notch frequency the current flows are more dominant around of the C-shaped parasitic structures. As a result, the desired high attenuation near the notch frequency can be produced [8].

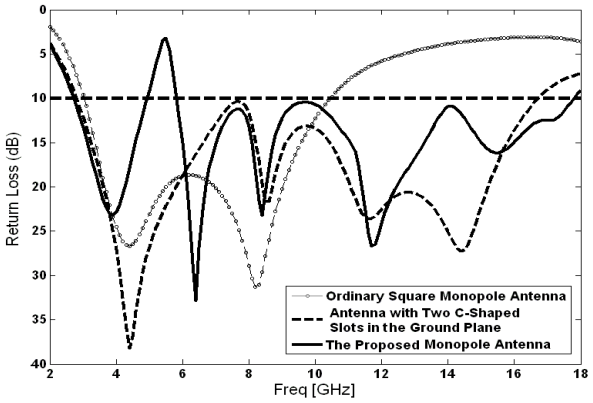

Fig. 3. Simulated return loss characteristics for the square monopole antenna without and with C-shaped slots and parasitic structures.

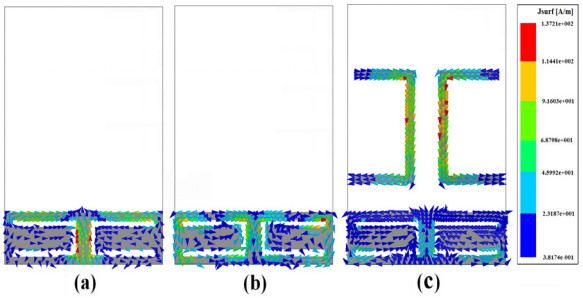

Fig. 4. Simulated surface current distributions on ground plane (a) at 11.5 GHz, (b) at 14.5 GHz, and (c) at 5.5 GHz.

The simulated VSWR curves with different values of W_{S1} are plotted in Fig. 5. As shown in Fig. 5, when the width of the W_{S1} increases from 3 to 4.75mm, the bandwidth of antenna has a various and with $W_{S1} = 4.5mm$, we gave a good bandwidth of square antenna with two C-shaped slots in the ground plane.

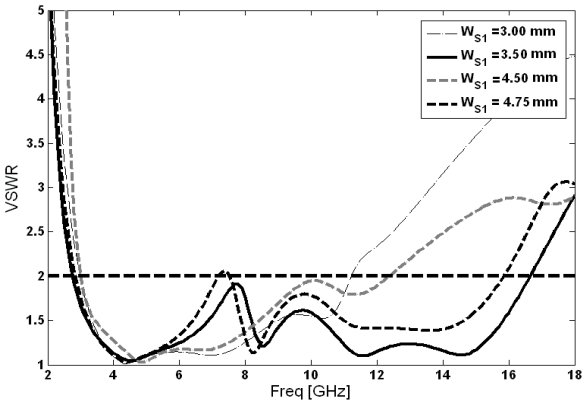

Fig. 5. Simulated VSWR characteristics for the proposed antenna without two C-shaped parasitic structures with different values of W_{S1}.

The simulated VSWR curves with different values of L_P are plotted in Fig. 6. As shown in Fig. 6, when the height of the L_P increases from 6 to 10 mm, the centre of notch frequency is decreases from 6.4 to 4.6 GHz and from these results, we can conclude that the notch frequency is controllable by changing the interior height of the L_P.

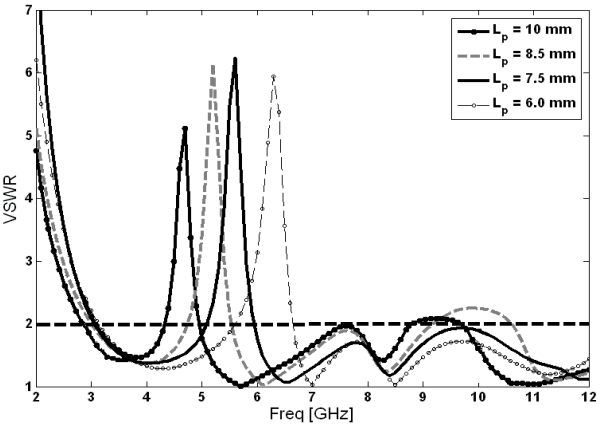

Fig. 6. Simulated VSWR characteristics for the proposed antenna with different values of L_P.

The simulated VSWR curves with different values of L_R are plotted in Fig. 7. As shown in Fig. 7, when the height of the L_R increases from 1.5 to 3 mm, the filter bandwidth is varied from 0.5 to 1.8 GHz.

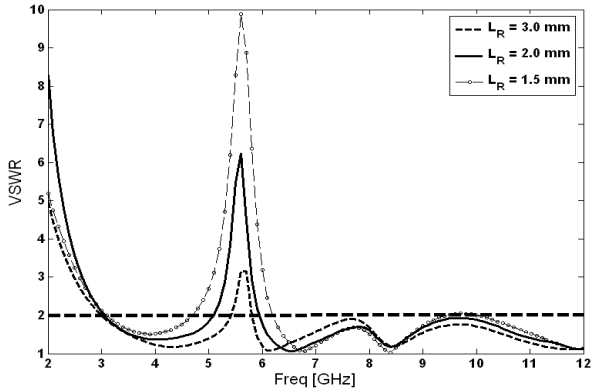

Fig. 7. Simulated VSWR characteristics for the proposed antenna with different values of L_R .

The proposed antenna with optimal design, as shown in Fig. 8, was built and tested. The measured and simulated VSWR characteristics of the proposed antenna are shown on Fig. 9. The fabricated antenna has the frequency band of 2.85 to over 17.83 GHz with notched-band function around 5.07-5.91.

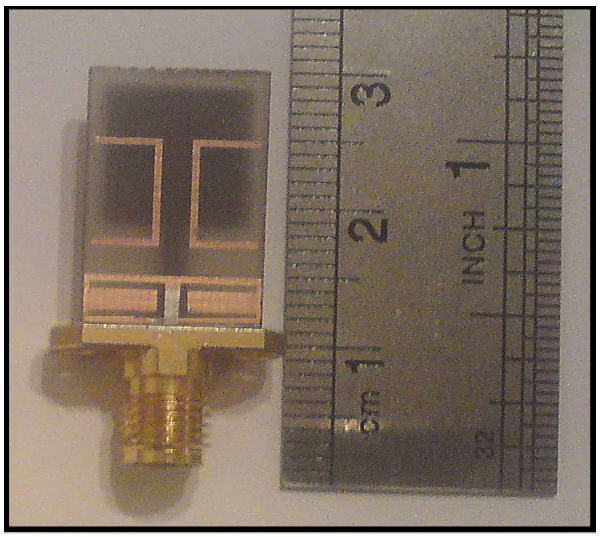

Fig. 8. Photograph of the realized printed monopole antenna.

Figure 10 illustrates the measured radiation patterns, including the Co-polarization and cross-polarization, in the H–plane (x-z plane) and E-plane (y-z plane). It can be seen that the radiation patterns in *x-z* plane are nearly omnidirectional for the three frequencies.

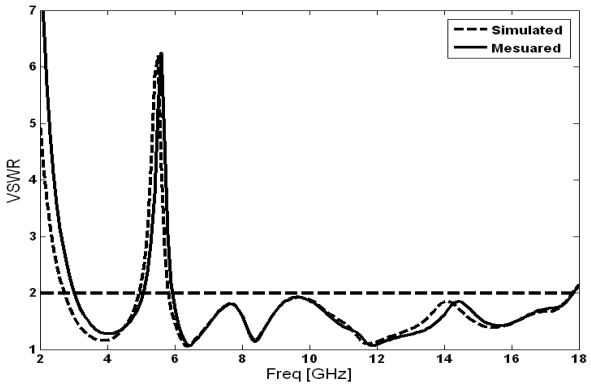

Fig. 9. Measured and simulated VSWR for the proposed antenna.

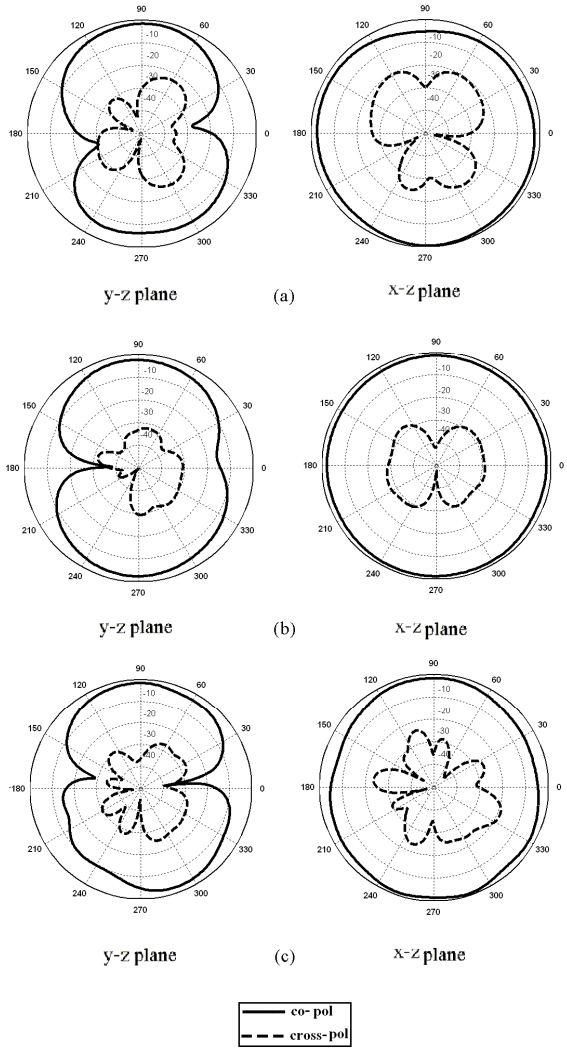

Fig. 10. Measured radiation patterns of the proposed antenna (a) 3 GHz, (b) 7 GHz, and (c) 10 GHz.

Figure 11 shows the effects of the C-shaped slots and the coupled C-shaped strips, on the maximum gain in comparison to the same antenna without them. As shown in Fig. 11, the ordinary square antenna has a gain that is low at 3 GHz and increases with frequency. It can be observed in Fig. 11 that by using a square radiating patch with a pair of C-shaped slots and parasitic structures, a sharp decrease of maximum gain in the notched frequency band at 5.5 GHz is shown. For other frequencies outside the notched frequency band, the antenna gain with the filter is similar to those without it.

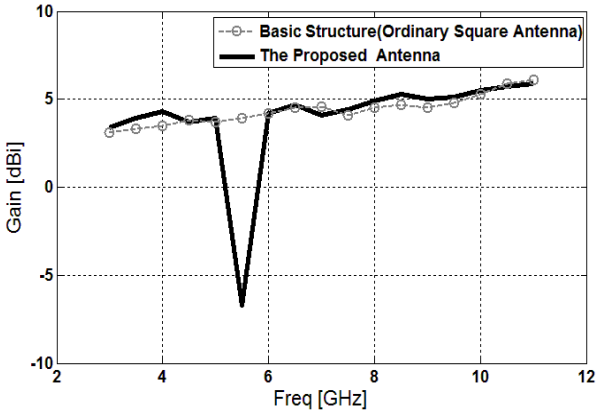

Fig. 11. Maximum gain comparisons for the ordinary square antenna (simulated), and the proposed antenna (measured).

V. CONCLUSION

In this paper, we present a novel multi-resonance microstrip-fed square monopole antenna for UWB applications with band-notch performance. The proposed antenna can operate from 2.85 to 17.83 GHz with WLAN rejection band around 5.1–5.97 GHz. In order to enhance bandwidth we insert two C-shaped slots in the ground plane, and also by adding two C-shaped parasitic structure a frequency band-notch function can be achieved. The designed antenna has a small size of 12×18 mm^2. Simulated and experimental results show that the proposed antenna could be a good candidate for UWB applications.

ACKNOWLEDGMENT

The authors are thankful to Microwave Technology (MWT) Company staff for their beneficial and professional help (www.microwave-technology.com).

REFERENCES

[1] H. Schantz, The Art and Science of Ultra Wideband Antennas, Artech House 2005.

[2] M. Ojaroudi, Sh. Yzdanifard, N. Ojaroudi, and M. Nasser-Moghaddasi, "Small Square Monopole Antenna with Enhanced by Using Inverted T-Shaped Slot and Conductor-Backed Plane", *IEEE Transactions on Antenna and Propagation*, vol. 59, no. 2, pp. 670-674, February 2011.

[3] R. Azim, M. T. Islam, N. Misran, "Design of a Planar UWB Antenna with New Band Enhancement Technique," *Applied Computational Electromagnetics Society (ACES) Journal*, vol. 26, no. 10, pp. 856-862, October 2011.

[4] M. Ojaroudi, Ch. Ghobadi, and J. Nourinia, "Small Square Monopole Antenna With Inverted T-Shaped Notch in the Ground Plane for UWB Application," *IEEE Antennas and Wireless Propagation Letters*, vol. 8, no. 1, pp. 728-731, 2009.

[5] M. Naghshvarian-Jahromi, N. Komjani-Barchloui, "Analysis of the Behavior of Sierpinski Carpet Monopole Antenna," *Applied Computational Electromagnetics Society (ACES) Journal*, vol. 24, no. 1, pp. 32-36, February 2009.

[6] D. S. Javan, O. H. Ghouchani, "Cross Slot Antenna with U-Shaped Tuning Stub for Ultra Wideband Applications," *Applied Computational Electromagnetics Society (ACES) Journal*, vol. 24, no. 4, pp. 427-432, August 2009.

[7] Sh. Yazdanifard, R. A. Sadeghzadeh, and M. Ojaroudi, "Ultra-Wideband Small Square Monopole Antenna with Variable Frequency Band-Notch Function", Progress In Electromagnetics Research C, vol. 15, pp. 133-144, 2010.

[8] J. William, R. Nakkeeran, "A New UWB Slot Antenna with Rejection of WiMax and WLAN Bands," *Applied Computational Electromagnetics Society (ACES) Journal*, vol. 25, no. 9, pp. 787-793, September 2010.

[9] M. Ojaroudi, "Printed Monopole Antenna with a Novel Band-Notched Folded Trapezoid for Ultra-Wideband Applications", *Journal of Electromagnetic Waves and Application (JEMWA)*, vol. 23, pp. 2513-2522, 2009.

[10] M. Ojaroudi, Gh. Ghanbari, N. Ojaroudi, and Ch. Ghobadi, "Small Square Monopole Antenna for UWB Applications with Variable Frequency Band-Notch Function," *IEEE Antennas and Wireless Propagation Letters*, vol. 8, pp. 1061-1064, 2009.

[11] M. Rostamzade, S. Mohamadi, Ch. Ghobadi, J. Nourinia, and M. Ojaroudi, "Square Monopole Antenna for UWB Applications with Novel Rod-

Shaped Parasitic Structures and Novel V-Shaped Slots in the Ground Plane," *IEEE Antennas and Wireless Propagation Letters*, vol. 11, pp. 446-449, 2012.

[12] T. Dissanayake, and K. P. Esselle, "Prediction of the notch frequency of slot loaded printed UWB antennas," *IEEE Trans. Antennas and Propag.*, vol. 55, no. 11, pp. 3320-3325, 2007.

[13] Q. Wu, R. Jin, J. Geng, and J. Lao, "Ultra-wideband rectangular disk monopole antenna with notched ground," *Electron. Lett.*, vol. 43, no. 11, pp. 1100-1101, May 2007.

[14] J. P. Lee, S. O. Park, and S. K. Lee, "Bow-tie Wideband Monopole Antenna with the Novel Impedance-matching Technique," *Microw. Opt. Technol. Lett.*, vol. 33, no. 6, pp. 448-452, Jun. 2002.

[15] Ansoft High Frequency Structure Simulation (HFSS), Ver. 13, Ansoft Corporation, 2010.

Behrang Hadian Siahkal-Mahalle was born on 1981 in Siahkal, Iran. He received his B.Sc. degree in Electrical Engineering from University of Science and Technology, and M.Sc. degree in Telecommunication Engineering from Tarbiat Modarres University (T. B. U), Tehran, Iran. He has been a Research Fellow and a Teaching Assistant with the Department of Electrical Engineering, Aeronautical University of Science and Technology, Tehran, Iran. His research interests include microstrip antenna design, microwave component design, UWB systems.

Mohammad Ojaroudi was born on 1984 in Germi, Iran. He received his B.Sc. degree in Electrical Engineering from Azad University, Ardabil Branch and M.Sc. degree in Telecommunication Engineering from Urmia University. From 2010, he is working toward the Ph.D. degree at Shahid Beheshti University. From 2007 until now, he is an Teaching Assistant with the Department of Electrical Engineering, Islamic Azad University, Ardabil Branch, Iran. Since March 2008, he has been a Research Fellow (Chief Executive Officer) in the Microwave Technology Company (MWT), Tehran, Iran. His research interests include analysis and design of microstrip antennas, design and modeling of microwave structures, radar systems, and electromagnetic theory. He is author and coauthor of more than 70 journal and international conference papers.

Nasser Ojaroudi was born on 1986 in Germi, Iran. He received his B.Sc. degree in Electrical Engineering from Azad University, Ardabil Branch. From 2011, he is working toward the M.Sc. degree in Telecommunication Engineering at Shahid Rajaee Teacher Training University. Since March 2008, he has been a Research Fellow in the Microwave Technology Company (MWT), Tehran, Iran. His research interests include microstrip antennas for radar systems, ultra-wideband (UWB) and small antennas for wireless communications, microwave passive devices and circuits, and microwave/millimeter systems.

Compact Microstrip Branch-line Coupler with Wideband Harmonic Suppression

Haifei Cui[1], Jianpeng Wang[1] and Jia-Lin Li[2]

[1] Ministerial Key Laboratory of JGMT,
Nanjing University of Science and Technology, Nanjing 210094, China
E-mail: elehfc@gmail.com, elejpwang@yahoo.com.cn

[2] School of Physical Electronics,
University of Electronic Science and Technology of China, Chengdu 610054, China
E-mail: jialinuestc@hotmail.com

Abstract ─ one compact microstrip branch-line coupler with wideband harmonic suppression is presented in this letter. The new structure has two significant advantages, which not only effectively reduces the occupied area to 26.5% of the conventional branch-line coupler at 0.96 GHz, but also has high 6^{th} harmonic suppression performance. The measured results indicate that a bandwidth of more than 120 MHz has been achieved while the phase difference between S_{21} and S_{31} is within 90° ± 1°. The measured bandwidth of $|S_{21}|$ and $|S_{31}|$ within 3 ± 0.5 dB are 145 MHz and 150MHz, respectively. Furthermore, the measured insertion loss is comparable to that of a conventional branch-line coupler. The new coupler can be easily implemented by using the standard printed-circuit-board etching processes and is very useful for wireless communication systems.

Index Terms ─ Branch-line coupler, microstrip, harmonic suppression.

I. INTRODUCTION

Branch-line couplers are extensively used at microwave frequencies in the design of microwave circuits such as balanced mixers, image-rejection mixers, balanced amplifiers, power combiners, and power dividers, etc [1]. There are currently two drawbacks for the conventional microstrip branch-line design. Firstly, as the conventional branch-line coupler is composed of four quarter-wavelength transmission-line sections at the designed frequency, this will result in a large occupied area especially at low frequency. Secondly, the conventional design also has harmonics that occurred at the integral multiples of the fundamental operation frequency. These properties will degrade the performance of the coupler. Therefore, much work has been reported in recent years to achieve both compact design and harmonic suppression for the branch-line coupler [2-12].

Typically, there are two methods to design a compact planar microstrip branch-line coupler with harmonic suppression. The first method is to load the coupler with shunt open-stubs. By loading shunt open-stubs inside the free area of the branch-line coupler, Eccleston et al. designed a branch-line coupler with a size reduction of 37% to the conventional design at 1.8 GHz [5]. Based on the similar idea, Mondal et al. proposed a branch-line coupler, which has the properties of 42% size reduction at 2.4 GHz and 5^{th} harmonics suppression [6]. However, further improvement should be carried out on size reduction and

Submitted On: March 19, 2012
Accepted On: July 22, 2012

harmonic suppression. The second design method is to introduce slow-wave resonators in the coupler structure. Using compensated spiral compact microstrip resonant cells (SCMRCs), Gu et al. introduced a branch-line coupler with its area reduced to 24% of the conventional one together with 2nd and 3rd harmonics suppression at 2.4 GHz. However, the isolation performance is not ideal [7]. By introducing high-low impedance resonators inside the free area of the coupler, Wang et al. proposed a slow-wave branch-line coupler with its area reduced to 28% of the conventional one at 2.0 GHz. Even so, it only has 2nd harmonic suppression performance [8]. On the other side, size reduction methods were also reported in [9–12]. These couplers achieve compact size, but the harmonic suppressions still need improvement.

The motivation of this paper is to design a new microstrip branch-line coupler with compact size and wideband harmonic suppression. For this purpose, one branch-line coupler with operation central frequency located at 0.96 GHz is designed, fabricated, and measured. Measured results indicate that the proposed branch coupler not only effectively reduces the occupied area to 26.5% of the conventional branch-line coupler at the same operation frequency, but also has high 6th harmonic suppression performance. Furthermore, the proposed new coupler has a bandwidth of more than 120 MHz, while the phase difference between S21 and S31 is within 90° ± 1°. The organizations of the paper are as following: the design theory of the proposed branch-line coupler is given in Section II; the simulated and measured results are given in Section III, and the conclusions are given in Section IV.

II. CIRCUIT DESIGN

The schematic layout of the proposed branch-line coupler is shown in Fig. 1, which consists of eight microstrip open-ended resonators loaded inside the free area of a conventional branch-line coupler. Each microstrip resonator is composed of a short high-impedance line and a long low-impedance line with open-end. This type of loading will introduce eight microstrip open-ended resonators that are in parallel with the main transmission lines of the conventional coupler. As the length of the high-impedance line is very short and less than $\lambda/10$, where λ is the guided wavelength at the operation frequency. Therefore, each

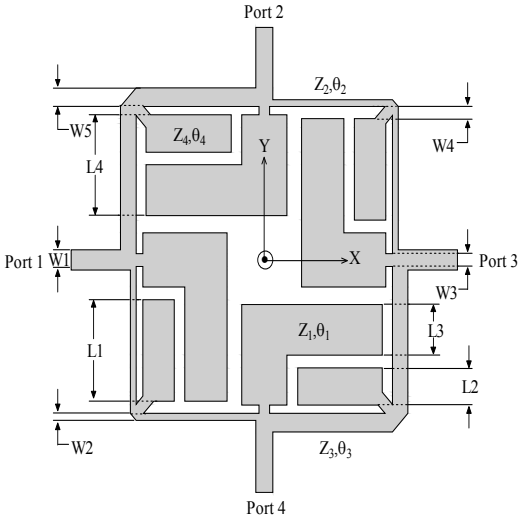

Fig. 1. Topology of the proposed branch-line coupler.

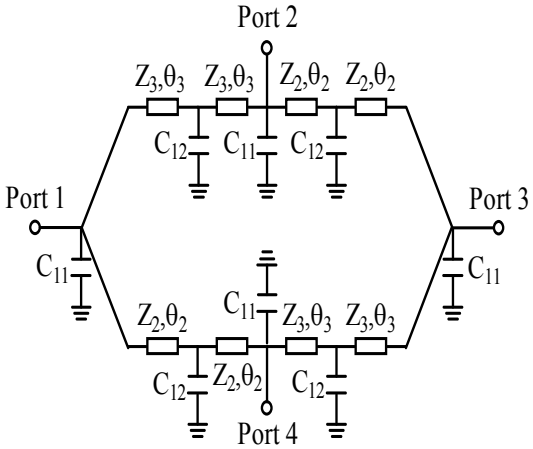

Fig. 2. Equivalent circuit of the proposed branch-line coupler.

high-impedance line can be deemed as a lumped element with negligibly small value and its inductance effect to the per unit length of the main transmission lines between two adjacent ports can be ignored since it is trivial. The capacitances caused by the low-impedance lines are loaded parallel with the main transmission lines in a distributed form. This will increase the per unit length capacitance of the main transmission lines between two adjacent ports. Figure 2 shows the equivalent circuit of the proposed branch-line

coupler. We can clearly see from this figure that the loaded high-low impedance resonators will introduce extra parallel capacitances denoted as C11 and C12 in the coupler, where C11 and C12 are the capacitances caused by the couplings between the loaded resonators and the ground. Thus, this type of loading can increase the shunt capacitance in the coupler. As the propagation constant β is given by

$$\beta = \omega\sqrt{L_0(C_0 + C_1)}\,, \qquad (1)$$

Where L0 and C0 are the distributed inductance and capacitance for the main line of the branch-line coupler per unit length, respectively, and C1 is the effective distributed capacitance per unit length caused by the shunt capacitance C11 and C12. Clearly, the propagation constant is increased by the periodic capacitive loading. An increased propagation constant means a shorter physical structure can be used to yield a required electrical length compared with a conventional transmission line. This new type of slow-wave loading dose not occupy extra area of the circuit as the periodic slow-wave loading are placed at the free area inside the branch-line coupler. We can get a desired slow-wave factor by adjusting the structure parameters of the proposed new branch-line coupler properly. On the other side, when the electrical length of the loaded high-low impedance resonator is odd number times of λ/4, where λ is the guided wavelength at the spurious resonance frequency, harmonic signals that occurred at the integral multiples of the fundamental operation frequency can be suppressed. The proposed branch-line coupler is designed based on the slow-wave loading mentioned above. The values of L0, C0, and C1 can be achieved by the curve fitting method through Advanced Design System simulator (ADS) based on the proposed lumped element equivalent circuit. Then, the coarse value of the structure parameters can be achieved by the experimental equations given in [13]. With further optimal design by the full-wave electronic magnetic (EM) simulation software (ANSOFT HFSS version 11.0), the final structure parameters of the proposed branch-line coupler are as follows: W1 = 1.7 mm, W2 =0.6 mm, W3 = 1.1 mm, W4 = 0.7 mm, W5 = 1.6 mm, L1 = 9 mm, L2 = 3.2 mm, L3 = 4.6 mm, L4 = 8.5 mm. They can be easily implemented by the standard printed-circuit-board etching processes. The substrate used here has a relative dielectric constant of 2.94 and a thickness of 0.76 mm and the total area of the proposed branch-line coupler is 820.25 mm2.

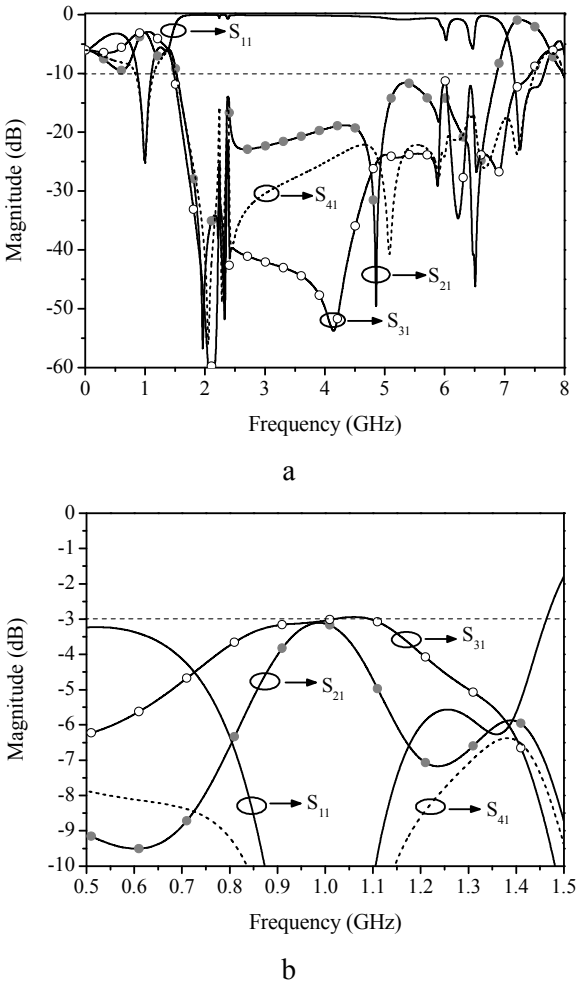

Fig. 3. Simulated S-parameters of the proposed branch-line coupler.

a Frequency range of 0 to 8 GHz.

b Frequency range of 0.5 to 1.5 GHz.

III. SIMULATION AND MEASUREMENT RESULTS

Simulation was accomplished with ANSOFT HFSS. Measurement was carried out on an Agilent 8510C network analyzer. Figure 3 shows the simulated results of S-parameters. Figure 4 shows the measured S-parameters of the proposed

branch-line coupler. We can find that they are in good agreement. Referring to the measured results in Fig. 4, the central frequency located at 0.96 GHz can be clearly observed. At this central frequency, the measured S21 is 3.12 dB and S31 is 3.10 dB, while the measured bandwidth of |S21| and |S31| within 3 ± 0.5 dB are 145 MHz and 150MHz, respectively.

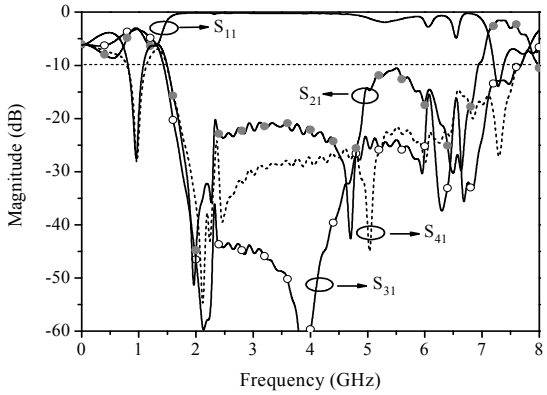

a

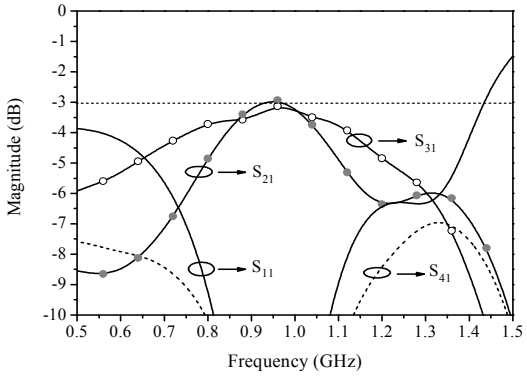

b

Fig. 4. Measured S-parameters of the proposed branch-line coupler.

a Frequency range of 0 to 8 GHz.

b Frequency range of 0.5 to 1.5 GHz.

From Fig. 4a we can also observe that the 6th harmonic signals have been effectively suppressed with S21 and S31 lower than a criterion of -10 dB. This means the proposed new coupler can protect specialized communication system from the interference of the unwanted signals from 1.5 GHz to 5.8 GHz, such as the signals in the IEEE 802.11 a/b/g standard specifications. This property is very useful for modern communication system to operation in high performance. In order to study the size reduction performance, we investigated the circuit area of conventional one at the same frequency and found that the cost area is 3089.88 mm2. This means that the proposed branch-line coupler can effectively reduce the occupied area to 26.5% of the conventional coupler.

Figure 5 shows the phase difference between S21 and S31. According to a criterion of ±1°around the optimum 90° phase difference, the frequency range is from 0.90 GHz to 1.02 GHz corresponding to a bandwidth is 12.5%. To demonstrate the superior performance of the proposed coupler, Table 1 shows the performance comparison of the proposed design with several previous designs. Hence, the advantages of the proposed coupler can be clearly observed. Photograph of the fabricated branch-line coupler is shown in Fig. 6.

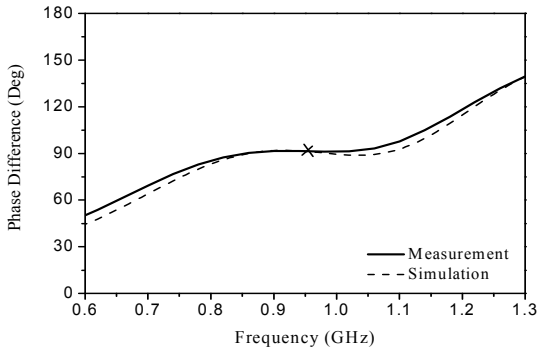

Fig. 5. Phase difference between S_{21} and S_{31}.

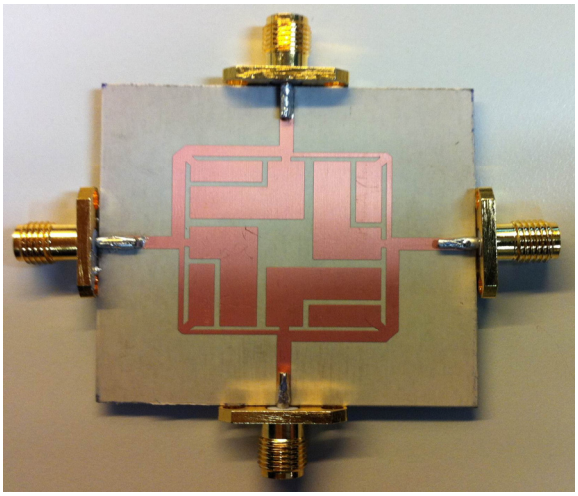

Fig. 6. Proposed branch-line coupler.

Table 1: Performance comparison of couplers

	Relative Area	**Harmonic Suppression**
Conventional	100%	No
[5]	63%	Not Reported
[6]	58%	5th
[7]	24%	3rd
[8]	28%	2nd
[9]	29.33%	4th
[10]	26.8%	2nd
[11]	25%	4th
This Work	26.5%	6th

IV. CONCLUSION

A novel compact microstrip branch-line coupler has been presented in this letter. Due to eight microstrip open-ended resonators placed inside the free area of a conventional branch-line coupler, the new structure has effectively reduced the occupied area to 26.5% of the conventional design at 0.96 GHz and has high 6th harmonic suppression performance. One sample microstrip branch-line coupler has been fabricated, measured, and compared with the previous designs. Results indicate that the proposed coupler has the properties of compact size, low insertion loss, and wideband harmonic suppression performance. With this good performance, the proposed branch-line coupler has potential applications in modern wireless communication systems.

ACKNOWLEDGEMENT

This work was supported by the Natural Science Foundation of China (NSFC) under Grant No. 61101047, the Specialized Research Fund for the Doctoral Program by the Ministry of Education of China under Grant No. 20113219120015, and by the Zijin Foundation of Nanjing University of Science and Technology under Grant No. AB41372.

REFERENCES

[1] D. M. Pozar, Microwave Engineering, 3rd ed. New York: Wiley, Ch. 7, pp. 333-337, 2005.

[2] A. Mohra, A. F. Sheta, S. F. Mahmoud, "New Compact 3 dB 0/180 Microstrip Coupler Configurations," *Applied Computational Electromagnetics Society (ACES) Journal*, vol. 19, no. 2, pp. 108-112, July 2004.

[3] B. Xiao, J. Hong, B. Wang, "A Novel UWB Out-of-phase Four-way Power Divider," *Applied Computational Electromagnetics Society (ACES) Journal*, vol. 26, no. 10, pp. 863-867, Oct. 2011.

[4] K. A. Shamaileh, A. Qaroot, N. Dib, A. Sheta, "Design of Miniaturized Unequal Split Wilkinson Power Divider with Harmonics Suppression using Non-uniform Transmission Lines," *Applied Computational Electromagnetics Society (ACES) Journal,* vol. 26, no. 6, pp. 530–538, June. 2011.

[5] K. W. Eccleston and S. H. M. Ong, "Compact Planar Microstripline Branch-line and Rat-race Couplers," *IEEE Trans. Microw. Theory Tech.*, vol. 51, no. 10, pp. 2119-2125, Oct. 2003.

[6] P. Mondal, and A. Chakrabarty, "Design of Miniaturized Branch-line and Rat-race Hybrid Couplers with Harmonics Suppression," *IET Microw. Antennas Propag.*, vol. 3, no. 1, pp. 109-116, Jan. 2009.

[7] J. Gu, and X. Sun, "Miniaturization and Harmonic Suppression of Branch-line and Rat-race Hybrid Coupler using Compensating Spiral Compact Micostrip Resonant Cell," *IEEE MTT-S Int. Dig.*, pp. 1211-1214, 2005.

[8] J. Wang, B.-Z. Wang, Y.-X. Guo, L. C. Ong, and S. Xiao, "A Compact Slow-wave Microstrip Branch-line Coupler with High Performance," *IEEE Microw. Wirel. Compon. Lett.*, vol. 17, no. 7, pp. 501-503, Jul. 2007.

[9] V. K. Velidi, B. Patel, S. Sanval, "Harmonic Suppressed Compact Wideband Branch-line Coupler using Unequal Length Open-stub Units," *International Journal of RF and Microwave Computer-Aided Engineering.*, vol. 21, no. 1, pp. 115-119, Jan. 2011.

[10] K. Y. Tsai, H. S. Yang, J. H. Chen, and Y. J. E. Chen, "A Miniaturized 3 dB Branch-line Hybrid Coupler with Harmonics Suppression," *IEEE Microw. Wirel. Compon. Lett.*, vol. 21, no. 10, pp. 537-539, Oct. 2011.

[11] V. K. Velidi, A. Pal, S. Sanyal, "Harmonics and Size Reduced Microstrip Branch-line Baluns using Shunt Open-stubs," *International Journal of RF and Microwave Computer-Aided Engineering.*, vol. 21, no. 2, pp. 115-119, Mar. 2011.

[12] A. S. Al-Zayed, Z. M. Hehjazi, A. S. Mohra, "A Microstrip Directional Coupler with Tight Coupling and Relatively Wideband using Defected Ground Structure," *Applied Computational Electromagnetics Society (ACES) Journal*, vol. 25, no. 10, pp. 577-587, Oct. 2010.

[13] J. S. Hong and M. J. Lancaster, Microstrip Filters for RF/Microwave Applications. New York: Wiley, Ch. 4, 2001.

Haifei Cui received the B.S. degree in electronics and information engineering from Anhui University, Hefei, China, in 2008. He is currently working toward the Ph.D. degree in Electromagnetic Field and Microwave Technology in NJUST. His research interest is the design of miniaturized high performance microwave passive device.

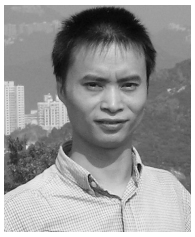

Jia-Lin Li received the M. Sc. degree from UESTC, Chengdu, China, in 2004, and the Ph. D. degree from the City University of Hong Kong, Hong Kong, in 2009, both in electronic engineering. Since Sept. 2009, he has been with the Institute of Applied Physics, School of Physical Electronics, UESTC, where he is currently a Professor. His research interests include the high performance active/passive microwave/millimeter-wave antennas, circuits and systems realized on PCB, multilayer PCB, LTCC, etc.

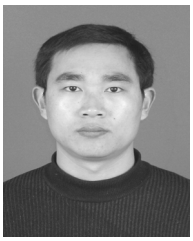

Jianpeng Wang received the M. Sc. and Ph. D. degree from UESTC, Chengdu, China, in 2004, and 2007, respectively, both in electronic engineering. Since Jan. 2008, he has been with the Ministerial Key Laboratory of JGMT, School of Electronic and Optical Engineering, NJUST, where he is currently an Associate Professor. His research interests include the high performance microwave/millimeter-wave passive components, circuits and systems realized on PCB, LTCC, etc.

Small Slot Antenna with Enhanced Bandwidth and Band-Notched Performance for UWB Applications

M. T. Partovi [1], N. Ojaroudi [2], and M. Ojaroudi [3]

[1] Department of Electrical Engineering,
Aeronautical University of Science and Technology, Tehran, Iran.
partovimt@gmail.com

[2] Faculty of Electrical & Computer Engineering
Shahid Rajaee Teacher Training University, Tehran, Iran
n_ojaroudi@srttu.edu

[3] Young Research Group
Ardabil Branch, Islamic Azad University, Ardabil, Iran
m.ojaroudi@iauardabil.ac.ir

Abstract ─ A novel ultra wideband (UWB) printed slot antenna with band-notched performance is designed and manufactured. In order to increase the impedance bandwidth of the slot antenna, we use a rectangular slot with a pair of L-shaped strips protruded inside the slot on the ground plane that with this structure UWB frequency range can be achieved. Additionally, by using an N-shaped slot on the radiating stub, a frequency notch band performance has been obtained. The designed antenna has a small size of 20×20 mm^2 while showing the radiation performance in the frequency band of 3.12 to over 14.27 GHz with a band rejection performance in the frequency band of 5.03 to 5.86 GHz. Simulated and experimental results obtained for this antenna show that it exhibits good radiation behavior within the UWB frequency range.

Index Terms ─ Printed Slot Antenna, N-Shaped Slot, Protruded L-Shaped Strip, Ultra-Wideband (UWB).

I. INTRODUCTION

In UWB communication systems, one of key issues is the design of a compact antenna while providing wideband characteristic over the whole operating band. Consequently, a number of printed microstrip with different geometries have been experimentally characterized [1]-[3]. Moreover, other strategies to improve the impedance bandwidth have been investigated [4]-[5]. The Federal Communication Commission (FCC)'s allocation of the frequency range 3.1–10.6 GHz for UWB systems and it will cause interference to the existing wireless communication systems, such as, the wireless local area network (WLAN) for operating in 5.15–5.35 GHz and 5.725–5.825 GHz bands), so the UWB antenna with a single band-stop performance is required [6-8].

A novel and compact microstrip.fed slot antenna with additional resonance and band-notched characteristics for UWB applications has been presented. This paper focuses on a slot antenna for UWB applications, which combines the square radiating stub approach with an N-shaped slot, and the ground plane with a rectangular slot with a pair of L-shaped strips protruded inside the slot that achieves a fractional bandwidth of more than 125%. In the proposed structure, first by inserting a rectangular slot with a pair of L-shaped strips protruded inside the slot on the ground plane, additional resonance is excited and hence much wider impedance bandwidth can be produced, especially at the higher frequencies. In order to generate a single band-notch function, for the first

Submitted On: Feb. 13, 2012
Accepted On: Aug. 5, 2012

time, we use an N-shaped slot on the square radiating stub. Good return loss and radiation pattern characteristics are obtained in the frequency band of interest. Simulated and experimental results show that the proposed slot antenna could be a good candidate for UWB applications

II. ANTENNA DESIGN

The slot antenna fed by a 50 Ω microstrip line is shown in Fig 1, which is printed on a FR4 substrate of thickness 0.8 mm, permittivity 4.4, and loss tangent 0.018. The basic antenna structure consists of a square radiating stub, a 50 Ω microstrip feed-line, and a ground plane with a rectangular slot. The square radiating stub has a width W. The radiating stub is connected to a feed line of width W_f and length L_f, as shown in Fig. 1. On the other side of the substrate, a conducting ground plane with a rectangular slot is placed. The proposed antenna is connected to a 50 Ω SMA connector for signal transmission

In this study, to design a novel antenna, the antenna with N-shaped slot and a rectangular slot with a pair of L-shaped strips protruded inside the slot is proposed. Based on Electromagnet Coupling Theory (ECT), the L-shaped strips protruded inside the slot on the ground plane are playing an important role in the broadband characteristics of this antenna, because it can adjust the electromagnetic coupling effects between the feed-line and the ground plane, and improves its impedance bandwidth without any cost of size or expense [9]. This phenomenon occurs because, with the use of L-shaped strips protruded inside the slot, additional coupling is introduced between the feed of the square patch and the ground plane [10]. As illustrated in Fig. 1, the N-shaped slot is cut on the square radiating stub. The N-shaped slot perturbs the resonant response and also acts as a half-wave resonant structure [11]. At the notch frequency, the current flows are more dominant around the N-shaped slot [5]-[7]. As a result, the desired high attenuation near the notch frequency can be produced. The variable band-notch characteristics can be achieved by carefully choosing the parameter (W_n, and L_n) for the N-shaped slot. In this structure, the width, W_n, is the critical parameter to control the filter bandwidth. On the other hand, the center frequency of the notched band is insensitive to the change of W_n. The resonant frequency of the notched band is determined by L_n. In this design, the optimized length is set to band-stop resonate at approximately, where and corresponds to band-notch frequency (5.5 GHz), and also is fixed at 5. 5 mm.

In this work, we start by choosing the aperture length L_S. We have a lot of flexibility in choosing this parameter. The length of the aperture mostly affects the antenna bandwidth. As L_S decreases, so does the antenna BW and vice versa. Next step, we have to determine the aperture width W_S. The aperture width is approximately $\lambda_S/2$, where λ_S is the slot wavelength that depends on a number of parameters such as the slot width as well as the thickness and dielectric constant of the substrate on which the slot is fabricated. The last and final step in the design is to choose the length of the radiating patch W_P. A good starting point is to choose it to be equal to $W = \lambda_m/4$, where λ_m is the guided wavelength in the microstrip line [6].

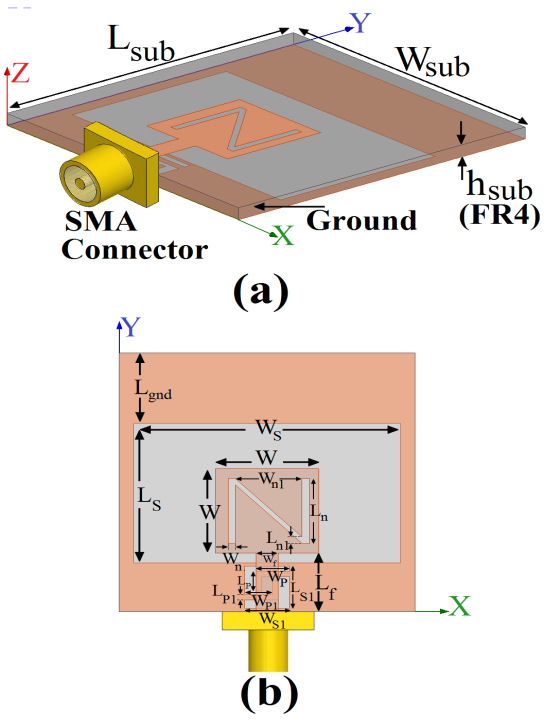

Fig. 1. Geometry of the proposed slot antenna, (a) side view, and (b) top view.

The optimal dimensions of the designed antenna are as follows: $W_{sub} = 20mm$, $L_{sub} = 20mm$, $W = 7mm$, $W_f = 1.5mm$, $L_f = 4mm$, $W_S = 18mm$, $L_S = 11mm$, $W_n = 0.3mm$, $L_n = 6mm$, $W_{n1} = 3.5mm$, $L_{n1} = 0.4mm$, $W_{S1} = 2.5mm$, $L_{S1} = 2.5mm$, $W_P = 2mm$, $L_P = 1mm$, $W_{P1} = 1.75mm$, $L_{P1} = 0.25mm$, and $L_{gnd} = 3mm$.

III. RESULTS AND DISCUSSIONS

In this Section, the planar slot antenna with various design parameters were constructed, and the numerical and experimental results of the input impedance and radiation characteristics are presented and discussed. The parameters of this proposed antenna are studied by changing one parameter at a time and fixing the others. The simulated results are obtained using the Ansoft simulation software high-frequency structure simulator (HFSS) [12].

Figure 2 shows the structure of the various antennas used for simulation studies. Return loss characteristics for ordinary slot antenna (Fig. 2(a)), with a rectangular slot with a pair of L-shaped strips protruded inside the slot on the ground plane (Fig. 2(b)), and the proposed antenna structure (Fig. 2(c)) are compared in Fig. 3. It is found that by inserting the a rectangular slot with a pair of L-shaped strips protruded inside the slot on the ground plane, the antenna can create the third resonant frequency at 10.5 GHz based on an over-coupling condition and hence the impedance bandwidth is effectively improved at the upper frequency [4]. Also as shown in Fig. 3, in this structure, the N-shaped slot is used in order to generate the frequency band-stop performance. Also the input impedance of the various slot antenna structures that shown in Fig. 2(b) and 2(c), on a Smith Chart is shown in Fig. 4.

In order to understand the phenomenon behind these new additional resonances and band-notch performance, the simulated current distribution on the ground plane and the radiating patch for the proposed antenna at the resonances frequencies of 4 GHz, 9 GHz, and 10.5 GHz and the notch frequency of 5.5 GHz are presented in Figs. 5(a), 5(b), 5(c) and 5(d), respectively.

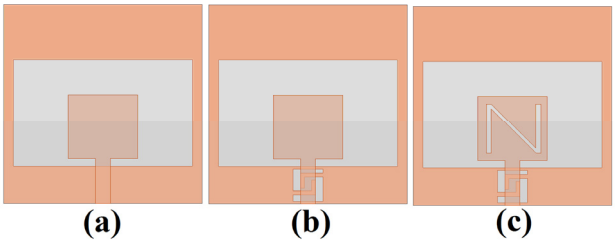

Fig. 2. (a) The ordinary slot antenna, (b) the antenna with a rectangular slot with a pair of L-shaped strips protruded inside the slot on the ground plane (c) the proposed slot antenna.

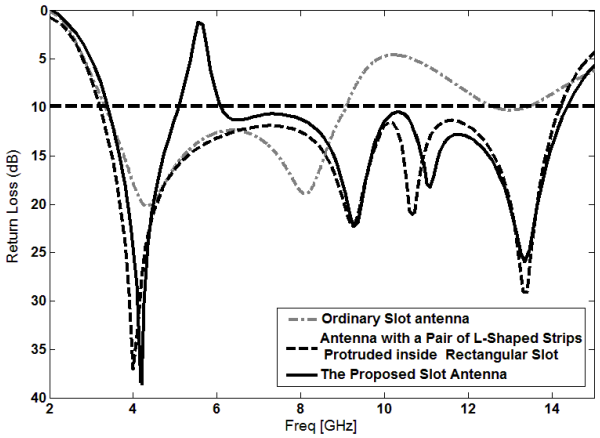

Fig. 3. Simulated return loss characteristics for antennas shown in Fig. 2.

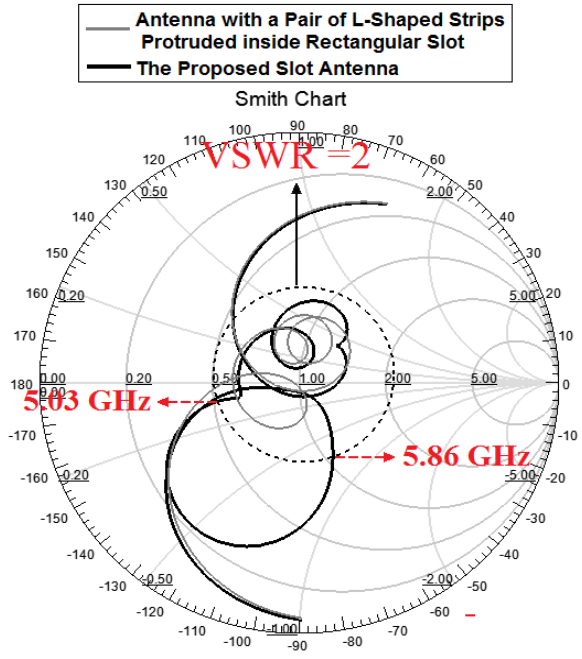

Fig. 4. The simulated input impedance on a Smith chart of the various slot antenna structures shown in Fig. 2(b) and 2(c).

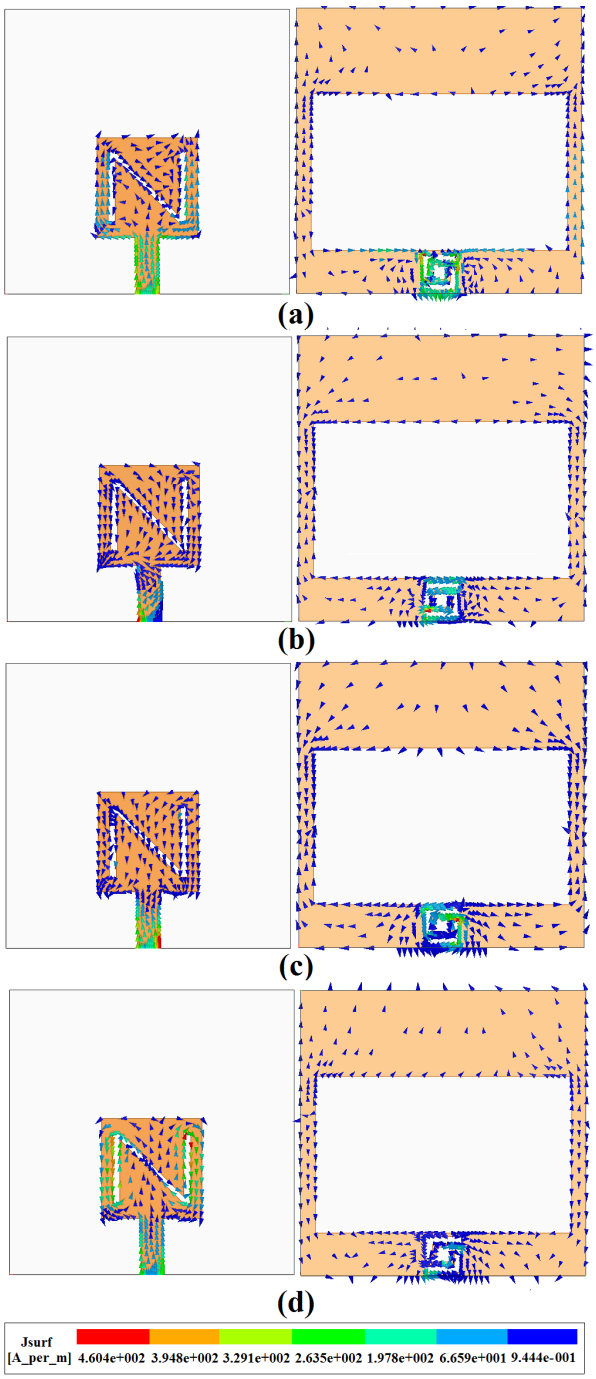

Fig. 5. Simulated surface current distributions for the proposed antenna on the radiating patch and the ground plane at resonances frequencies, (a) 4 GHz, (b) 9 GHz, (c) 10.5 GHz, and (d) at notch frequency (5.5 GHz).

It can be observed on Figs. 5(a), 5(b), and 5(c) that the current concentrated on the edges of the interior and exterior of the protruded L-shaped strips and the feed-line and radiating patch edges at resonances frequencies. Therefore the antenna impedance changes at these frequencies due to the resonant properties of the proposed structure. In addition, by inserting a rectangular slot with a pair of L-shaped strips protruded inside the slot on the ground plane the impedance bandwidth is effectively improved at the upper frequency [2]. It can be observed on Fig. 5(d) that the current concentrated on the edges of the interior and exterior of the N-shaped slot at 5.5 GHz. This figure shows that the electrical current for the notch frequency (5.5 GHz) does change direction along the N-shaped slot, due to the band notch properties of the proposed structure.

In this study, the N-shaped slot in the square radiating stub with variable dimensions is used in order to generate the frequency band-stop performance as displayed in Fig. 1. The simulated VSWR curves with different values of L_n are plotted in Fig. 6. As shown in Fig. 6, when the interior length increases from 4.8 to 6.6 mm, the center of notch frequency is decreases from 5.95 to 4.35 GHz. From these results, we can conclude that the notch frequency is controllable by changing the interior length of N-shaped slot.

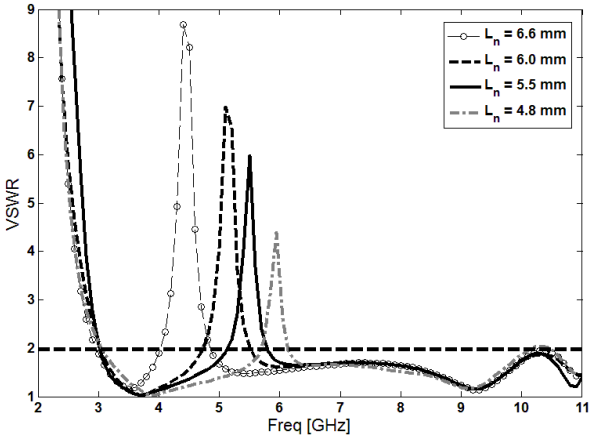

Fig. 6. Simulated VSWR characteristic with different values of L_n.

Another main effect of the N-shaped slot occurs on the filter bandwidth. In this structure, the width W_n, is the critical parameter to control the filter bandwidth. Figure 7 illustrates the simulated VSWR characteristics with various width of W_n. As the interior gap distance of the W_n increases from 0.2 to 0.6 mm, the filter bandwidth is varied

from 0.7 to 1.5 GHz. Therefore the bandwidth of notch frequency is controllable by changing the width of W_n.

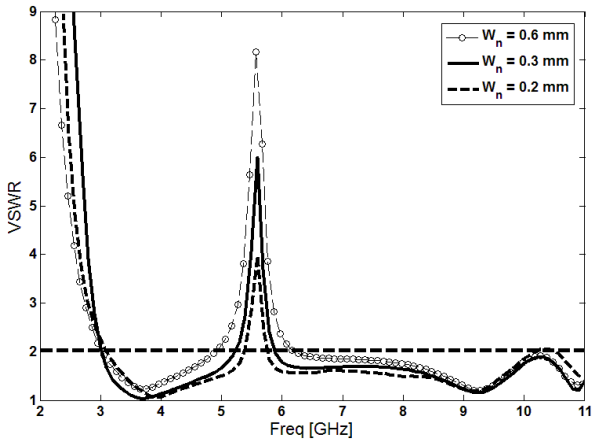

Fig. 7. Simulated VSWR characteristic with different values of W_n.

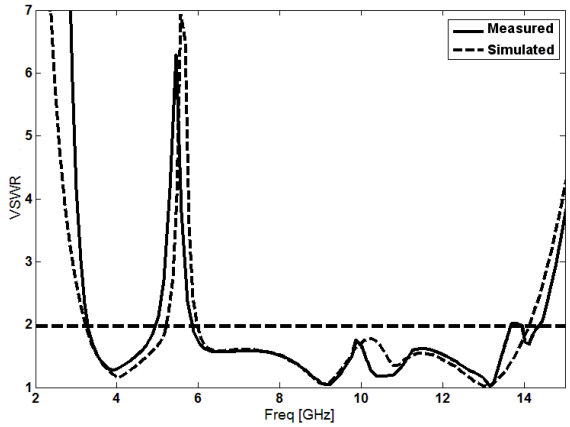

Fig. 8. Measured and simulated VSWR for the proposed slot antenna.

The proposed antenna with optimal design was built and tested. Figure 8 shows the measured and simulated VSWR characteristics of the proposed antenna. The fabricated antenna satisfies the VSWR<2 requirement from of 3.12 to over 14.27 GHz with a band rejection performance in the frequency band of 5.03 to 5.86 GHz. As shown in Fig. 8, there exists a discrepancy between measured data and the simulated results this could be due to the effect of the SMA port. In order to confirm the accurate VSWR characteristics for the designed antenna, it is recommended that the manufacturing and measurement process need to be performed carefully.

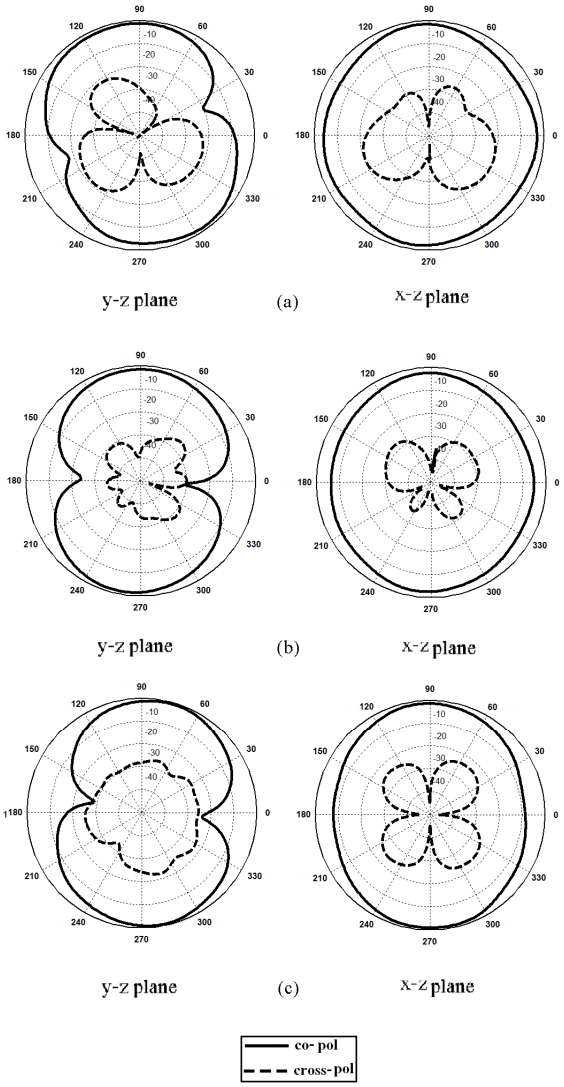

Fig. 9. Measured radiation patterns of the proposed antenna. (a) 4 GHz, (b) 7 GHz, and (c) 10 GHz.

Fig. 9 the measured radiation patterns including the co-polarization and cross-polarization in the *H*-plane (*x*-*z* plane) and *E*-plane (*y*-*z* plane). The main purpose of the radiation patterns is to demonstrate that the antenna actually radiates over a wide frequency band. It can be seen that the radiation patterns in *x*-*z* plane are nearly omnidirectional for the three frequencies.

Figure 10 shows the effects of the a rectangular slot with a pair of L-shaped strips protruded inside the slot on the ground plane and the N-shaped slot on the radiating stub on the maximum gain in comparison to the ordinary slot antenna without

them. A two-antenna technique is used to measure the radiation gain in the z axis direction (x-z plane). As shown in Fig. 10, the ordinary antenna has a gain that is low at 2 GHz and increases with frequency. It is found that the gain of the ordinary slot antenna is decreased with the use of the rectangular slot with a pair of L-shaped strips protruded inside the slot on the ground plane and the N-shaped slot on the radiating stub. It can be observed in Fig. 10 that by using these structures, a sharp decrease of maximum gain in the notched frequency band at 5.5 GHz are shown. For other frequencies outside the notched frequencies band, the antenna gain with the filter is similar to those without it.

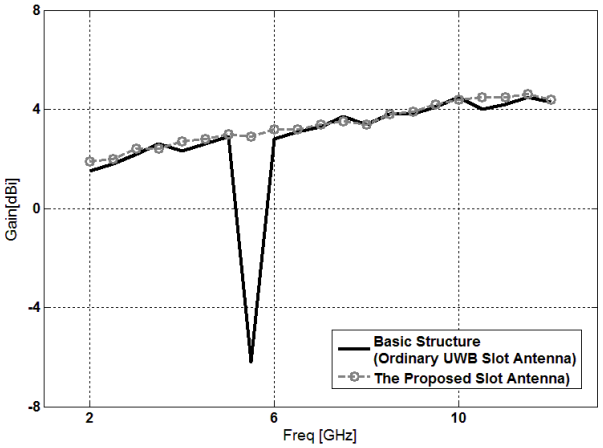

Fig. 10. Maximum gain comparisons for the ordinary slot antenna (simulated), and the proposed antenna (measured) in the z axis direction (x-z plane).

V. CONCLUSION

In this letter, a novel compact printed slot antenna has been proposed for UWB applications. The fabricated antenna satisfies the VSWR<2 requirement from of 3.12 to over 14.27 GHz with a band rejection performance in the frequency band of 5.03 to 5.86 GHz. By inserting a rectangular slot with a pair of L-shaped strips protruded inside the slot on the ground plane, additional resonance is excited and hence much wider impedance bandwidth can be produced, especially at the higher band. n order to generate a single band-notch function, for the first time, we use an N-shaped slot on the square radiating stub. The proposed antenna has a simple configuration and is easy to fabricate. Experimental results show that the proposed antenna could be a good candidate for UWB application.

ACKNOWLEDGMENT

The authors are thankful to Microwave Technology (MWT) Company staff for their beneficial and professional help (www.microwave-technology.com).

REFERENCES

[1] D. Cheng, Compact Ultra Wideband Microstrip Resonating Antenna, US patent 7872606, Jan. 2011.

[2] Y. Tan, X.-J. Tian, and C.-F. Chen, "C-Shaped Slot Serves UWB Antenna", *Microwave & RF*, vol. 51, no. 2, pp. 89-91, Feb. 2012.

[3] R. Azim, M. T. Islam, N. Misran, "Design of a Planar UWB Antenna with New Band Enhancement Technique," *Applied Computational Electromagnetics Society (ACES) Journal*, vol. 26, no. 10, pp. 856-862, October 2011.

[4] D. S. Javan, O. H. Ghouchani, "Cross Slot Antenna with U-Shaped Tuning Stub for Ultra Wideband Applications," *Applied Computational Electromagnetics Society (ACES) Journal*, vol. 24, no. 4, pp. 427-432, August 2009.

[5] M. Ojaroudi, and A. Faramarzi, "Multi-Resonance Small Square Slot Antenna for Ultra-Wideband Applications," *Microwave and Optical. Tech. Letters*, vol. 53, no. 9, pp. 2145-2149, September 2011.

[6] M. Ojaroudi, S. Yzdanifard, N. Ojaroudi, and R.A. Sadeghzadeh, Band-notched Small Square-ring Antenna with a Pair of T-shaped Strips Protruded Inside the Square Ring for UWB Applications, *IEEE Antennas Wireless Propag. Lett.*, vol. 10, pp. 227-230, 2011.

[7] J. William, R. Nakkeeran, "A New UWB Slot Antenna with Rejection of WiMax and WLAN Bands," *Applied Computational Electromagnetics Society (ACES) Journal*, vol. 25, no. 9, pp. 787-793, September 2010.

[8] M. Naghshvarian-Jahromi, N. Komjani-Barchloui, "Analysis of the Behavior of Sierpinski Carpet Monopole Antenna," *Applied Computational Electromagnetics Society (ACES) Journal*, vol. 24, no. 1, pp. 32-36, February 2009.

[9] W. J. Lui, C. H. Cheng, Y. Cheng, et al., Frequency Notched Ultra Wideband Microstrip

Slot Antenna with a Fractal Tuning Stub, *Electron. Lett.,* vol. 41, pp. 294-296, 2005.

[10] J. Ding, Z. Lin, Z. Ying, and S. He, "A Compact Ultra-wideband Slot Antenna with Multiple Notch Frequency Bands", *Microw. Opt. Technol. Lett.,* vol. 49, no. 12, pp. 3056-3060, Dec. 2007.

[11] M.-C. Tang, S. Xiao, T. Deng, D. Wang, J. Guan, and B.-Z Wang, G. Ge, "Compact UWB Antenna with Multiple Band-notches for WiMAX and WLAN," *IEEE Trans. Antennas Propag.,* vol. 59, no. 4, pp.1372-1376, Apr. 2011.

[12] S.-W. Su, K.-L. Wong, and F.-S. Chang, Compact Printed Ultra Wideband Slot Antenna with a Band Notched Operation, *Microwave Opt. Technol. Lett.,* vol. 45, pp. 128-130, 2005.

[13] Ansoft High Frequency Structure Simulation (HFSS), Ver. 13, Ansoft Corporation, 2010.

Mohammad-Taghi Partovi was born on 1973 in Mianeh Iran. He received his B.Sc. degree in Control Engineering from University of Science and Technology, and M.Sc. degree in Industrial Engineering from University of Science and Technology, Mazandaran, Iran. Since March 2001, he has been a Research Fellow and a Teaching Assistant with the Department of Electrical Engineering, Aeronautical University of Science and Technology, Tehran, Iran. His research interests include design and modeling of microwave structures, radar systems, and RFID systems.

Nasser Ojaroudi was born on 1986 in Germi, Iran. He received his B.Sc. degree in Electrical Engineering from Azad University, Ardabil Branch. From 2011, he is working toward the M.Sc. degree in Telecommunication Engineering at Shahid Rajaee Teacher Training University. Since March 2008, he has been a Research Fellow in the Microwave Technology Company (MWT), Tehran, Iran. His research interests include microstrip antennas for radar systems, ultra-wideband (UWB) and small antennas for wireless communications, microwave passive devices and circuits, and microwave/millimeter systems.

Mohammad Ojaroudi was born on 1984 in Germi, Iran. He received his B.Sc. degree in Electrical Engineering from Azad University, Ardabil Branch and M.Sc. degree in Telecommunication Engineering from Urmia University. From 2010, he is working toward the Ph.D. degree at Shahid Beheshti University. From 2007 until now, he is a Teaching Assistant with the Department of Electrical Engineering, Islamic Azad University, Ardabil Branch, Iran. Since March 2008, he has been a Research Fellow (Chief Executive Officer) in the Microwave Technology Company (MWT), Tehran, Iran. His research interests include analysis and design of microstrip antennas, design and modeling of microwave structures, radar systems, and electromagnetic theory. He is author and coauthor of more than 70 journal and international conference papers.

2012 INSTITUTIONAL MEMBERS

DTIC-OCP LIBRARY
8725 John J. Kingman Rd, Ste 0944
Fort Belvoir, VA 22060-6218

AUSTRALIAN DEFENCE LIBRARY
Northcott Drive
Canberra, A.C.T. 2600 Australia

BEIJING BOOK CO, INC
701 E Linden Avenue
Linden, NJ 07036-2495

DARTMOUTH COLLEGE
6025 Baker/Berry Library
Hanover, NH 03755-3560

DSTO EDINBURGH
AU/33851-AP, PO Box 830470
Birmingham, AL 35283

SIMEON J. EARL – BAE SYSTEMS
W432A, Warton Aerodome
Preston, Lancs., UK PR4 1AX

ENGINEERING INFORMATION, INC
PO Box 543
Amsterdam, Netherlands 1000 Am

ETSE TELECOMUNICACION
Biblioteca, Campus Lagoas
Vigo, 36200 Spain

GA INSTITUTE OF TECHNOLOGY
EBS-Lib Mail code 0900
74 Cherry Street
Atlanta, GA 30332

TIMOTHY HOLZHEIMER
Raytheon
PO Box 1044
Rockwall, TX 75087

HRL LABS, RESEARCH LIBRARY
3011 Malibu Canyon
Malibu, CA 90265

IEE INSPEC
Michael Faraday House
6 Hills Way
Stevenage, Herts UK SG1 2AY

INSTITUTE FOR SCIENTIFIC INFO.
Publication Processing Dept.
3501 Market St.
Philadelphia, PA 19104-3302

LIBRARY – DRDC OTTAWA
3701 Carling Avenue
Ottawa, Ontario, Canada K1A OZ4

LIBRARY of CONGRESS
Reg. Of Copyrights
Attn: 407 Deposits
Washington DC, 20559

LINDA HALL LIBRARY
5109 Cherry Street
Kansas City, MO 64110-2498

MISSOURI S&T
400 W 14th Street
Rolla, MO 56409

MIT LINCOLN LABORATORY
Periodicals Library
244 Wood Street
Lexington, MA 02420

NATIONAL CHI NAN UNIVERSITY
Lily Journal & Book Co, Ltd
20920 Glenbrook Drive
Walnut, CA 91789-3809

JOHN NORGARD
UCCS
20340 Pine Shadow Drive
Colorado Springs, CO 80908

OSAMA MOHAMMED
Florida International University
10555 W Flagler Street
Miami, FL 33174

NAVAL POSTGRADUATE SCHOOL
Attn:J. Rozdal/411 Dyer Rd./ Rm 111
Monterey, CA 93943-5101

NDL KAGAKU
C/0 KWE-ACCESS
PO Box 300613 (JFK A/P)
Jamaica, NY 11430-0613

OVIEDO LIBRARY
PO BOX 830679
Birmingham, AL 35283

DAVID PAULSEN
E3Compliance
1523 North Joe Wilson Road
Cedr Hill, TX 75104-1437

PENN STATE UNIVERSITY
126 Paterno Library
University Park, PA 16802-1808

DAVID J. PINION
1122 E Pike Street #1217
SEATTLE, WA 98122

KATHERINE SIAKAVARA
Gymnasiou 8
Thessaloniki, Greece 55236

SWETS INFORMATION SERVICES
160 Ninth Avenue, Suite A
Runnemede, NJ 08078

YUTAKA TANGE
Maizuru Natl College of Technology
234 Shiroya
Maizuru, Kyoto, Japan 625-8511

TIB & UNIV. BIB. HANNOVER
DE/5100/G1/0001
Welfengarten 1B
Hannover, Germany 30167

UEKAE
PO Box 830470
Birmingham, AL 35283

UNIV OF CENTRAL FLORIDA
4000 Central Florida Boulevard
Orlando, FL 32816-8005

UNIVERSITY OF COLORADO
1720 Pleasant Street, 184 UCB
Boulder, CO 80309-0184

UNIVERSITY OF KANSAS – WATSON
1425 Jayhawk Blvd 210S
Lawrence, KS 66045-7594

UNIVERSITY OF MISSISSIPPI
JD Williams Library
University, MS 38677-1848

UNIVERSITY LIBRARY/HKUST
Clear Water Bay Road
Kowloon, Honk Kong

CHUAN CHENG WANG
8F, No. 31, Lane 546
MingCheng 2nd Road, Zuoying Dist
Kaoshiung City, Taiwan 813

THOMAS WEILAND
TU Darmstadt
Schlossgartenstrasse 8
Darmstadt, Hessen, Germany 64289

STEVEN WEISS
US Army Research Lab
2800 Powder Mill Road
Adelphi, MD 20783

YOSHIHIDE YAMADA
NATIONAL DEFENSE ACADEMY
1-10-20 Hashirimizu
Yokosuka, Kanagawa,
Japan 239-8686

APPLIED COMPUTATIONAL ELECTROMAGNETICS SOCIETY JOURNAL
http://aces.ee.olemiss.edu

INFORMATION FOR AUTHORS

PUBLICATION CRITERIA

Each paper is required to manifest some relation to applied computational electromagnetics. **Papers may address general issues in applied computational electromagnetics, or they may focus on specific applications, techniques, codes, or computational issues.** While the following list is not exhaustive, each paper will generally relate to at least one of these areas:

1. **Code validation.** This is done using internal checks or experimental, analytical or other computational data. Measured data of potential utility to code validation efforts will also be considered for publication.

2. **Code performance analysis.** This usually involves identification of numerical accuracy or other limitations, solution convergence, numerical and physical modeling error, and parameter tradeoffs. However, it is also permissible to address issues such as ease-of-use, set-up time, run time, special outputs, or other special features.

3. **Computational studies of basic physics.** This involves using a code, algorithm, or computational technique to simulate reality in such a way that better, or new physical insight or understanding, is achieved.

4. **New computational techniques** or new applications for existing computational techniques or codes.

5. **"Tricks of the trade"** in selecting and applying codes and techniques.

6. **New codes, algorithms, code enhancement, and code fixes.** This category is self-explanatory, but includes significant changes to existing codes, such as applicability extensions, algorithm optimization, problem correction, limitation removal, or other performance improvement. **Note: Code (or algorithm) capability descriptions are not acceptable, unless they contain sufficient technical material to justify consideration.**

7. **Code input/output issues.** This normally involves innovations in input (such as input geometry standardization, automatic mesh generation, or computer-aided design) or in output (whether it be tabular, graphical, statistical, Fourier-transformed, or otherwise signal-processed). Material dealing with input/output database management, output interpretation, or other input/output issues will also be considered for publication.

8. **Computer hardware issues.** This is the category for analysis of hardware capabilities and limitations of various types of electromagnetics computational requirements. Vector and parallel computational techniques and implementation are of particular interest.

Applications of interest include, but are not limited to, antennas (and their electromagnetic environments), networks, static fields, radar cross section, inverse scattering, shielding, radiation hazards, biological effects, biomedical applications, electromagnetic pulse (EMP), electromagnetic interference (EMI), electromagnetic compatibility (EMC), power transmission, charge transport, dielectric, magnetic and nonlinear materials, microwave components, MEMS, RFID, and MMIC technologies, remote sensing and geometrical and physical optics, radar and communications systems, sensors, fiber optics, plasmas, particle accelerators, generators and motors, electromagnetic wave propagation, non-destructive evaluation, eddy currents, and inverse scattering.

Techniques of interest include but not limited to frequency-domain and time-domain techniques, integral equation and differential equation techniques, diffraction theories, physical and geometrical optics, method of moments, finite differences and finite element techniques, transmission line method, modal expansions, perturbation methods, and hybrid methods.

Where possible and appropriate, authors are required to provide statements of quantitative accuracy for measured and/or computed data. This issue is discussed in "Accuracy & Publication: Requiring, quantitative accuracy statements to accompany data," by E. K. Miller, *ACES Newsletter*, Vol. 9, No. 3, pp. 23-29, 1994, ISBN 1056-9170.

SUBMITTAL PROCEDURE

All submissions should be uploaded to ACES server through ACES web site (http://aces.ee.olemiss.edu) by using the upload button, journal section. Only pdf files are accepted for submission. The file size should not be larger than 5MB, otherwise permission from the Editor-in-Chief should be obtained first. Automated acknowledgment of the electronic submission, after the upload process is successfully completed, will be sent to the corresponding author only. It is the responsibility of the corresponding author to keep the remaining authors, if applicable, informed. Email submission is not accepted and will not be processed.

EDITORIAL REVIEW

In order to ensure an appropriate level of quality control, papers are peer reviewed. They are reviewed both for technical correctness and for adherence to the listed guidelines regarding information content and format.

PAPER FORMAT

Only camera-ready electronic files are accepted for publication. The term **"camera-ready" means that the material is neat, legible, reproducible, and in accordance with the final version format listed below.**

The following requirements are in effect for the final version of an ACES Journal paper:

1. The paper title should not be placed on a separate page.

The title, author(s), abstract, and (space permitting) beginning of the paper itself should all be on the first page. The title, author(s), and author affiliations should be centered (center-justified) on the first page. The title should be of font size 16 and bolded, the author names should be of font size 12 and bolded, and the author affiliation should be of font size 12 (regular font, neither italic nor bolded).

2. An abstract is required. The abstract should be a brief summary of the work described in the paper. It should state the computer codes, computational techniques, and applications discussed in the paper (as applicable) and should otherwise be usable by technical abstracting and indexing services. The word "Abstract" has to be placed at the left margin of the paper, and should be bolded and italic. It also should be followed by a hyphen (—) with the main text of the abstract starting on the same line.

3. All section titles have to be centered and all the title letters should be written in caps. The section titles need to be numbered using roman numbering (I. II. ….)

4. Either British English or American English spellings may be used, provided that each word is spelled consistently throughout the paper.

5. Internal consistency of references format should be maintained. As a guideline for authors, we recommend that references be given using numerical numbering in the body of the paper (with numerical listing of all references at the end of the paper). The first letter of the authors' first name should be listed followed by a period, which in turn, followed by the authors' complete last name. Use a coma (,) to separate between the authors' names. Titles of papers or articles should be in quotation marks (" "), followed by the title of journal, which should be in italic font. The journal volume (vol.), issue number (no.), page numbering (pp.), month and year of publication should come after the journal title in the sequence listed here.

6. Internal consistency shall also be maintained for other elements of style, such as equation numbering. Equation numbers should be placed in parentheses at the right column margin. All symbols in any equation have to be defined before the equation appears or right immediately following the equation.

7. The use of SI units is strongly encouraged. English units may be used as secondary units (in parentheses).

8. Figures and tables should be formatted appropriately (centered within the column, side-by-side, etc.) on the page such that the presented data appears close to and after it is being referenced in the text. When including figures and tables, all care should be taken so that they will appear appropriately when printed in black and white. For better visibility of paper on computer screen, it is good to make color figures with different line styles for figures with multiple curves. Colors should also be tested to insure their ability to be distinguished after black and white printing. Avoid the use of large symbols with curves in a figure. It is always better to use different line styles such as solid, dotted, dashed, etc.

9. A figure caption should be located directly beneath the corresponding figure, and should be fully justified.

10. The intent and meaning of all text must be clear. For authors who are not masters of the English language, the ACES Editorial Staff will provide assistance with grammar (subject to clarity of intent and meaning). However, this may delay the scheduled publication date.

11. Unused space should be minimized. Sections and subsections should not normally begin on a new page.

ACES reserves the right to edit any uploaded material, however, this is not generally done. It is the author(s) responsibility to provide acceptable camera-ready files in pdf and MSWord formats. Incompatible or incomplete files will not be processed for publication, and authors will be requested to re-upload a revised acceptable version.

COPYRIGHTS AND RELEASES

Each primary author must execute the online copyright form and obtain a release from his/her organization vesting the copyright with ACES. Both the author(s) and affiliated organization(s) are allowed to use the copyrighted material freely for their own private purposes.

Permission is granted to quote short passages and reproduce figures and tables from and ACES Journal issue provided the source is cited. Copies of ACES Journal articles may be made in accordance with usage permitted by Sections 107 or 108 of the U.S. Copyright Law. This consent does not extend to other kinds of copying, such as for general distribution, for advertising or promotional purposes, for creating new collective works, or for resale. The reproduction of multiple copies and the use of articles or extracts for commercial purposes require the consent of the author and specific permission from ACES. Institutional members are allowed to copy any ACES Journal issue for their internal distribution only.

PUBLICATION CHARGES

All authors are allowed for 8 printed pages per paper without charge. Mandatory page charges of $75 a page apply to all pages in excess of 8 printed pages. Authors are entitled to one, free of charge, copy of the printed journal issue in which their paper was published. Additional reprints are available for $ 50. Requests for additional re-prints should be submitted to the managing editor or ACES Secretary.

Corresponding author is required to complete the online form for the over page charge payment right after the initial acceptance of the paper is conveyed to the corresponding author by email.

ACES Journal is abstracted in INSPEC, in Engineering Index, DTIC, Science Citation Index Expanded, the Research Alert, and to Current Contents/Engineering, Computing & Technology.